WYLE LABORATORIES
SCIENTIFIC SERVICES AND SYSTEMS GROUP
EASTERN OPERATIONS
FACILITIES LOCATED IN
HUNTSVILLE, ALA. AND HAMPTON, VA.

(NASA-CR-144092)   STUDY TO DEFINE UNSTEADY   N76-13021
FLOW FIELDS AND THEIR STATISTICAL
CHARACTERISTICS (Wyle Labs., Inc.)   145 p HC
$6.00   CSCI 01A   Unclas
                                             G3/02   06016

research REPORT

WYLE LABORATORIES — RESEARCH STAFF
REPORT WR 75-1

STUDY TO DEFINE UNSTEADY FLOW FIELDS
AND THEIR STATISTICAL CHARACTERISTICS

by

J. E. Robertson
R. M. Slone, Jr.
M. E. Wang

May 1975

Draft Report

of

Work Performed Under Contract NAS8-30535

ABSTRACT

Preliminary estimates of Space Shuttle fluctuating pressure
environments have been made based on analyses of wind
tunnel data and empirical prediction techniques developed
by Wyle Laboratories. Particular emphasis has been given
to the External Tank and Solid Rocket Boosters for the tran-
sonic speed regime during launch of a parallel-burn Space
Shuttle configuration. Predicted environments are presented
as space-averaged zonal profiles with progressive shading
from zone to zone to illustrate spatial variations in the mag-
nitude of the fluctuating pressure coefficient over the surfaces
of the External Tank and Solid Rocket Boosters. Predictions
are provided for the transonic Mach number range from
$0.8 \leq M_\infty \leq 1.5$ and for supersonic Mach numbers of 2.0
and 3.0.

TABLE OF CONTENTS

LIST OF FIGURES

LIST OF FIGURES (CONCLUDED)

1.0 INTRODUCTION

During launch and flight through the atmosphere, the external surfaces of the Space Shuttle vehicles will be exposed to high intensity acoustic fluctuating pressure environments. These environments will be critical to the design and success of the complete Space Shuttle system. In order to ensure structural integrity, reliability, and the economic operational requirements of the Space Shuttle, accurate definition of the critical aerodynamic flow fields and the attendant acoustic environments which will be encountered during Space Shuttle flight is required at the earliest possible time during the development stage. Wyle Laboratories has engaged in a research program under NASA-MSFC Contract NAS8-30535 to define the fluctuating pressure environments on the Space Shuttle during ascent flight.

During the early phases of this program, oil flow pictures and shadowgraph photographs from Space Shuttle wind tunnel tests were analyzed to define the significant flow regimes over the Space Shuttle. Sketches depicting the location and areal range of these flow regimes were prepared for both the Solid Rocket Booster (SRB) and the External Tank (ET). Analytical predictions of normalized fluctuating pressure coefficient $\sqrt{\overline{p^2}}/q_\infty$ were then made for the areas of interest on the ET and SRB. These predicted $\sqrt{\overline{p^2}}/q_\infty$ values were refined by comparison with Space Shuttle wind tunnel data. This information was then compiled to indicate zones of equivalent fluctuating pressure on the ET and SRB surfaces.

The predicted fluctuating pressure environments resulting under this program are as detailed and precise as the presently available wind tunnel flow visualization and fluctuating pressure data will allow.

Section 2.0 contains a brief description of various types of fluctuating pressure environments experienced by the Space Shuttle vehicle. Presented in section 3.0 are the general prediction formulae used to estimate the fluctuating pressure environments on the Space Shuttle. Section 4.0 discusses the aerodynamic flow regimes of interest on the External Tank and Solid Rocket Boosters and presents the flow visualization data used to define these flow environments.

Presented in section 5.0 are fluctuating pressure estimates for the Space Shuttle External Tank and Solid Rocket Boosters, and section 6.0 contains concluding remarks.

2.0 FLUCTUATING PRESSURE ENVIRONMENTS

When a vehicle moves through air there are two basic means by which it can produce noise: (1) by its propulsion mechanisms (motor-jet, rocket, etc.), and (2) by its interaction with its surroundings. At low speeds, for example, during and immediately after lift-off, the first of these is by far the dominant one, while near or above the speed of sound the second becomes important.

During any flight cycle for an aerospace vehicle, there are four important phases of the flight which should be investigated in order to assess the environmental trends due to acoustic and fluctuating pressures. These are listed in the chronological order in which they occur.

- Lift-off phase during which acoustic excitations result from the exhaust noise.

- Launch flight to orbit phase, during which rocket exhaust noise diminishes and aerodynamic fluctuating pressures (pseudo-sound) start to dominate. From an aerodynamic noise viewpoint, this phase becomes most critical at transonic Mach numbers ($0.8 \leq M \leq 1.5$).

- Reentry phase during which only aerodynamic fluctuating pressures are present.

- Flyback phase during which the noise from flyback engines dominates.

This report is devoted to the specification of surface fluctuating pressures resulting from unsteady aerodynamic flows which occur during the launch phase of flight since this is considered to be the primary area of study for this contractual effort. Inflight surface fluctuating pressures are distinctly different from acoustic disturbances originating from rocket exhaust flows and engine noise. Inflight disturbances, as considered herein, arise from several modes or disturbances—the principal source being the passage of a turbulence environment over the external surface. One other important source to be discussed is shock-wave oscillation which is characterized by both turbulence (in close proximity to the foot of the shock wave) and pseudo-static disturbances resulting from the modulation of the pressure gradient through the shock wave. Thus, inflight fluctuating pressure phenomena are near-field mechanisms acting on the surface of a vehicle with the distinction that the disturbances are generally convected at some fraction of the local mean flow velocity. On the other hand, rocket noise and engine noise are acoustic mode disturbances which generally originate away from the surface. Furthermore, acoustic mode disturbances consist of sound waves which propagate at the local speed of sound with a direction independent of the local velocity.

Two specific areas are considered in the present study: (1) "basic" fluctuating pressure environments which will occur on virtually all aerospace vehicles during some phase of flight, and (2) "special" fluctuating pressure environments which are unique to the Space Shuttle configuration and mission parameters. Under the first category fall such environments

2

as attached turbulent boundary layers, separated flows and certain shock-oscillation environments. Other environments which are more dependent on configuration and mission parameters are certain types of shock-wave impingement, protuberance flows, wake and base flows, rocket plume interference, and rocket exhaust impingement. Distinction is made between the two areas since the "basic" fluctuating pressure environments are dictated by the aerodynamic flow field of the overall vehicle; whereas, the "special" fluctuating pressure environments accompany relatively localized flow fields which are essentially superimposed upon the basic flow field.

There are an infinite number of possible aerodynamic flow fields, each affected by vehicle trajectory, Mach number, and vehicle configurations; any discussion of their fluctuating pressure environments must therefore be general. Unsteady flow phenomena are of particular importance at transonic speeds, since in this range, fluctuating pressures reach maximum levels due to their proportionality to dynamic pressure (q). However, peak fluctuating pressures do not necessarily occur at maximum dynamic pressure for certain regions of a vehicle due to the nonhomogeneous nature of the flow field. For example, regions of the vehicle exposed to separated flow and the impingement of oscillating-shock waves will experience fluctuating pressures at least an order of magnitude greater than regions exposed to attached flow. Thus, if separated flow and oscillating-shock waves are present, say at Mach numbers other than the range of maximum dynamic pressure, then peak fluctuating pressures will also be encountered at conditions other than at maximum q. Thus, it is easily seen that the parameters mentioned above are very important in the specification of fluctuating pressure levels.

In order to assess the fluctuating pressure environments for a vehicle of unique geometry, such as the Space Shuttle vehicle, it is convenient to develop prediction formulae for the statistical properties of the fluctuating pressures for each basic type of unsteady flow field. From previous wind tunnel tests and flight data, the following unsteady flow fields have been identified as sources of fluctuating pressures:

a) Attached turbulent boundary layers

b) Separated flows:
    1) Expansion Corners
    2) Compression Corners

c) Oscillating shock waves:
    1) Transonic terminal shock
    2) Supersonic compression shock
    3) Supersonic impinging shock

d) Wake and base flows

e) Jet/rocket exhaust flow interaction with the vehicle aerodynamic flow field

f) Protuberance flows

g) Rocket exhaust impingement.

3

During past research programs, not all of these phenomena have been studied in sufficient detail to enable prediction methods to be developed (for example, items d and g). However, the other flow fields have been examined sufficiently to provide at least a first-order analysis of the attendant fluctuating pressure environments.

The surface fluctuating pressures for each of the above flow conditions may be expected to exhibit different statistical characteristics due to dissimilarities in the mechanisms at work. For example, attached flow pressure fluctuations results from the disturbances within turbulent boundary layers. Separated flow pressure fluctuations result from disturbances within the separated shear layer and instabilities associated with the separation and reattachment points. Pressure fluctuations for shock-wave oscillation result from the movement of the shock wave and the static pressure discontinuity associated with the shock wave. Generally, shock-wave impingement occurs in the presence of either attached or separated flow and added disturbances result due to the combined environments. Thus, in order to develop prediction techniques for the many unsteady flow fields which a vehicle may encounter, it is necessary to examine each flow field independently, and to define, at least empirically, the statistical properties of the attendant fluctuating pressure environment.

The statistical characteristics of each fluctuating pressure environment necessary for the complete specification of aeroacoustic loading may be classified under four parameters:

- The fluctuating pressure coefficient, $\sqrt{\overline{p^2}}/q_\infty$.

- The nondimensional power spectra.

- The cross-power spectra (or narrow band cross-correlation).

- Trajectory dependent flight parameters, such as Mach number and angle of attack, and dynamic pressure.

In the following section, a summary of the prediction formula is presented together with typical comparisons of the predictions with existing experimental data.

3.0 GENERAL PREDICTION FORMULAE

Analyses of various unsteady flow regimes have been performed under this contract for the purpose of estimating the attendant fluctuating pressures. This work is based on the results contained in references 1 through 29 and 35. A detailed summary of the basic findings and prediction formulae is presented in Appendix A. The surface fluctuating pressures for both "basic" unsteady flows and certain "special" unsteady flows unique to the Space Shuttle vehicles have been reviewed. The resulting empirical formulae have been generalized for the various environments in order to achieve: (1) simplicity in their mathematical formulation, (2) a relationship to the physical parameters of the flow, and (3) good agreement with the available experimental data. As noted in the previous section, complete definition of a fluctuating pressure environment requires that the fluctuating pressure coefficient, power spectra, and cross-power spectra be defined. A brief summary of prediction methods for each of these statistical parameters is given in the following subsections for attached flow, separated flow, and shock-wave oscillation.

3.1 Fluctuating Pressure Coefficient

The correct method for computing overall fluctuating pressure levels for surfaces beneath the convected turbulence in boundary layers is in terms of the fluctuating pressure coefficient, $\sqrt{\overline{p^2}}/q_\infty$. Here the root-mean square pressure, $\sqrt{\overline{p^2}}$, is normalized by some characteristic dynamic pressure. Free-stream dynamic pressure, q_∞, local dynamic pressure, q_ℓ, and wall shear stress, τ_ω, have been used to normalize $\sqrt{\overline{p^2}}$ so that meaningful data collapse can be realized through the Mach number range. The most generally accepted normalizing parameter is q_∞ and, thus, it is used in the current expressions.

The effect of Mach number on the normalized rms intensities of the fluctuating pressures in attached flows are shown in Figure 1. There is significant scatter in the data which may be attributed to several factors: (1) background noise and free-stream turbulence in the testing medium, (2) instrumentation quality and the precision of the experimental technique, and (3) data acquisition and reduction techniques, etc. For the range of Mach numbers covered in the data of Figure 1, the normalized rms value of the fluctuating pressure varies from $\sqrt{\overline{p^2}}/q_\infty \approx 0.006$ at subsonic Mach numbers to 0.002 at supersonic Mach numbers. Lowson, reference 1, proposed the following semiempirical prediction formula which appears to agree with the general trend in the data:

$$\sqrt{\overline{p^2}}/q_\infty = 0.006 / (1 + 0.14 \, M_\infty^2) \tag{1}$$

It is important to note that this formula has some theoretical basis and is not strictly an empirical approximation of measured results (see reference 1). The use of this formula at high supersonic and hypersonic Mach numbers should be done with the understanding that it has not been verified in this Mach number range and may lead to significant error. Predictions for high supersonic and hypersonic Mach numbers have been developed under a previous program and are presented in Reference 27. However, in the Mach number range up to, say $M_\infty = 3.0$, the above equation is in good agreement with experimental results.

The variation of fluctuating pressure level, normalized by free-stream dynamic pressure, with local Mach number for various separated flow environments is presented in Figure 2. These data represent both expansion and compression corners. For expansion corners, the largest levels occurred at low Mach numbers and decreased as local Mach number increased. These data represent the region of plateau-static pressure and the tolerance brackets on the data represent the variations in fluctuating pressure level within the region of constant static pressure rather than scatter in the measurements. A good empirical approximation to the expansion-induced separated flow disturbances is:

$$\sqrt{\overline{p^2}} / q_\infty = \frac{0.045}{1 + M^2} \tag{2}$$

This equation is similar in form to that previously proposed for attached turbulent boundary layers.

Fluctuating pressure measurements for the region of plateau-static pressure upstream of compression corners exhibit a somewhat different trend with Mach number. In general, the compression corner data showed an increase in fluctuating pressure level with increasing free-stream Mach number in the range, $1.0 \leq M_\infty \leq 2.0$ — reaching a constant level at Mach numbers above 2.0. Free-stream Mach number is used here because adequate data is not available for determining the local Mach number in the vicinity of the compression-induced separated flow region. Derivation of an empirical prediction formula for the fluctuating pressure level within compression-induced separated flows will require further study.

Generally, shock-wave oscillation produces the most intense fluctuating pressure levels that are usually encountered by a vehicle. Typical shock waves encountered by vehicles are:

- Terminal shock waves for regions of transonic flow.

- Displaced oblique shock waves as induced by the separated flow in compression corners at local supersonic speeds.

- Reattachment shock waves in the vicinity of the reattachment point for separated flows generated by both compression and expansion corners.

6

- Impingement shock waves as caused by local bodies such as strap-on rockets.

- Oblique shock waves associated with separated flow induced by highly expanded rocket plume at high altitudes.

All shock waves may be expected to produce generally similar fluctuating pressure environments since the pressure fluctuations arise from motion of the shock wave. It has been found that the oscillations are driven primarily by velocity fluctuations in the incoming turbulent boundary layer. The maximum displacement is governed by mean flow conditions. Except for alternating flow conditions, where oscillation distance is much larger than shock thickness and the power spectrum is therefore a Poisson distribution, spectra and overall levels for various shock environments are quite similar. A discussion of shock oscillation and results of analytical investigation are presented in reference 28, and are summarized in Appendix B. The overall level is a strong function of Mach number in the transonic regime; typical overall levels for terminal shock wave oscillation are presented in Figure 3.

3.2 Power Spectra

Power spectra represent the distributions of the mean-square fluctuating pressure with frequency. Power spectra for the various fluctuating pressure environments are found to scale on a Strouhal number basis; that is, frequency is normalized by multiplying by a typical length and dividing by a typical velocity. Normalized spectra enable similar, stationary flows to be represented by a single spectrum regardless of the scale of the flow field or the free-stream velocity.

Numerous studies have been conducted to determine the proper parameters to be used to nondimensionalize the spectra for various aeroacoustic environments. Unfortunately, the choice of parameters which best collapses the data appear to be dependent on the nature of the fluctuating pressure environment. In general, free-stream velocity is used as the normalizing velocity parameter, although a typical eddy convection velocity (itself a function of frequency) has been used occasionally. The local convection velocity appears to correspond more closely with the physical situation for fluctuating pressures due to the turbulent eddies. Selection of a typical length is more difficult. Boundary layer thickness, δ, displacement thickness, δ^*, wall shear stress, τ_w, and momentum thickness, θ, have all been used by various investigators for attached flow. For separated flow and shock-wave oscillation, local boundary layer thickness and separation length have also been used.

Generally, prior knowledge of the fluctuating pressure is required to predict the power spectra; however, prediction formulae for the overall levels have been developed to a limited degree, as discussed in section 3.1.

Prediction formulae for the power spectra for the various unsteady flows, with the exception of shock-wave oscillation, have the following form:

$$\frac{\phi(f) \, U}{q_\infty^2 \, L} = \frac{\overline{p^2} / q_\infty^2}{\frac{f_0 \, L}{U} \left\{ 1 + \left(f/f_0 \right)^n \right\}^k}$$

(3)

where

U = characteristic velocity

L = characteristic length

f_0 = characteristic frequency

n, k = spectrum shape factor

For shock-wave oscillation, the power spectrum is a combination of power spectra for inviscid shock-wave motion as well as contributions from the separated flow near the foot of the shock wave. The prediction formula has the following form:

$$\left(\frac{\phi(f) \, U}{q_\infty^2 \, L} \right)_{sw} = \left(\frac{\phi(f) \, U}{q_\infty^2 \, L} \right)_{sw}^{I} + k_1 \left(\frac{\phi(f) \, U}{q_\infty^2 \, L} \right)_{s}$$

(4)

where $k_1 \approx 0.25$, the subscripts sw and s denote shock wave and separated flow respectively, and the superscript I denotes the absence of viscous effects. A complete discussion of the power spectra predictions for the various fluctuating pressure environments are presented in reference 26. Comparisons of predicted power spectra with experimental data are presented for attached flow, separated flow, and shock-wave oscillation in Figures 4, 5, and 6. Also, power spectra predictions have been developed for nonhomogeneous attached and separated flows (see reference 26). Comparisons of these predictions with experimental data are shown in Figure 7 together with attached flow, separated flow and shock-wave oscillation.

3.3 Cross-power Spectra

The final requirement in determining the characteristics of the fluctuating pressure environment of an unsteady flow field is to define the narrow band, space correlation function or co-power spectral density. This parameter is the key function needed to describe an impinging pressure field on a structure in order to calculate the induced mean-square response of the structure (see, for example, reference 17 for the structural response computational technique). The spatial correlation properties of a fluctuating pressure field can be obtained only from a careful and detailed examination of the flow field at a large number of points.

Measurements by several investigators have shown that the co-power spectral density of the turbulent boundary layer pressure fluctuations in the direction of the flow can be approximated by an exponentially damped cosine function, and the lateral co-spectral density can be approximated by an exponential function.

The spatial coherence of the fluctuating pressure environments as defined by the co-power spectra have been evaluated for the various unsteady flows. The cross-power spectra for attached turbulent boundary layers, two- and three-dimensional separated flows and protuberance-induced wake flows appear to be fairly well defined, at least in the longitudinal direction. Much uncertainty remains for transverse cross-power spectra in upstream separated flows and protuberance wake flows. Both longitudinal and transverse cross-power spectra for the regions beneath oscillating shock waves require additional study.

In general, the normalized co-power spectra for the various fluctuating pressure environments can be defined as exponentially damped sinusoids for the longitudinal axis as follows:

$$C(\xi, f) = e^{-a\omega\xi/U_c} \cos \frac{\omega\xi}{U_c} \tag{5}$$

Along the transverse axis, the normalized co-spectra may be defined by an exponential decay as follows:

$$C(\eta, f) = e^{-b\omega\eta/U_c} \tag{6}$$

where ω is the circular frequency, U_c is the convection velocity, and ξ and η are the longitudinal and transverse separation distances, respectively, and a and b are the coefficients of exponential decay.

The coefficient of exponential decay is a function of the particular environment under study and may also depend on free-stream Mach number as well as local flow conditions. Derivations of the coefficient of exponential decay are presented in reference 26 for each unsteady flow condition where the data was sufficiently well defined to merit an analysis. For attached boundary layer flow, the coefficient of exponential decay in the longitudinal direction was found to be a = 0.10. For two-dimensional and axisymmetric separated flows, the values ranged from 0.13 at M_∞ = 2.5 to 0.33 at M_∞ = 1.60. The coefficient of exponential decay in the inner and outer regions of three-dimensional separated flows upstream of cylindrical protuberances were approximately the same in the longitudinal direction with a value of a ≈ 0.7. In the protuberance wake, the spatial decays were clearly defined only in the neck and far-wake regions with a value of a ≈ 0.19. Typical co- and quad-spectra are presented in Figures 8 and 9 for attached flow and separated flow, respectively.

4.0 AERODYNAMIC FLOW FIELDS

The Space Shuttle launch configuration is a complex combination of several bodies—with each major body having a different geometry. The flow field for the mated launch vehicle will consist of the individual flow fields of each major body of the vehicle with modified regions as generated by the interference and interactions among the flow fields of the various bodies. An extensive experimental/theoretical study has been performed to accurately define the resulting flow over the mated configuration. The aerodynamic flow field was defined so that estimates of surface fluctuating pressure environments on the External Tank and the Solid Rocket Boosters could be made. The approach taken was to first analyze the interference-free flow field for each major body of the mated Space Shuttle vehicle, and to consider the effects on the individual flow fields of predicted flow interference. This information was then used to help interpret oil flow diagrams and other wind tunnel data.

Regions of significant unsteady aerodynamic flow have been identified and located through close examination of wind tunnel flow visualization data. These oil flow diagrams and shadowgraph photographs indicate the type and location of the various flow regimes over the surface of the ET and SRB for a wide range of Mach numbers. These flow regimes are described herein as interference-free flow and interference flow environments.

4.1 Interference-free Flow Environments

4.1.1 Solid Rocket Boosters — The solid rocket motors are basically cone-cylinder missile configurations with a 17.5 degree cone half angle. Cone-cylinder geometries have been studied extensively in past years and their unsteady flow fields are fairly well defined. For these bodies, the following environments are anticipated:

- Attached turbulent boundary layer flow

- Shoulder-induced separated flow (subsonic Mach numbers)

- Terminal shock-wave oscillation (transonic Mach numbers below 1.0).

For a cone-cylinder body, the types of unsteady flow conditions which will occur at a given Mach number depend on cone-angle, angle of attack, and Reynolds number. Typical flow fields for cone-cylinders are shown for the zero angle of attack, interference-free case in Figure 10.

For all Mach numbers, the flow over the nose cones will be attached with the location of boundary layer transition occurring as a function of Reynolds number. Flow characteristics in the vicinity of the cone-cylinder juncture will vary depending on free-stream Mach number, angle of attack, and shoulder angle. For cones having half angles (shoulder angles) greater than approximately 10 degrees, the flow will not fully expand over the shoulder at subsonic speeds but will separate at the shoulder. A separation bubble is thus formed, with reattachment occurring a short distance aft of the shoulder with the axial extent of the bubble

depending primarily on cone-angle. At high subsonic Mach numbers, the flow negotiates the shoulder without separating, reaches supersonic speed immediately aft of the shoulder, and produces a near-normal, terminal-shock wave at some point along the cylinder. The boundary layer becomes extremely thin at the shoulder due to the strong expansion fan and a new boundary layer is essentially formed at the shoulder. The boundary layer remains attached between the shoulder and the shock wave. At the shock location, the boundary layer may undergo separation depending on the strength of the shock wave. The shock strength is at a maximum corresponding to the initial attachment of the flow at the shoulder and decreases in strength as it moves aft with increasing Mach number. At sonic speed, the terminal-shock wave will move aft of the body and will be reduced to zero strength.

For Mach numbers above 1.0, the interference-free flow fields for the SRB will consist of attached boundary layer flow and possible shock-oscillation environments corresponding to surface protuberances and other geometric irregularities.

     4.1.2 External Tank — The ET is basically an ogive-cylinder configuration. Ogive-cylinders have been studies in the past, although not as extensively as the more basic cone-cylinder configuration. A key factor in this type of body is the configuration of the shoulder.

Robertson (reference 30) investigated the effect of introducing a radius at the shoulder of a cone-cylinder, with geometry ranging from a sharp corner to an ogive-cylinder. It was found that flow separation decreases as shoulder radius increases, with no separation observed for ogive-cylinders. Static pressure measurements indicate that the terminal-shock wave on an ogive-cylinder is generally weaker and occurs at a higher Mach number than on an equivalent cone-cylinder. Interference-free flow environments for the External Tank will therefore consist of attached boundary layer flow and terminal shock wave oscillation (though not as severe as for a cone-cylinder) at subsonic speeds, and attached boundary layer flow for Mach numbers above 1.0. As with the SRB, there may also be separated flow and shock oscillation environments corresponding to surface protuberances and other irregularities.

4.2 Mated Vehicle Interference Flow Environments

The launch configuration of Space Shuttle vehicles will be comprised of four approximately parallel bodies, as pictured in Figure 11. Such vehicles have regions of flow interference between the various bodies which will result in relatively severe fluctuating pressure environments. For other similar configurations, such as Titan III, shock-induced pressure fluctuations have been observed at the location of shock impingement from one body onto the surface of the other bodies. This phenomenon may be anticipated for Mach numbers starting at approximately 1.2 when the bow shock for the mated vehicle divides into separate bow shocks for each major body of the vehicle. Shock impingement will continue to produce severe fluctuating pressure levels until Booster separation, ET separation, or until the q_∞ decreases to a level sufficiently low that the disturbances are no longer of concern. The following shock interference regions will occur:

1)   Bow-shock impingement and shock-boundary layer interaction between the SRB and ET due to SRB bow shock.

2)   Bow-shock impingement and shock-boundary layer interaction between the ET and Orbiter fuselage due to Orbiter bow shock.

3)   Shock-boundary layer interaction between the Orbiter lower wing surfaces and SRB due to wing leading edge shocks.

4)   Possible transonic shock-boundary layer interaction between SRB and ET or ET and Orbiter due to transonic terminal shock waves.

The most severe interference flow regions are anticipated to be in the vicinity of the cone-cylinder juncture of the SRB, in the region between the SRB and ET, and in the region of the ET beneath the Orbiter nose. The most critical Mach number range is anticipated to be in the transonic region ($0.80 \leq M_{\infty} \leq 1.6$) corresponding to maximum dynamic pressure, transonic buffet phenomena and near-normal shock wave impingement. Downstream of the shock-interaction regions, the flow may become choked and a shock-free interference flow and fluctuating-pressure levels on the order of those experienced in homogeneous separated flow may be expected.

4.3 ET and SRB Interference and Interference-free Flow Diagrams

Shadowgraph and oil flow photographs of the flow fields for the mated ascent Shuttle configuration are shown in Figures 12 and 13 respectively. These data clearly show the complex flows resulting from the aerodynamic interference between the various bodies comprising the mated configuration. To access the detailed characteristics of the ET and SRB, the perturbed flows as defined in Figures 12 and 13 were mapped using a transparent overlay with grid and transferred to an unfolded surface grid. For the ET, the surface was unfolded using a separation seam along the bottom ($\theta = 180^{\circ}$) surface centerline which, for $\beta = 0^{\circ}$, results in flow symmetry on either side of the top (0°) surface centerline. For the SRB, the surface was unfolded along the outside surface centerline ($\theta = 90^{\circ}$). Distortion in the flow pattern resulting in a lack of symmetry on either side of the inside ($\theta = 270^{\circ}$) surface centerline is caused by flow interference from the Orbiter.

The resulting ET and SRB flow environments anticipated for SSV ascent are presented in Figures 14 and 15, respectively. These diagrams depict the relative intensity and direction aerodynamic flow over the ET and SRB surfaces for the range of Mach numbers $0.8 \leq M_{\infty} \leq 3.0$ and for angles of attack and sideslip angles $0^{\circ} \leq \alpha \leq 2.0^{\circ}$ and $0^{\circ} \leq \beta \leq 2.0^{\circ}$. It should be noted that no consideration has been made in this analysis for protuberances on the surface of the ET and SRB. The local flow effects resulting from surface protuberances must be derived separately, and may then be superimposed upon these basic flow patterns.

The flow patterns presented in Figures 14 and 15 are largely self-explanatory. Key features of ET flow patterns are:

1)   Shock wave patterns resulting from:

a)   Terminal shock wave upstream of SRB attachment locations associated with transonic flow in the vicinity of the ogive-cylinder juncture of the ET.

12

b) SRB bow shock impingement on the surface of the ET.

c) Orbiter bow shock impingement on the surface of the ET.

d) Normal shock wave resulting from choking of the flow between the ET and the Orbiter in the aft region between these two bodies.

2) Flow separation upstream of the SRB attachment point due to the flow blockage caused by the SRB in close proximity to the ET surface.

3) Wake flow downstream of the SRB attachment point due to the flow blockage caused by the SRB in close proximity to the ET surface.

4) Perturbed flow caused by the support structure for the various bodies comprising the mated Shuttle configuration.

Key features of the SRB flow pattern are:

1) Shock wave patterns resulting from:

a) Terminal shock wave associated with transonic flow in the vicinity of the cone-cylinder juncture of the SRB.

b) SRB bow shock reflection from the surface of the ET and impingement on the SRB nose cone.

c) Impingement of the shock wave from the leading and trailing edges of the Orbiter wings.

d) Flow separation and reattachment shock waves in the vicinity of the SRB attachment ring and the SRB aft skirt.

2) Flow separation upstream of the SRB attachment point due to the flow blockage between the ET and SRB.

3) Wake flow downstream of the SRB attachment point due to the flow blockage between the ET and SRB.

4) General perturbed flow caused by the support structure between the ET and SRB.

Predicted fluctuating pressure environments associated with the flow fields defined in Figures 14 and 15 are discussed in the following section.

5.0 PREDICTED FLUCTUATING PRESSURE ENVIRONMENTS

The flow diagrams presented in section 4.3 represent both interference and noninterference flow fields, and were the first step in the estimation of fluctuating pressure environments for the SSV ascent. Complete definition of these flow fields permitted the following numerical fluctuating pressure predictions.

5.1 Preliminary $\sqrt{\overline{p^2}}/q_\infty$ Predictions

5.1.1 Attached Turbulent Boundary Layer Flow —

$$\frac{\sqrt{\overline{p^2}}}{q_\infty} = \frac{0.006}{1 + 0.14 \, M_\infty^2}$$

<u>ET</u>

- Ogive Nose — All Mach numbers and surface area

- Cylinder — $X_s/D \gtrsim 0$, $M_\infty \lesssim 0.9$

    — $0 \leq X_s/D \leq X_{sw}/D$, $0.9 \lesssim M_\infty < 1.0$

    — $X_s/D > 0$, $M_\infty \geq 1.0$

<u>SRB</u>

- Nose Cone — All Mach numbers and surface area except separation bubble forward of ET forward attach point

- Cylinder — $X_s/D \gtrsim 0.2$, $M_\infty \lesssim 0.78$

    — $0 \leq X_s/D \leq X_{sw}/D$, $0.78 \lesssim M_\infty < 1.0$

    — $X_s D > 0$, $M_\infty \geq 1.0$

<u>5.1.2 Shoulder-Induced Separated Flow</u> — For the shoulder-induced separated flow environment, there are two sources of fluctuating pressures which should be noted. First, immediately aft of the shoulder and within the separation bubble, the pressure fluctuations appear to be fairly homogeneous with levels similar to those observed immediately downsteam of a rearward facing step or in the wake of bulbous payload configurations. However, further aft, the flow reattaches and higher level fluctuating pressures have been observed in the

vicinity of the reattachment point. Also, even though the flow separates at the shoulder, the flow may reach local supersonic conditions as it expands over the separation bubble; in which case, reattachment aft of the shoulder will produce a recompression shock wave and relatively severe fluctuating pressure levels. Measurements presented in References 18 and 31 indicate fluctuating pressure levels ranging up to $\sqrt{\overline{P^2}}/q_\infty = 0.16$ for reattachment aft of cone-cylinder junctures with shoulder angles ranging up to 30 degrees. Most of the results represented in References 18 and 31 show considerable scatter with variations in both cone angle and free-stream Mach number. A prediction curve which appears to be representative of the maximum fluctuating pressure levels for shoulder-induced separated flow on cone-cylinder bodies is given in Figure 16. This curve is attributed to Stevens in Reference 32, and it will be employed in the present predictions for shoulder-induced separated flow. Results from References 18 and 31 are also shown in Figure 16.

For the Mach number range from 0.60 to the attachment Mach number (M_a), the homogeneous region of separated flow will produce fluctuating pressure levels in the range from $\sqrt{\overline{P^2}}/q_\infty = 0.02$ to 0.04 (Figure 2). The fluctuating pressure levels given by Steven's predictions are greater than those for homogeneous separated flow, and the difference can be attributed to the disturbances in the reattachment region (see Figure 10). For cone-cylinders with shoulder angles less than approximately 10 degrees, shoulder separation does not occur and the fluctuating pressure levels will decrease to the levels observed in attached flow as indicated by the dashed portion of the prediction curve.

$$\sqrt{\overline{P^2}}/q_\infty = f(\theta_N), \qquad \text{Figure 16}$$

ET

● None anticipated for the ogive-cylinder configuration.

SRB

● Cylinder — $X_s/D < 0.2$

$\left.\begin{array}{c} \\ \sqrt{\overline{P^2}}/q_\infty = 0.06 \end{array}\right\}$ $M_\infty \leq 0.78$

Expansion-induced separated flow environments occur over a limited transonic Mach number region.

<u>5.1.3 Transonic Shock-Wave Oscillation</u> — Typical cone-cylinder data showing the attachment Mach number and the variation of shock location with free-stream Mach number is presented in Figure 17. Shown in Figure 18 is an interpolation of these data for two additional cone angles. Shock-induced fluctuating pressure levels, normalized by free-stream dynamic pressure, are presented in Figure 19 for a range of cone angles. Curves for $17.5°$ and $22.5°$ are interpolated, $17.5°$ corresponding to the SRB.

Data depicting transonic shock location and oscillation strength for an ogive-cylinder are not presently available. A conservative estimate of shock oscillation strength may be obtained by considering the External Tank to be approximated by a $30°$ cone-cylinder. Fluctuating pressures obtained thereby will likely be several dB higher. Shock location is not predicted for the External Tank, as the interference flow fields resulting from the proximity of the SRB's and Orbiter distort the predicted location. A reasonable picture of the External Tank transonic shock location for the mated launch configuration can be obtained from Figure 14.

The prediction for shock oscillation is:

$$\sqrt{\overline{P^2}}\,/q_\infty = f(M_\infty, \theta_N) \quad , \qquad \text{Figure 18}$$

<u>ET</u>

- Cylinder — Narrow band of approximately $3\delta_\ell$ width corresponding to X_{sw}/D in Figure 17. $\qquad 0.86 < M_\infty \le 1.0$

<u>SRB</u>

- Cylinder — Narrow band of approximately $3\delta_\ell$ width corresponding to X_{sw}/D in Figure 18. $\qquad 0.78 < M_\infty \le 1.0$

Transonic shock oscillation occurs over a limited Mach number range. Fluctuating levels and shock location are easily obtained from Figures 17 through 19; levels and location for the Shuttle are computed and discussed in preceding sections.

<u>5.1.4 Compression-Induced Separated Flow (Two-Dimensional)</u> —

$$\sqrt{\overline{P^2}}\,/q_\infty = 0.015 \text{ to } 0.025 \qquad \text{(Figure 2)}$$

ET

Protuberance Flow Fields
$\left.\vphantom{\begin{array}{c}a\\b\end{array}}\right\}$ All Mach Numbers
Interference Flow Fields

SRB

Protuberance Flow Fields
$\left.\vphantom{\begin{array}{c}a\\b\end{array}}\right\}$ All Mach Numbers
Interference Flow Fields

It should be noted that for compression-induced, two-dimensional, separated flow, $\sqrt{\overline{p^2}}/q_{\infty}$ is a function increasing with Mach number (see Figure 2), and, consequently, maximum fluctuating pressures may occur at a time later than q_{∞} max.

5.1.5 Supersonic Shock-Boundary Layer Interactions —

$$\sqrt{\overline{p^2}} / q_{\infty} = 0.06 \text{ to } 0.08$$

ET

Protuberance Flow Fields
$\left.\vphantom{\begin{array}{c}a\\b\end{array}}\right\}$ Local Mach Number > 1.0
Interference Flow Fields

SRB

Protuberance Flow Fields
$\left.\vphantom{\begin{array}{c}a\\b\end{array}}\right\}$ Local Mach Number < 1.0
Interference Flow Fields

Because the prediction used here is not a function of Mach number (other than applying only for $M > 1$), the critical shock oscillation environment occurs at maximum q_{∞}.

5.2 Mated SSV Launch Configuration Wind Tunnel $\sqrt{\overline{p^2}}/q_\infty$ Data

The formulae used in Section 5.1 to predict fluctuating pressure environments are general in nature and at least semi-empirical in origin. Without detailed definition of local flow parameters, there must always be some question about the applicability of these general equations to specific flow regimes. To improve the confidence in predicted fluctuating pressure environments, additional wind tunnel data more closely related to the SSV launch configuration was examined. Four-percent scale SSV test data (Reference 36) taken on aerodynamic noise model 11-OTS during mid-1973 at the Ames Research Center Unitary Pian Wind Tunnels was used to refine the numerical $\sqrt{\overline{P^2}}/q_\infty$ estimates.

This data was utilized in such a manner as to extract the maximum information possible for definition of the External Tank and Solid Rocket Booster fluctuating pressure environments. Wherever possible, wind tunnel fluctuating pressure data for the bottom centerline of the Orbiter was used to supplement data available for the top centerline of the External Tank. Similarly, External Tank and Solid Rocket Booster fluctuating pressure data were used to augment one another along their adjacent surfaces. This approach, while introducing some measure of uncertainty, can be expected to provide a good indication of anticipated levels in the absence of more directly applicable data.

In all cases where directly applicable SSV wind tunnel data were available for the range of trajectory parameters (Reference 37) anticipated for a launch from the Eastern Test Range, the current predictions reflect that data.

In those cases where data could be extrapolated for application to ET and SRB surfaces, that data was used to temper numerical predictions. For those areas where no specific SSV data were available, appropriate aerodynamic noise theory and general wind tunnel data were applied via the generalized equations presented in Section 3.0.

5.3 Fluctuating Pressure Contours

The External Tank and Solid Rocket Booster fluctuating pressure environments discussed in Sections 5.1 and 5.2 are presented in Figures 20 and 21, respectively. These diagrams depict zones of the ET and SRB surfaces which experience specified fluctuating pressure environments during ascent. In lieu of conventional line contours, progressive shading is utilized here to illustrate the magnitude of the fluctuating pressure coefficient and the transition from low $\sqrt{\overline{P^2}}/q_\infty$ values to relatively higher ones. These space-averaged environmental predictions are provided for the transonic range $(0.8 \leq M_\infty \leq 1.5)$ and for supersonic Mach numbers of 2.0 and 3.0. The local flow parameters are relatively insensitive to small changes in the low α and β values specified for the wind tunnel test data, so the present predictions may be considered valid over the approximate range $0° \leq \alpha \leq 2.0°$ and $0° \leq \beta \leq 2.0°$.

6.0 CONCLUDING REMARKS

Preliminary estimates of Space Shuttle fluctuating pressure environments have been made based on analyses of wind tunnel data and prediction techniques developed by Wyle Laboratories. Particular emphasis has been given to the transonic speed regime during launch of a parallel-burn Space Shuttle configuration. Analyses have consisted of the following:

- Review of shadowgraphs and oil flow photographs of scale-model Space Shuttle flow fields as obtained in the NASA-MSFC 14-inch Trisonic Wind Tunnel. These data were used to develop flow patterns over the surface of the External Tank and SRB for the Mach number range from 0.6 to 3.0.

- Based on identified flow fields, predictions of attendant fluctuating pressure environments were made. These environments were specified in terms of progressively shaded zones to illustrate the magnitude of the fluctuating pressure coefficient $\sqrt{\overline{p^2}}/q_\infty$ over the surface of the External Tank and Solid Rocket Boosters.

- Specification of empirically determined rms fluctuating pressure levels typical of the interference-free and interference-induced flow fields typical of those which occur over the surfaces of the External Tank and Solid Rocket Boosters.

- Equations describing the spectral distribution of the various fluctuating pressure environments are presented in Section 3.2 and the appendix. For further detail, the reader is directed to Figures 4 through 7 and the indicated references.

- Information on the cross-power spectral density of the fluctuating pressure environments is given in Section 3.3, the appendix, Figures 8 and 9, and their related references.

Because of the complex nature of the flow fields and attendant fluctuating pressure levels, the reader is referred to the data presented in Figures 20 and 21 for predicted environments.

REFERENCES

1. Lowson, M. V., "Prediction of Boundary Layer Pressure Fluctuations," Wyle Laboratories Research Staff Report WR 67-15, October 1967.

2. Speaker, W. V., and C. M. Ailman, "Spectra and Space-time Correlations of the Fluctuating Pressures at a Wall Beneath a Supersonic Turbulent Boundary Layer Perturbed by Steps and Shock Waves," NASA CR-486, May 1966.

3. Bull, M. K., "Properties of the Fluctuating Wall Pressure Field of a Turbulent Boundary Layer," AGARD Report 455, April 1963.

4. Bull, M. K., et al, "Wall Pressure Fluctuations in Boundary Layer Flow and Response of Simple Structure to Random Pressure Fields," University of Southampton, AASU Report 243, 1963.

5. Kistler, A. L., and W. S. Chen, "The Fluctuating Pressure Field in a Supersonic Turbulent Boundary Layer," Jet Propulsion Laboratory Technical Report No. 32-277, August 1962.

6. Belcher, P. M., "Prediction of Boundary Layer Turbulence Spectra and Correlations for Supersonic Flight," Presented at the 5th International Acoustic Congress, Liege, Belgium, September 1965.

7. Serafini, J. S., "Wall Pressure Fluctuations and Pressure Velocity Correlations in a Turbulent Boundary Layer," NASA TR R-165, December 1963.

8. Bakewell, H. P., Jr., et al, "Wall Pressure Correlation in Turbulent Pipe Flow," U. S. Navy Sound Laboratory Report No. 559, August 1962.

9. Shattuck, R. D., "Sound Pressures and Correlations of Noise on the Fuselage of a Jet Aircraft in Flight," NASA TN D-1086, August 1961.

10. Willmarth, W. W., and F. W. Roos, "Resolution and Structure of the Wall Pressure Field Beneath a Turbulent Boundary Layer," J. Fluid Mech., Vol. 22, Part 1, pp. 81-94, 1965.

11. Maestrello, L., "Measurement of Noise Radiated by Boundary Layer Excited Panels," J. Sound Vib., 2 (2), 1965.

12. Hilton, D. A., "In-flight Aerodynamic Noise Measurements on a Scout Launch Vehicle," NASA TN D-1818, July 1963.

13. Williams, D. J. M., "Measurements of the Surface Pressure Fluctuations in a Turbulent Boundary Layer in Air at Supersonic Speeds," University of Southampton, AASU Report No. 162, Department of Aeronautics and Astronautics, December 1960.

14. Chyu, W. J., and R. D. Hanly, "Power and Cross-spectra and Space Time Correlation of Surface Fluctuating Pressures at Mach Numbers Between 1.6 and 2.5," AIAA Preprint No. 68-77, January 1968.

15. Maestrello, L., "Measurement and Analysis of the Response Field of Turbulent Boundary Layer Excited Panels," J. Sound and Vib., $\underline{2}$ (3), July 1965.

16. Willmarth, W. W., and C. E. Woolridge, "Measurements of the Fluctuation Pressure at the Wall Beneath a Thick Turbulent Boundary Layer," J. Fluid Mech., Vol. 14, pp. 187-210, 1962.

17. Bozich, D. J., and R. W. White, "Study of the Vibration Responses of Shells and Plates to Fluctuating Pressure Environments," Wyle Laboratories Research Staff Report WR 69-19, September 1969.

18. Robertson, J. E., "Wind Tunnel Investigation of the Effects of Reynolds Number and Model Size on the Steady and Fluctuating Pressures Experienced by Cone Cylinder Missile Configurations at Transonic Speeds," AEDC-TR-66-266, March 1967.

19. Coe, Charles F., "Surface Pressure Fluctuations Associated with Aerodynamic Noise," Basic Aerodynamic Noise Research Conference Proceedings, NASA SP-207.

20. Coe, Charles F., and R. D. Rechtien, "Scaling and Spatial Correlation of Surface Pressure Fluctuations in Separated Flow at Supersonic Mach Numbers," Paper presented at the AIAA Structural Dynamics Aeroelasticity Specialist Conference, New Orleans, La., April 16-17, 1969.

21. Rechtien, Richard D., "A Study of the Fluctuating Pressure Field Regions of Induced Flow Separation at Supersonic Speeds," University of Missouri - Rolla UMR Research Report, May 1970.

22. Robertson, J. E., "Characteristics of the Static- and Fluctuating-pressure Environments Induced by Three-dimensional Protuberances at Transonic Mach Numbers," Wyle Laboratories Research Staff Report WR 69-3, June 1969.

23. Robertson, J. E., "Fluctuating Pressures Induced by Three-dimensional Protuberances," Wyle Laboratories Research Staff Report WR 70-10, April 1970.

24. Chapman, D. R., D. M. Kuehn, and H. K. Larson, "Investigation of Separated Flows in Supersonic and Subsonic Streams with Emphasis on the Effects of Transition," NACA Report 1356.

25. Incompressible Aerodynamics, Oxford at the Claredon Press, 1960.

26. Robertson, J. E., "Prediction of In-flight Fluctuating Pressure Environments Including Protuberance Induced Flow," Wyle Laboratories - Research Staff Report WR 71-10, March 1971.

27. Tu, Bo-Jang, "Prediction of Wall Pressure Fluctuations Beneath a Turbulent Boundary Layer Flow at Supersonic and Hypersonic Speeds," Wyle Laboratories Research Staff Report TM 71-3, September 1971.

28. Plotkin, Kenneth J., "Shock Wave Oscillation Driven by Turbulent Boundary Layer Fluctuations," Wyle Laboratories Research Staff Report WR 72-12, September 1972.

29. Plotkin, Kenneth J., "Prediction of Fluctuating Pressure Environments Associated with Plume-induced Separated Flow Fields," Wyle Laboratories Research Staff Report WR 73-3, May 1973.

30. Robertson, J. E., "Steady and Fluctuating Pressures on Cone-cylinder Missile Configurations at Transonic Speeds," AEDC-TR-65-269, February 1966.

31. Coe, Charles F., and Arthur J. Koskey, "The Effects of Nose Bluntness on the Pressure Fluctuations Measured on 15° and 20° Cone-cylinders at Transonic Speeds," NASA TM X-779, January 1963.

32. Himelblau, Harry, "Aeroacoustic, Vibration and Shock Environments for the Space Shuttle Orbiter," Paper presented at Space Shuttle Dynamics and Aeroelasticity Technology Working Group Meeting, Ames Research Center, Moffet Field, California, November 8-9, 1971.

33. Robertson, J. E., "Preliminary Estimates of Space Shuttle Fluctuating Pressure Environments," Wyle Laboratories Research Staff Report WR 72-10, August 1972.

34. Dobs, Jules B., Jr., and Richard D. Hanly, "In-flight Aeroacoustic Environments on Prospective Space Shuttle Vehicles," Published in Proceedings of NASA Space Materials, San Antonio, Texas, April 12-14, 1972, NASA TM X-2570.

35   Plotkin, Kenneth J., and J. E. Robertson, "Prediction of Space Shuttle Fluctuating Pressure Environments, Including Rocket Plume Effects," Wyle Laboratories Research Staff Report WR 73-6, June 1973.

36. Preliminary Data, 0.040 Scale Integrated Space Shuttle Model 11-OTS Wind Tunnel Tests, NASA Ames Research Center Unitary Plan Wind Tunnel, August 1973.

37. Mission 1 Ascent Trajectories for November 1974 Performance Assessment, Rockwell International Corporation, November 26, 1974.

○ Chyu and Hanly (Ames-Cylinder data; X/D 2.9) Ref. 14
● Unpublished Ames-Tunnel Wall Data, Ref. 19
□ Speaker and Ailman-Tunnel Wall data, Ref. 2
△ Belcher - Flight data, Ref. 6
◇ Kistler and Laufer, Ref. 19
◁ Williams - Tunnel Wall Data, Ref. 13
▽ Bull, et al.,-Tunnel Wall data, Refs. 3 and 4
▽ Bull and Willis - Tunnel wall data, Ref. 19
◇ Willmarth and Roos-Tunnel wall data, Ref. 10
□ Serafini-Tunnel wall data, Ref. 7
◆ Willmarth and Woolridge - Tunnel wall data, Ref. 16
✹ Unpublished XB-70 flight data, Ref. 19
■ Maestrello-Tunnel wall data, Ref. 15

$\sqrt{\overline{p^2}}/q_\infty$

0.04

0.02

0.01

0.006

0.004

0.002

0.001

0   1   2   3

M_∞

Equation 1

Figure 1. Comparison of Pressure Fluctuation Measurements by Various Investigators for Attached Turbulent Boundary Layers

23

	Coe and Rechtien, 45° Conical Frustrum
□	
△	Coe and Rechtien, 45° Wedge
◇	Chyu and Hanly, 45° Conical Frustrum
▲	Coe and Nute, 34° Boattail
●	Robertson, 25° Cone-Cylinder
◆	Robertson, 30° Cone-Cylinder
⬥	Andrews, 17.5° Boattail
	Coe's Unpublished Data for Rearward Facing Step
– –	Attached Turbulent Boundary Layer, Equation (1)
☐	Coe's Unpublished Data for Compression Corners as Presented by Lowson

Compression Corners

Expansion Corners

Figure 2. Variation of Fluctuating Pressure Level for Homogeneous Separated Flow
with Mach Number

24
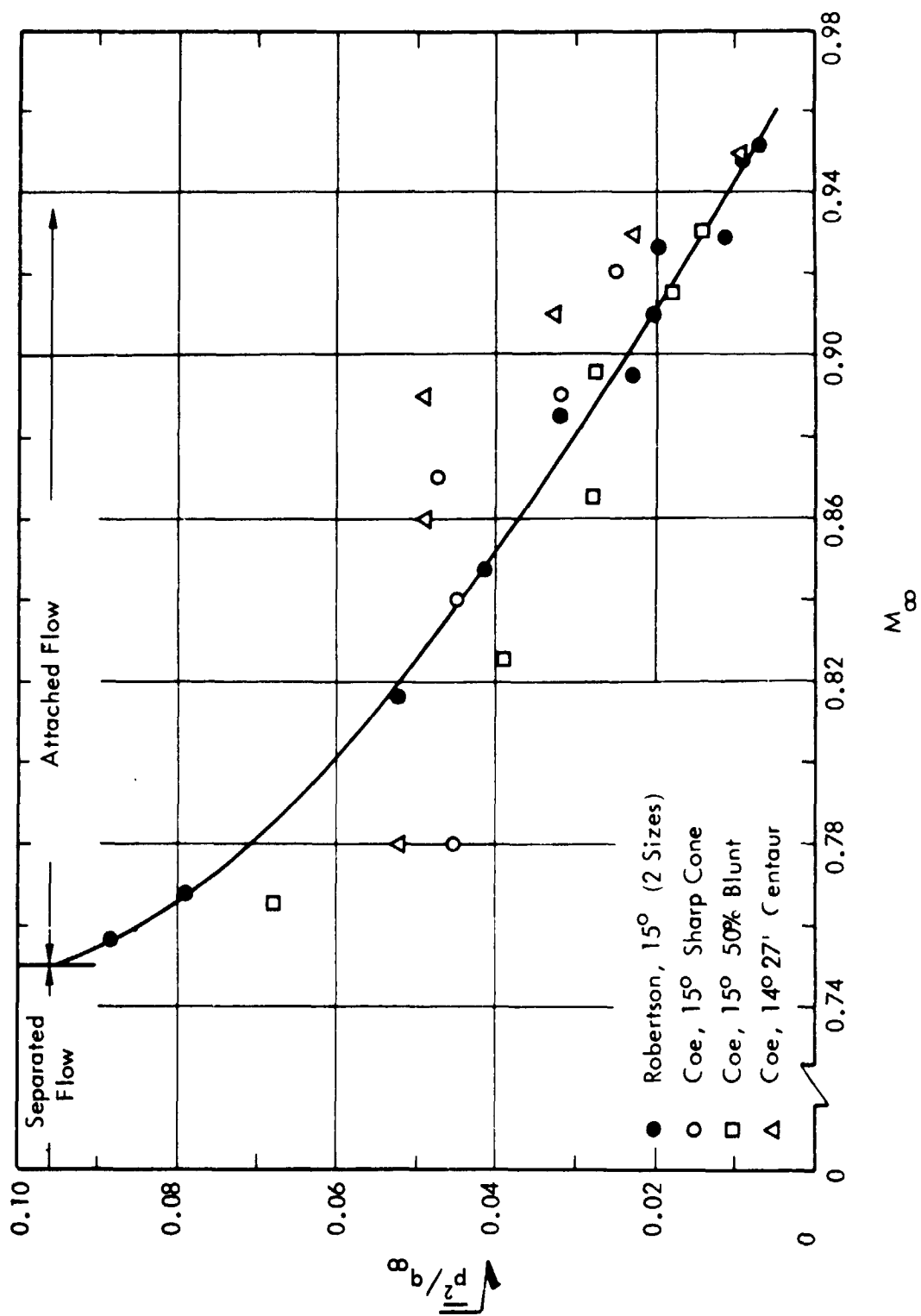
Figure 3. Variation of Fluctuating Pressure Level for Shock-Wave Oscillation with Mach Number

25
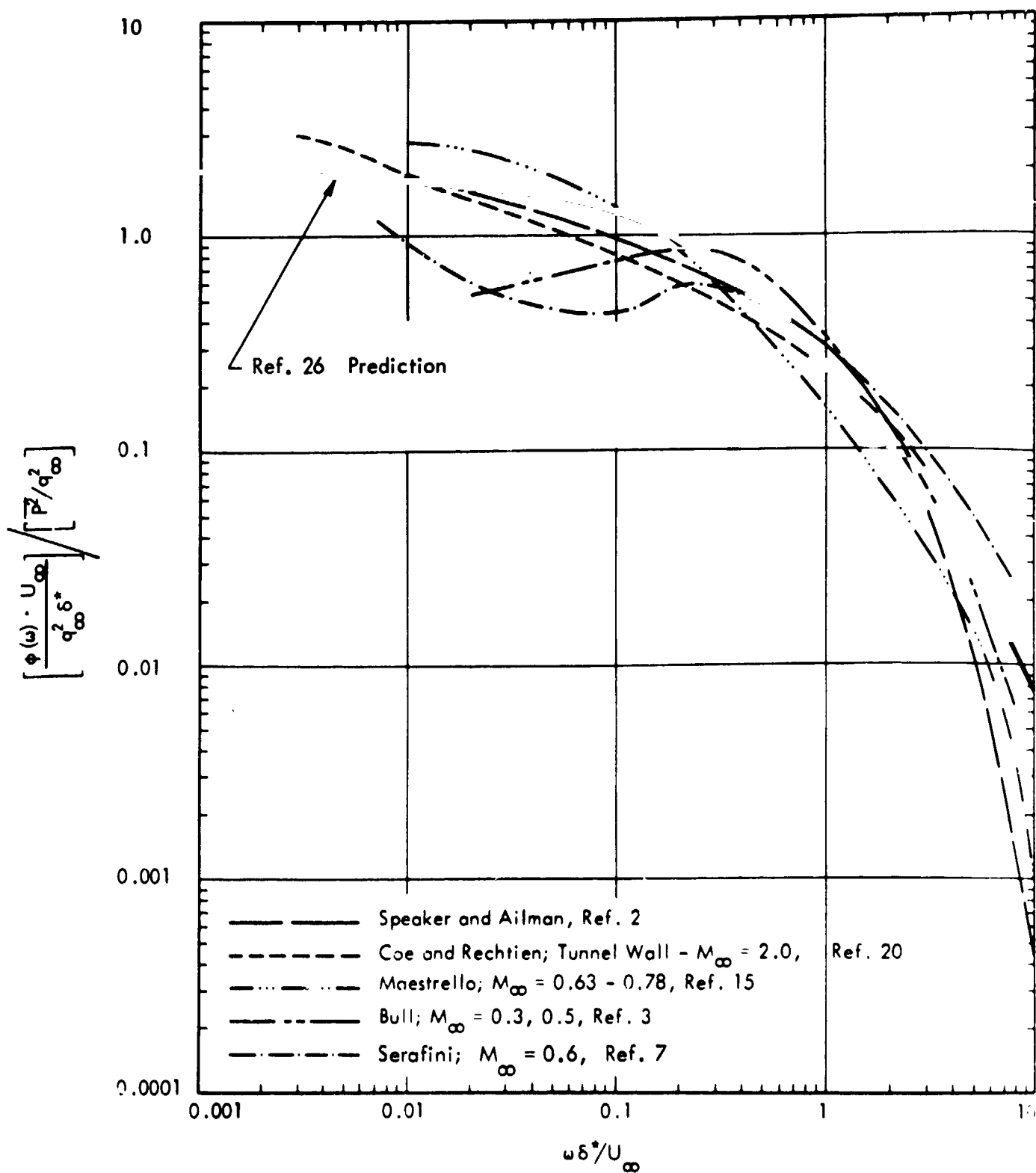
Figure 4. Power Spectra for Turbulent Boundary Layer Fluctuating Pressures
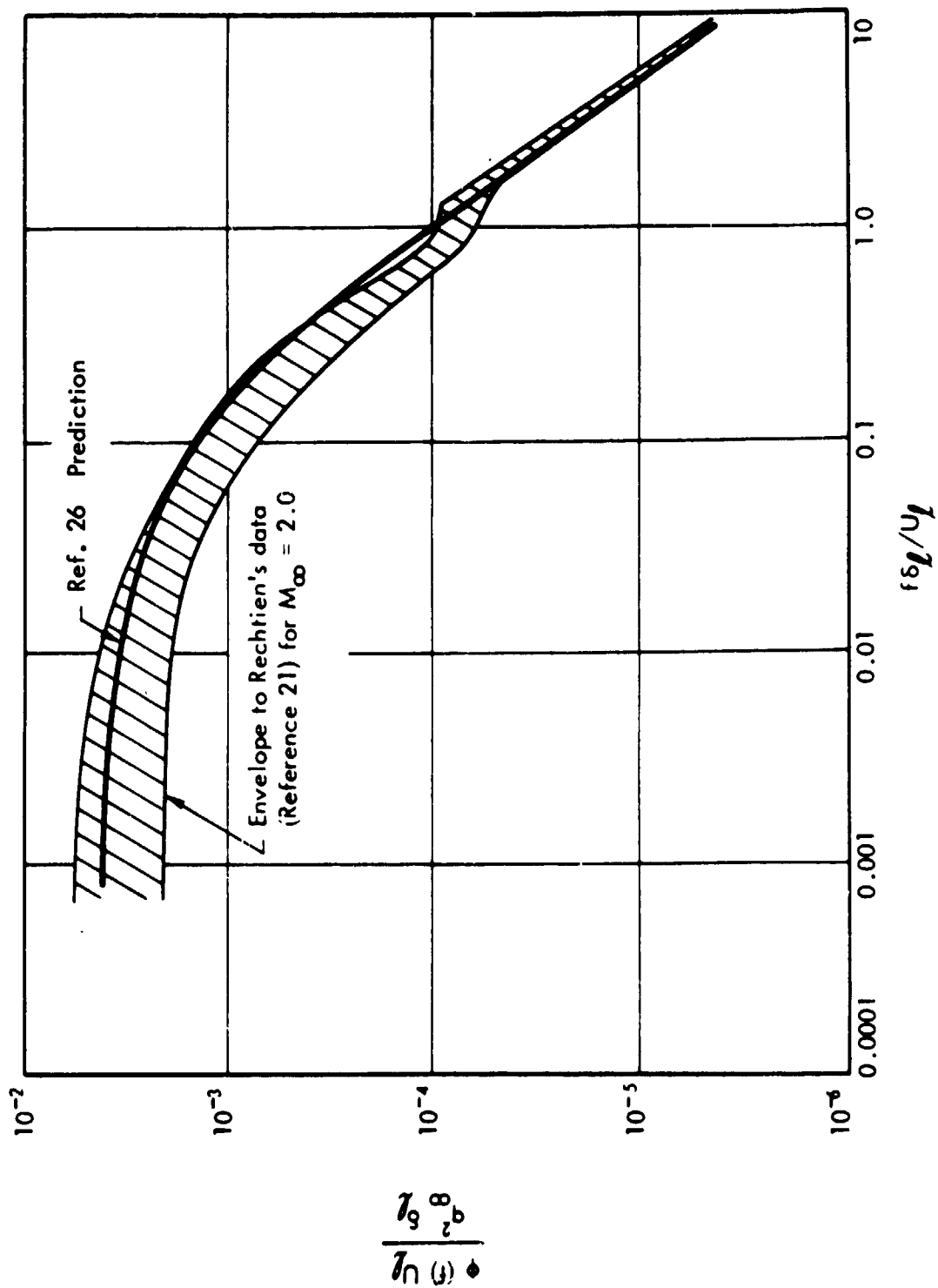
Figure 5. Power Spectrum of Fluctuating Pressures within Homogeneous Separated Flow Regions
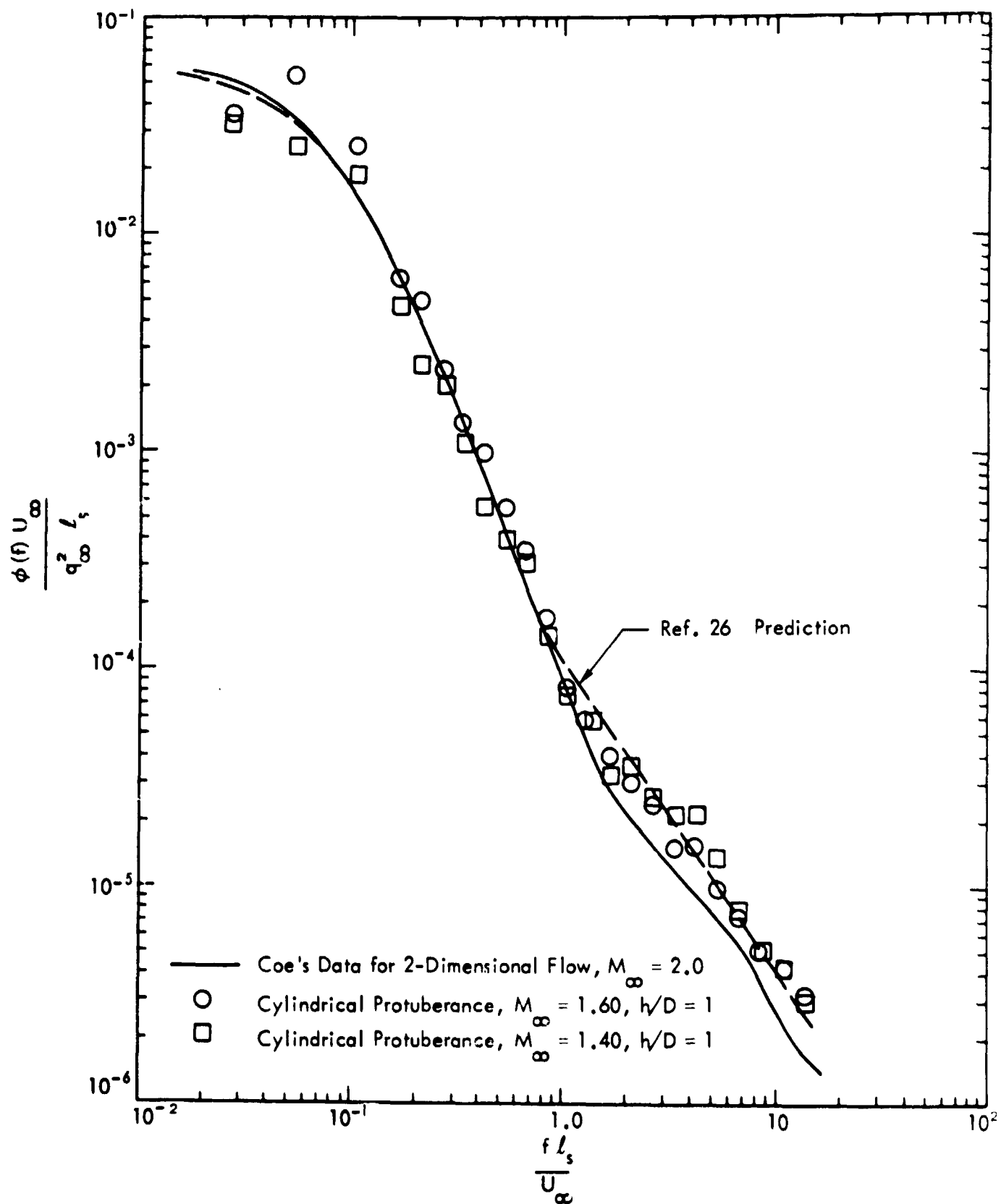
Figure 6. Comparison of Predicted and Measured Power Spectra for Shock-Wave Oscillation Upstream of Two- and Three-Dimensional Separated Flow Fields

28
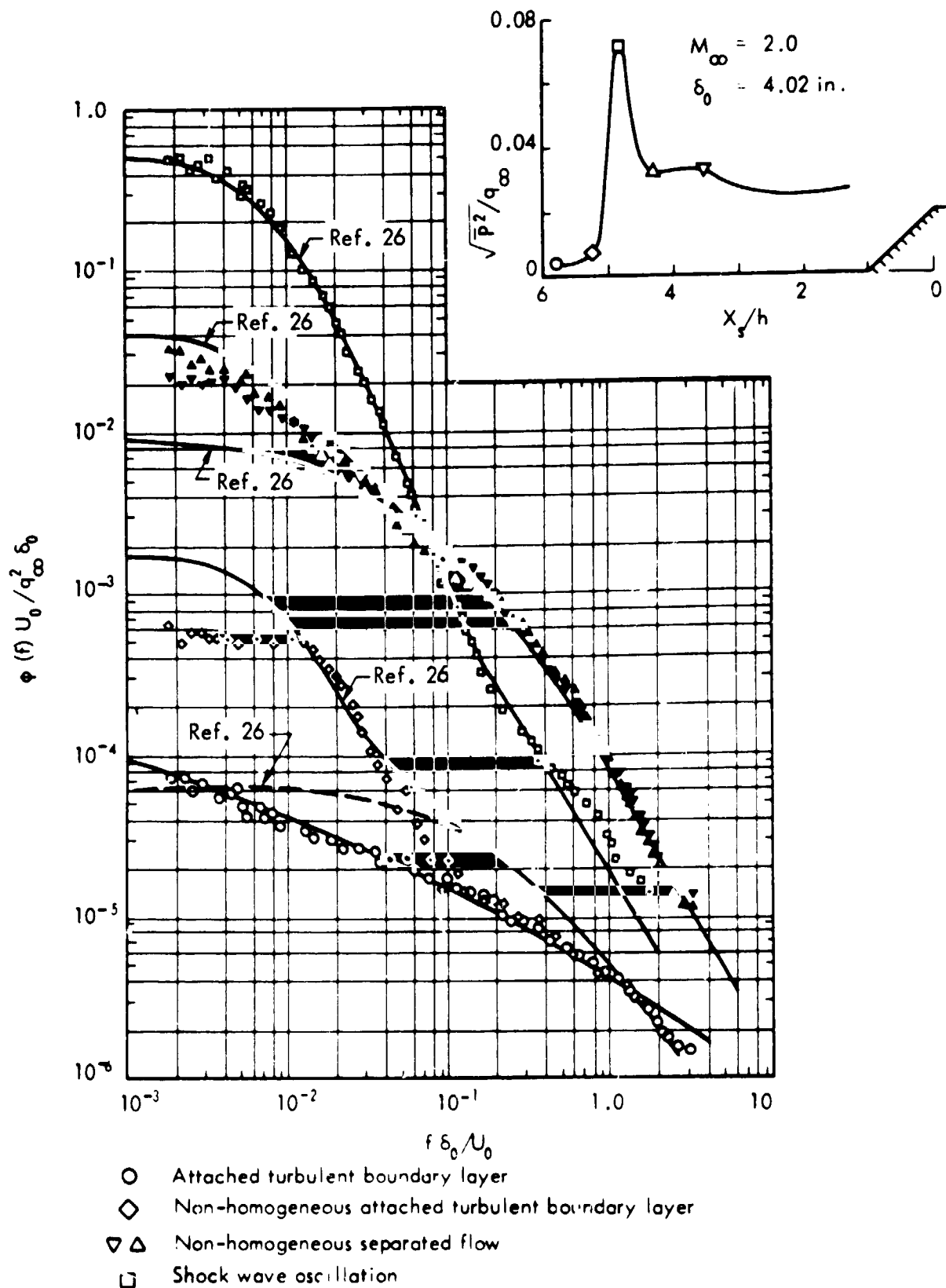
Figure 7. Longitudinal Distribution of Pressure Fluctuations and Typical Power Spectra in Vicinity of Supersonic Flow Separation Ahead of a 45° Wedge

○   Attached turbulent boundary layer

◇   Non-homogeneous attached turbulent boundary layer

▽ △   Non-homogeneous separated flow

⊔   Shock wave oscillation
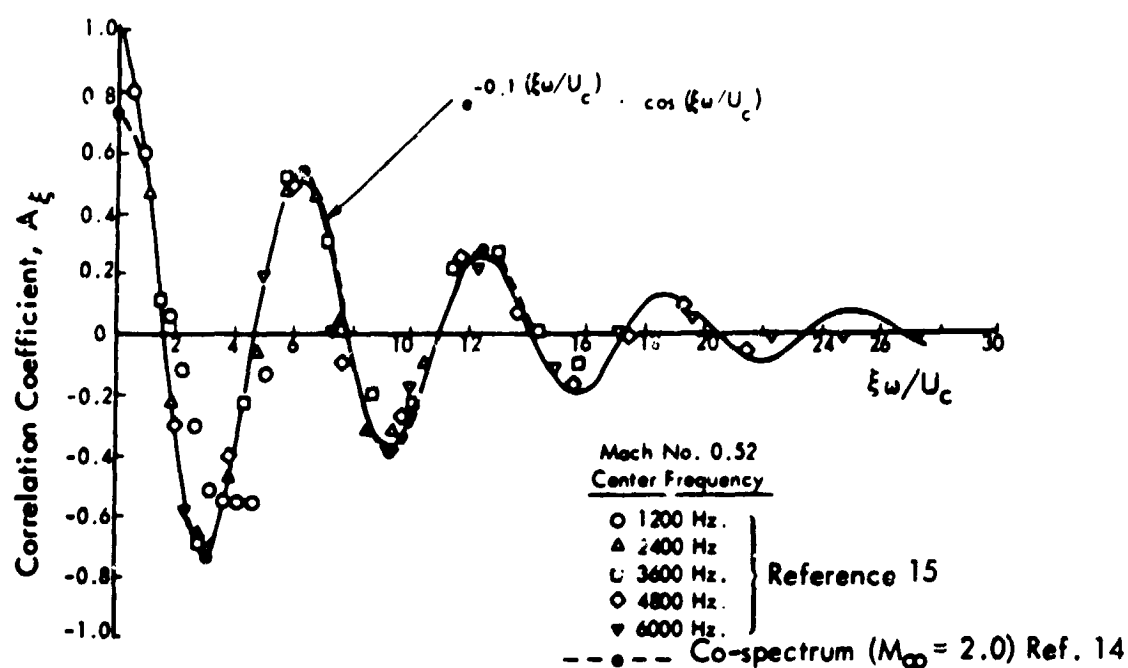
Figure 8(a). Narrow Band Longitudinal Space Correlation Coefficient
for Boundary Layer Fluctuating Pressures
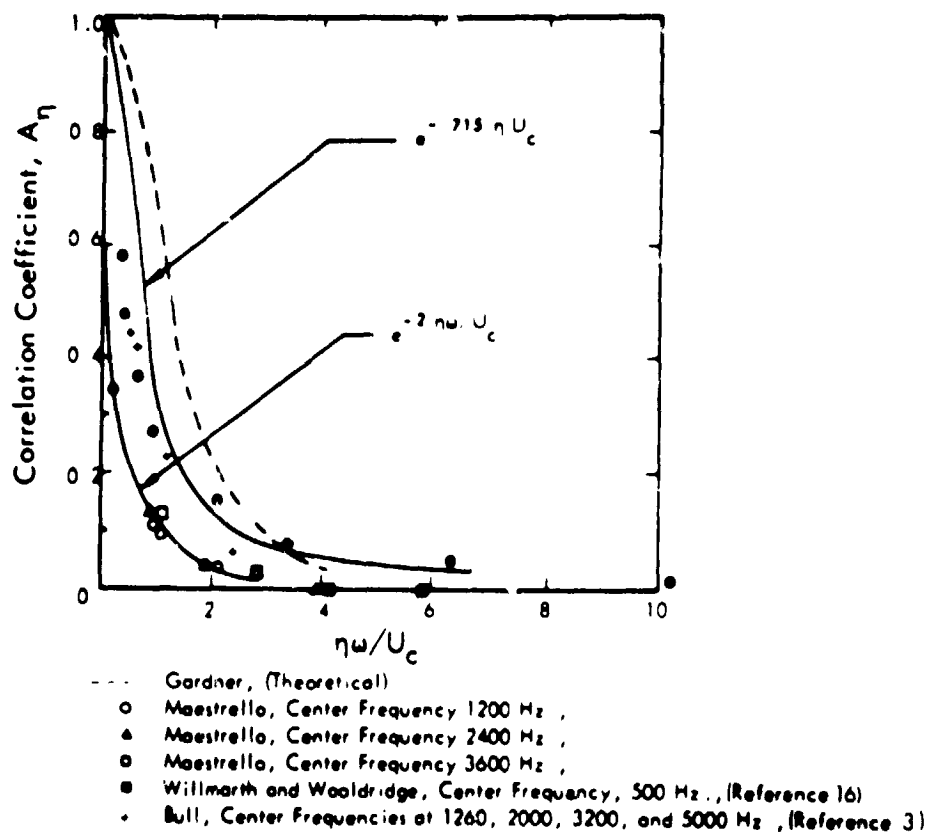
Figure 8(b). Narrow Band Lateral Space Correlation Coefficient for
Boundary Layer Fluctuating Pressures
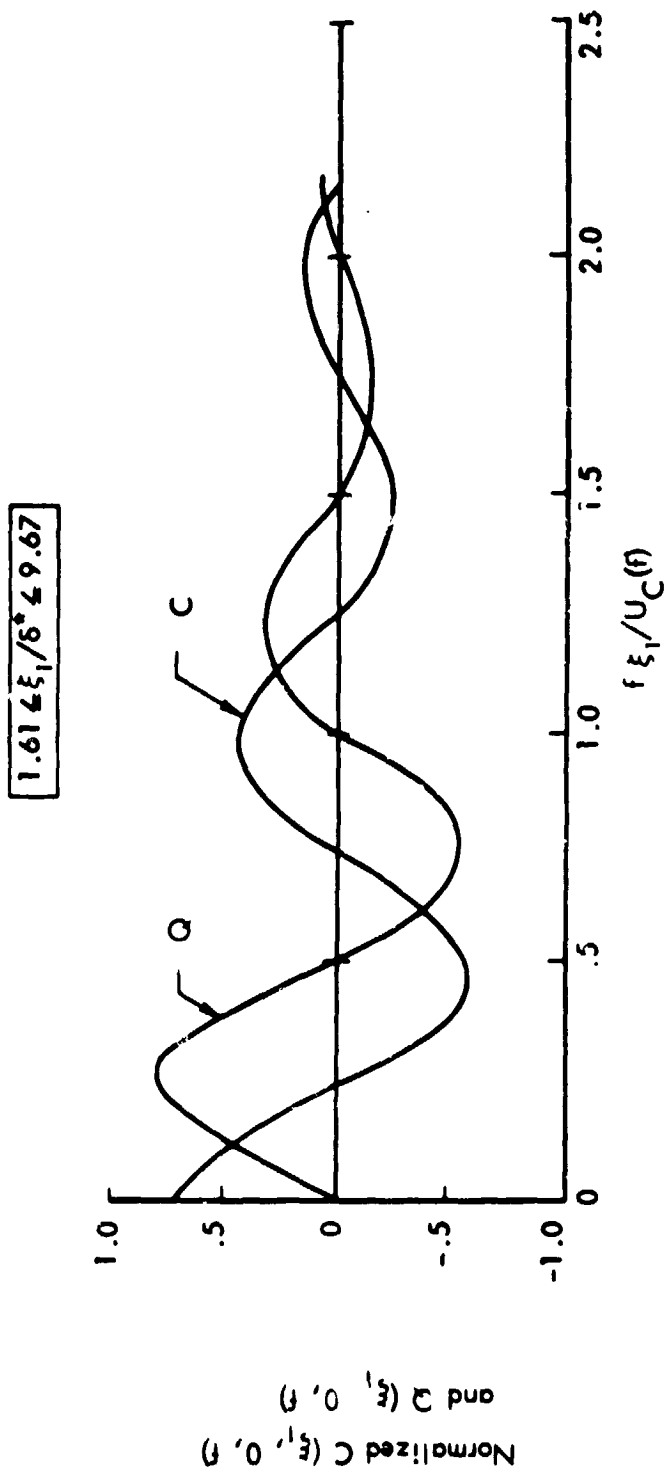
Figure 9.   Typical Longitudinal Cross-Spectra of Pressure Fluctuations for Separated Flow (Ref. 14)

$1.61 \leq \xi_1/\delta^* \leq 9.67$

$f\xi_1/U_C(f)$

Normalized $C(\xi_1, 0, f)$ and $Q(\xi_1, 0, f)$

31

Shoulder-Induced Separated Flow

Subsonic Mach Numbers

$$\left(M_\infty < M_a \right)$$

$$X_{sw} = f\left(M_\infty, \theta_N \right)$$

X_{sw}

Shock-Wave Oscillation

θ_N

D

Transonic Mach Numbers

$$M_a < M_\infty < 1.0$$

X_s Attached Flow

D

$$M_\infty \geq 1.0$$
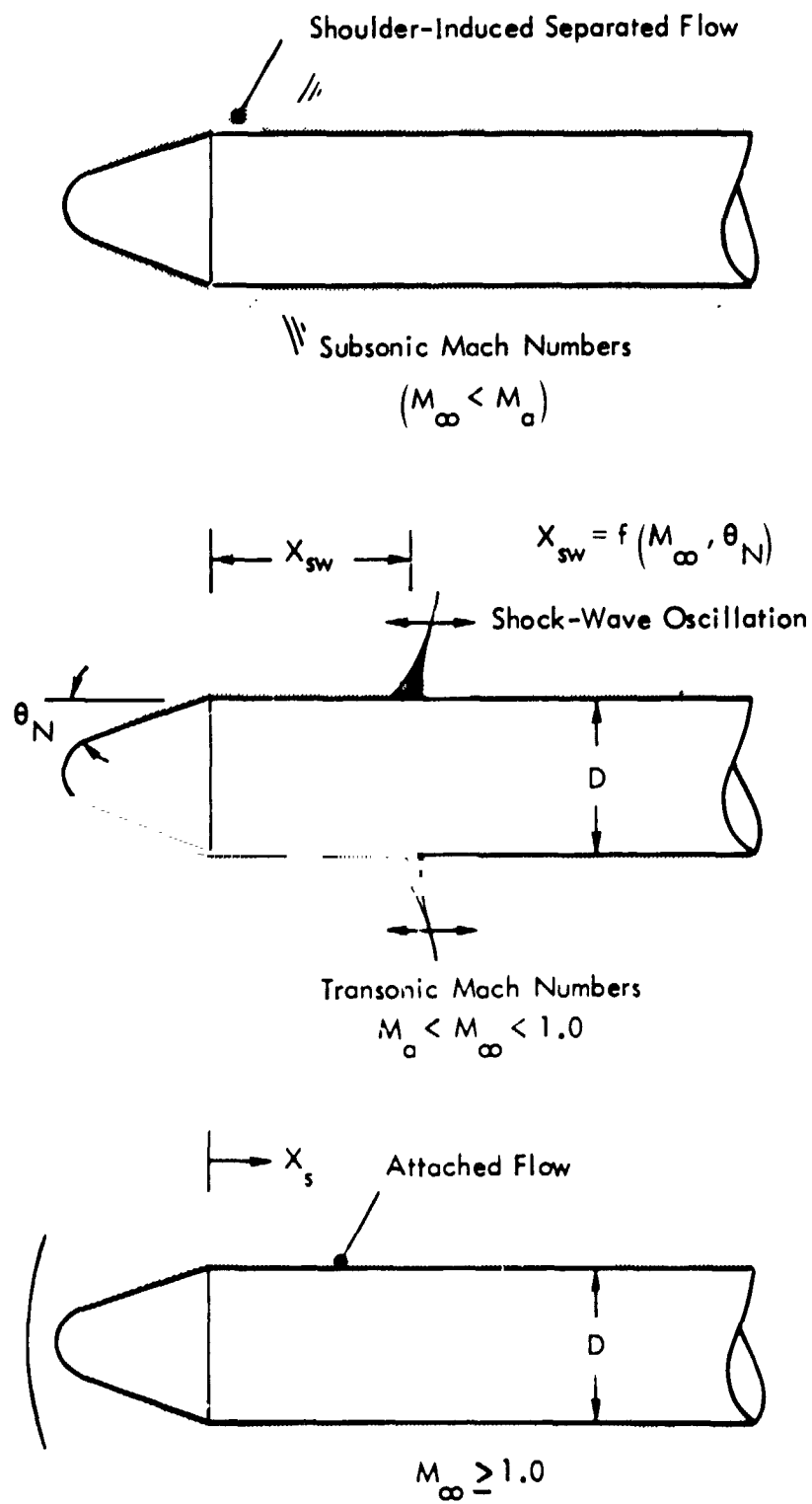
Figure 10. Schematic of Interference-Free Flows Over
a Cone-Cylinder Body
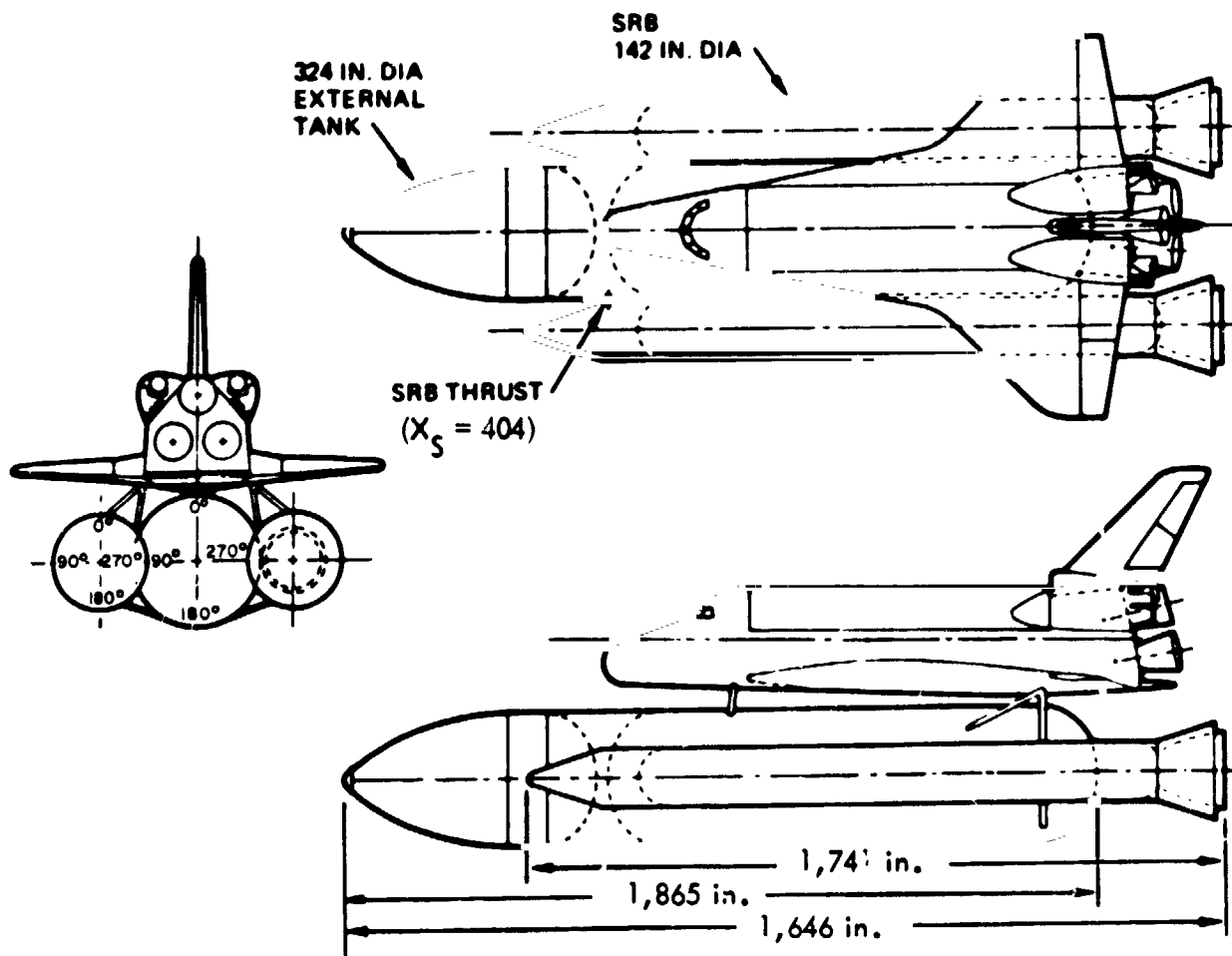
Figure 11. Schematic of Baseline Shuttle Launch Configuration

33
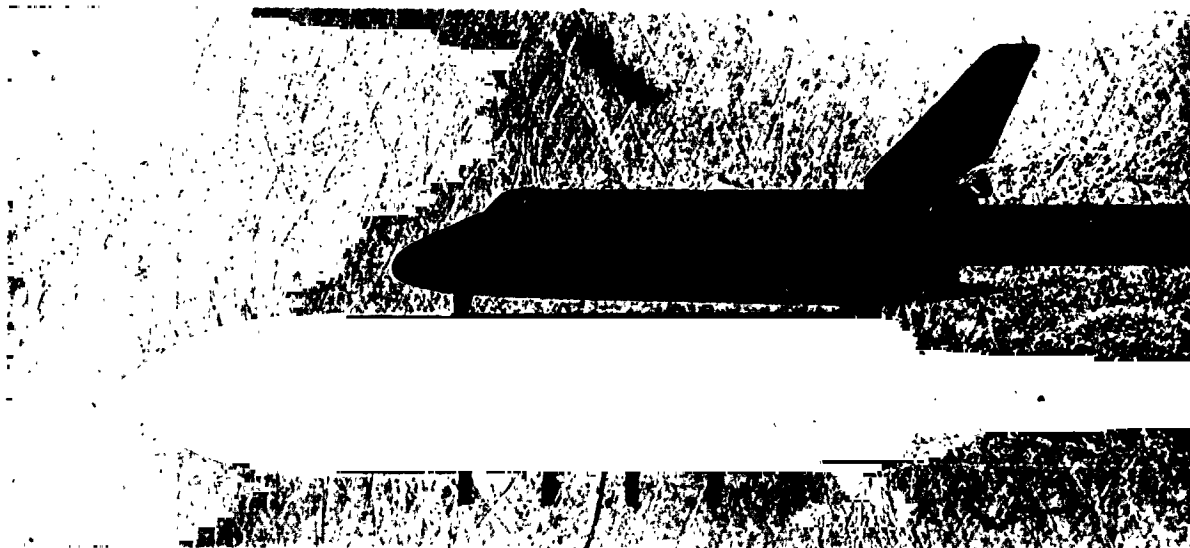
Side View

Top View

Figure 12. Wind Tunnel Shadowgraphs of the Space Shuttle
Launch Configuration

$$M_\infty = 0.80$$

34
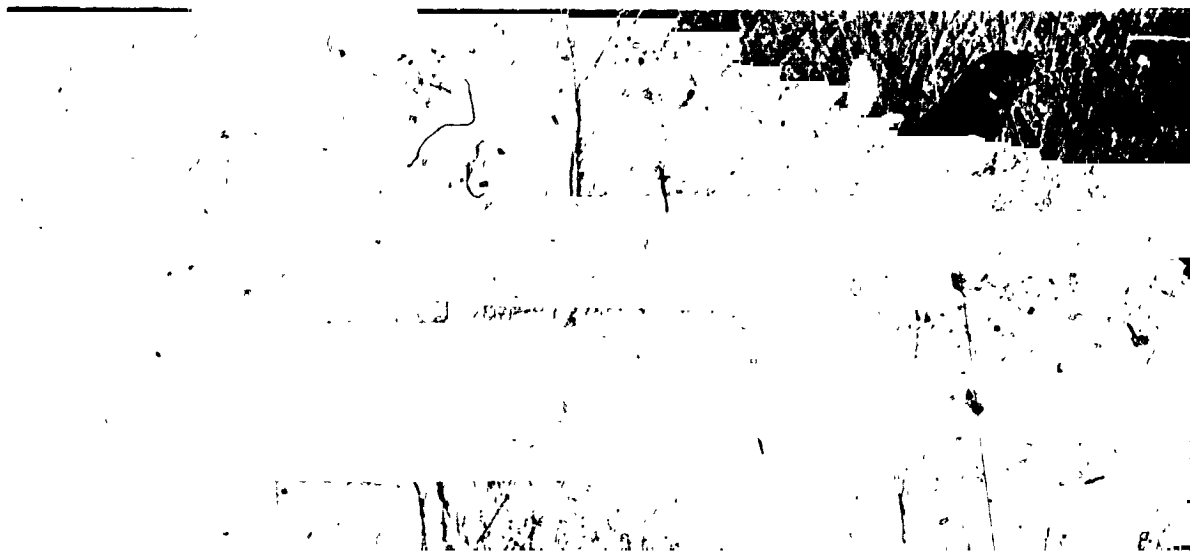
Side View

Top View

Figure 12. Continued

$M_\infty = 0.90$

Side View

Top View

Figure 12. Continued

$M_\infty = 0.95$
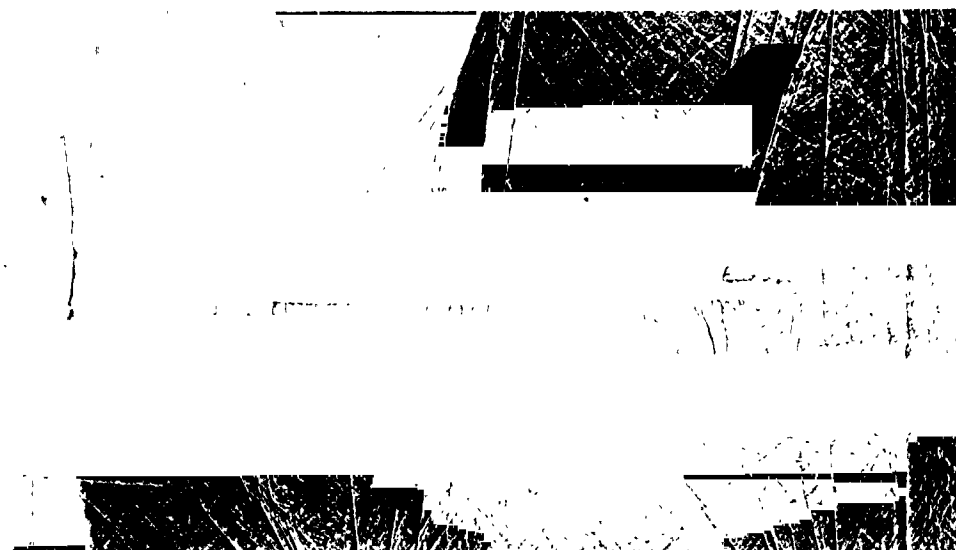
Side View

Top View

Figure 12. Continued

$M_\infty = 1.00$
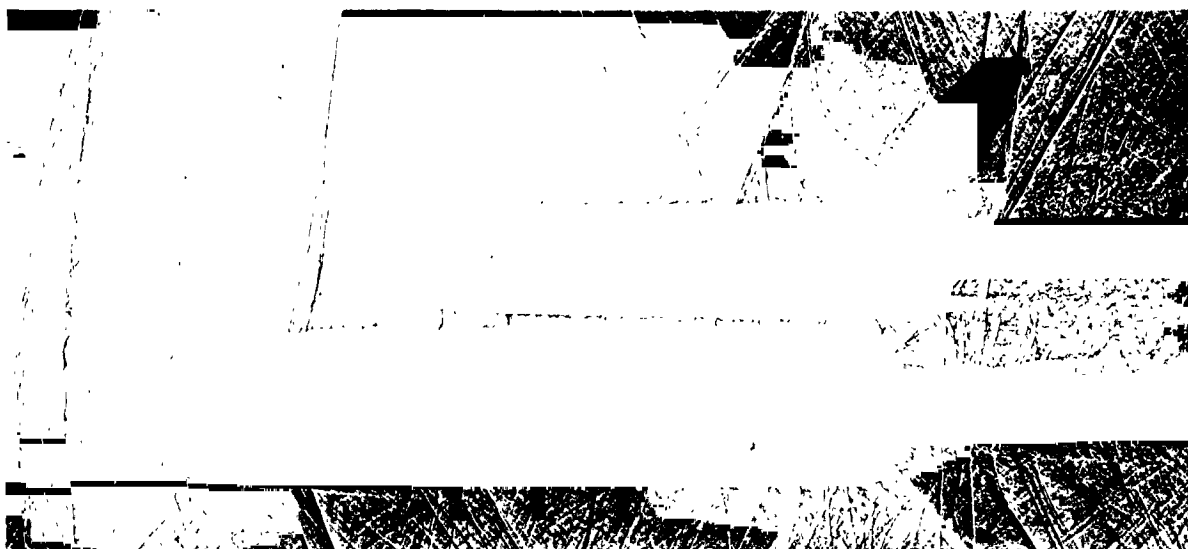
Side View
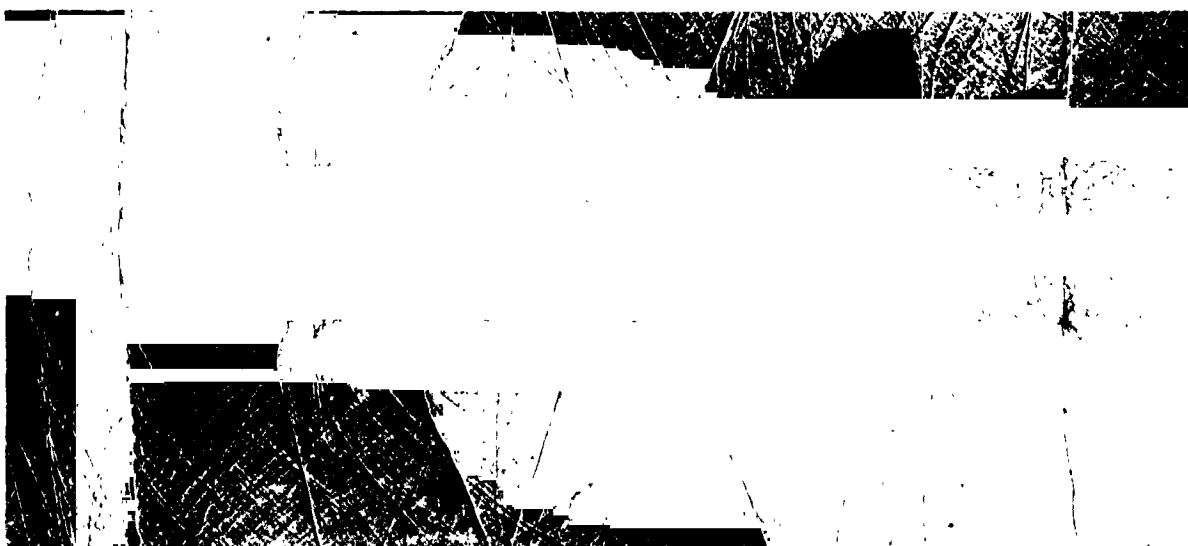
Top View

Figure 12. Continued

$M_\infty = 1.10$

38

Side View

Top View

Figure 12. Continued

$M_\infty = 1.20$

39

Side View

Top View

Figure 12. Continued

$M_\infty = 1.46$

Side View
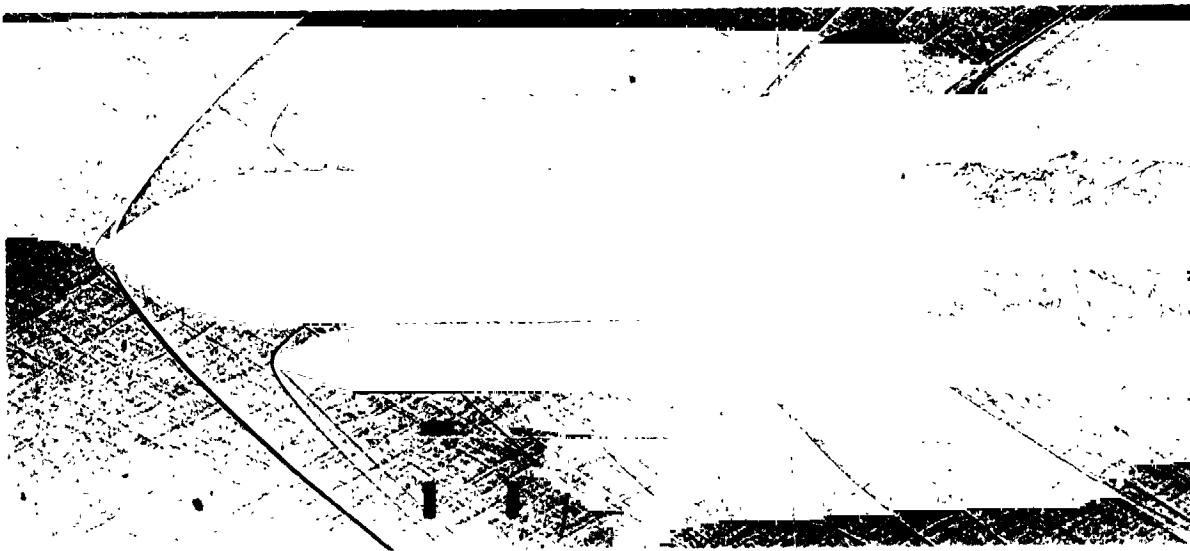
Top View

Figure 12. Continued

$M_\infty = 1.96$
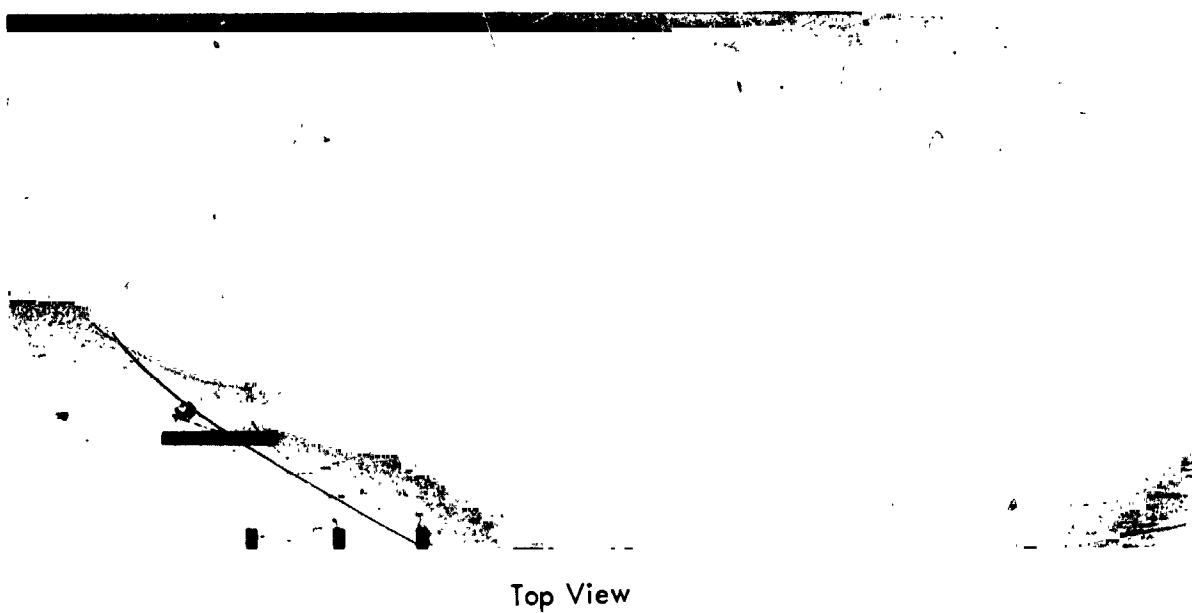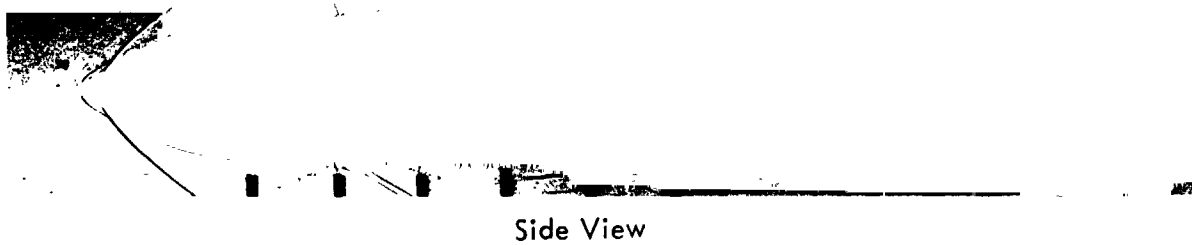
Side View

Top View

Figure 12. Concluded

$M_\infty = 2.99$

42
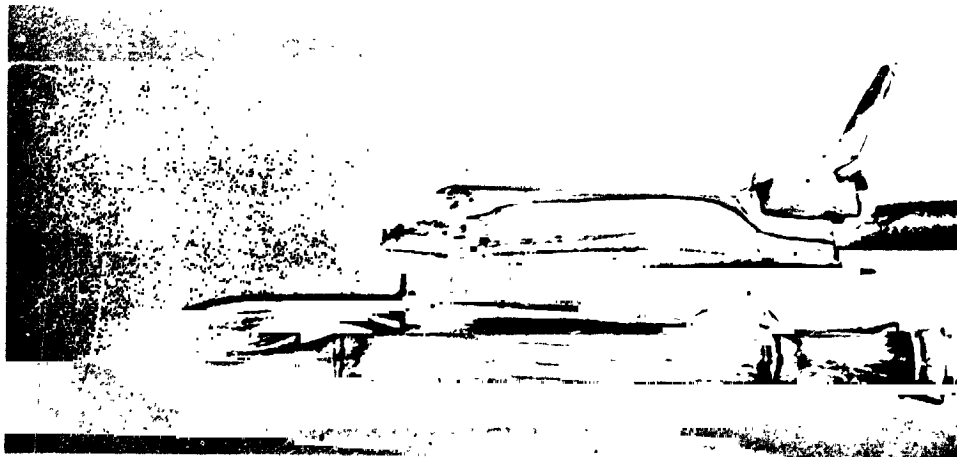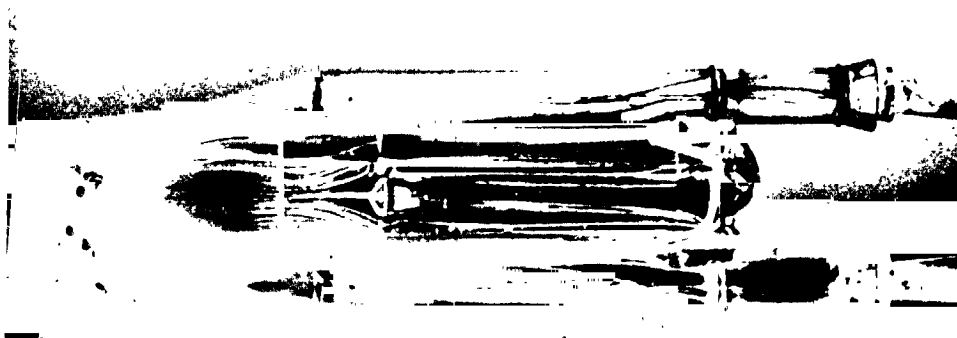
Side View

Top View (Orbiter Removed)
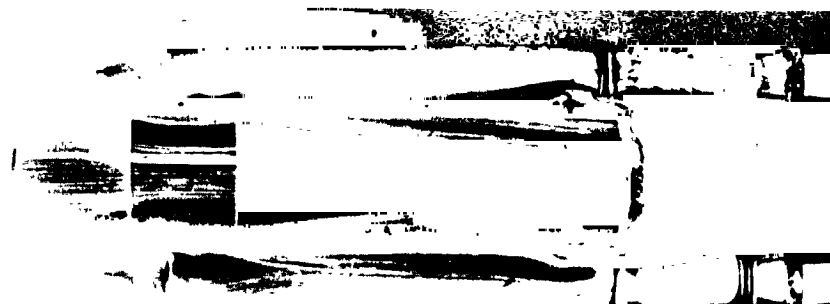
Bottom View (Orbiter Removed)

Figure 13. Wind Tunnel Oil Flow Photographs of Space Shuttle
Launch Configuration

$$M_\infty = 0.80$$
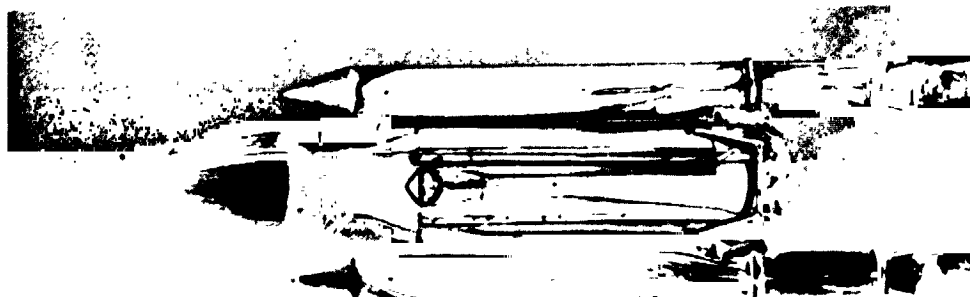
43

Side View

Top View (Orbiter Removed)

Bottom View (Orbiter Removed)

Figure 13. Continued

$M_\infty = 0.90$
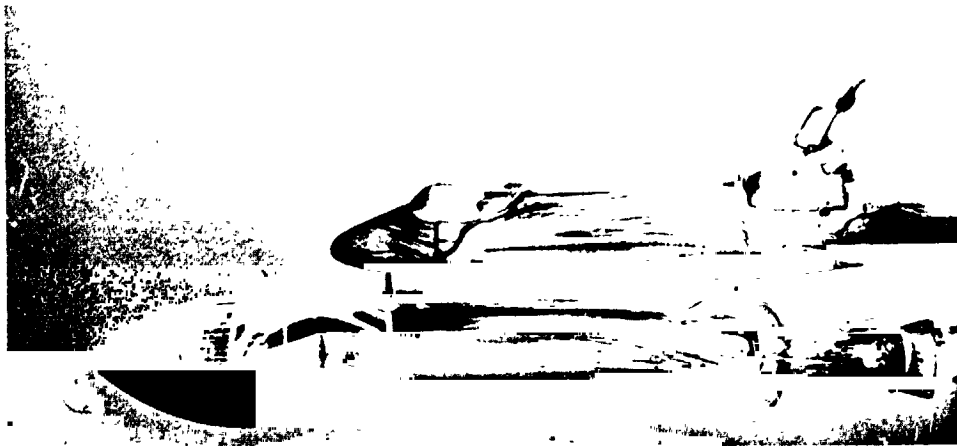
44

Side View

Top View (Orbiter Removed)

Bottom View (Orbiter Removed)

Figure 13. Continued

$M_\infty = 0.95$

Side View

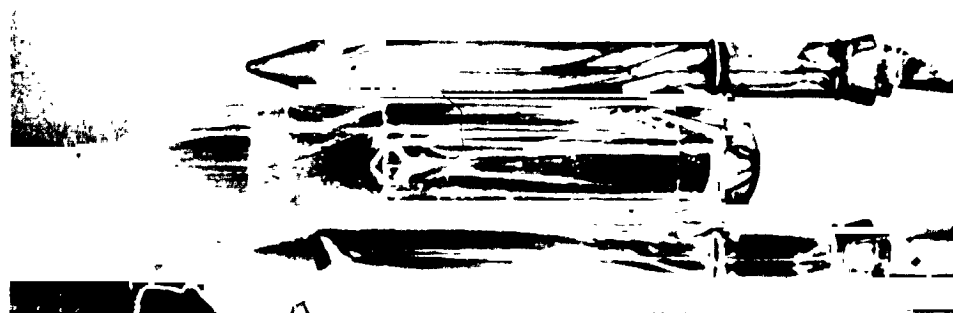Top View (Orbiter Removed)

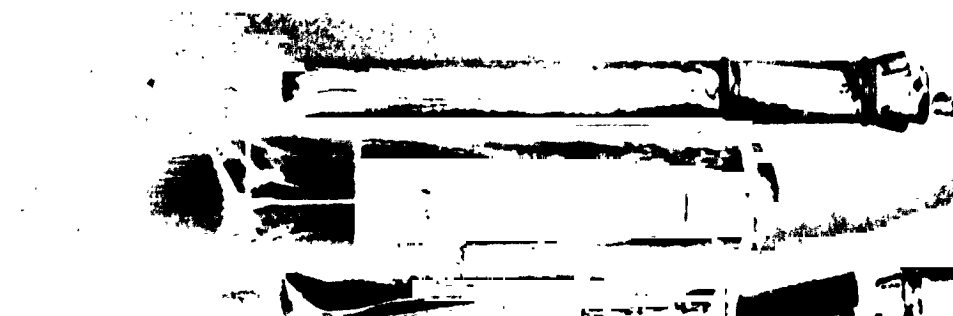Bottom View (Orbiter Removed)

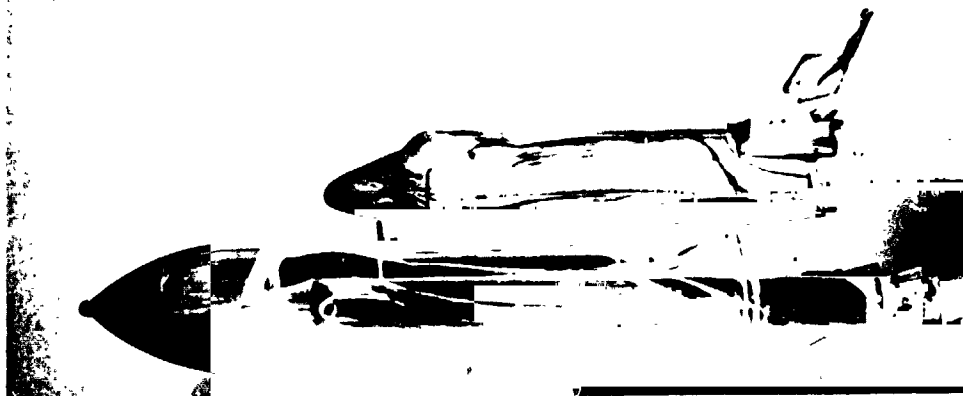Figure 13. Continued

$M_\infty = 1.00$

46

Side View

Top View (Orbiter Removed)

Bottom View (Orbiter Removed)

Figure 13. Continued

$$M_\infty = 1.10$$

Side View

Top View (Orbiter Removed)

Bottom View (Orbiter Removed)

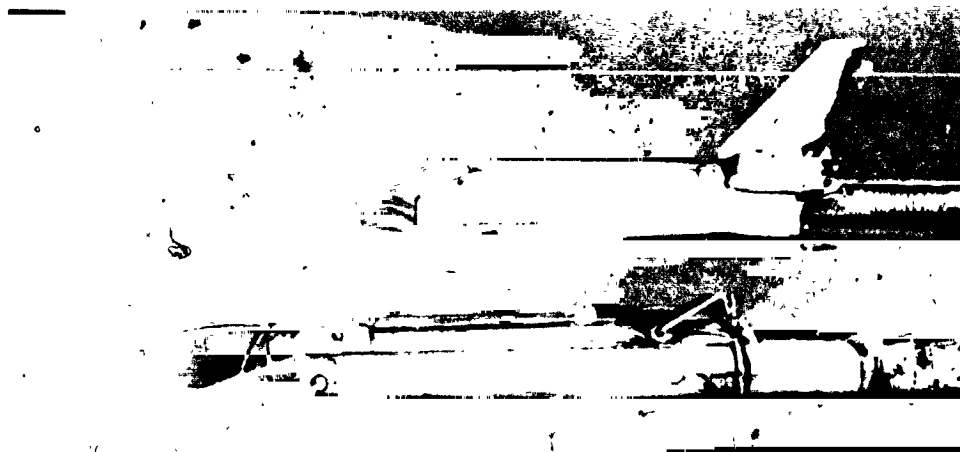Figure 13. Continued

$$M_\infty = 1.20$$

48

Side View

Top View (Orbiter Removed)
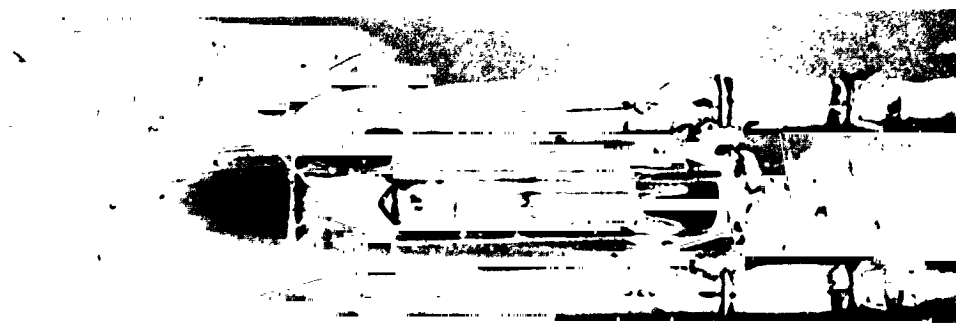

Bottom View (Orbiter Removed)

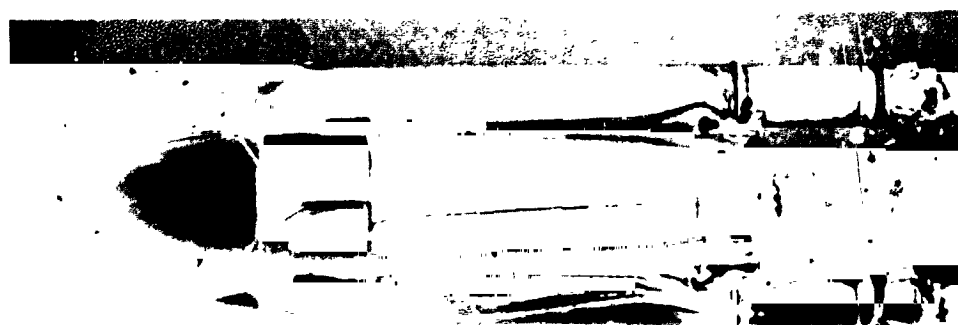Figure 13. Continued

M_∞ - 1.46
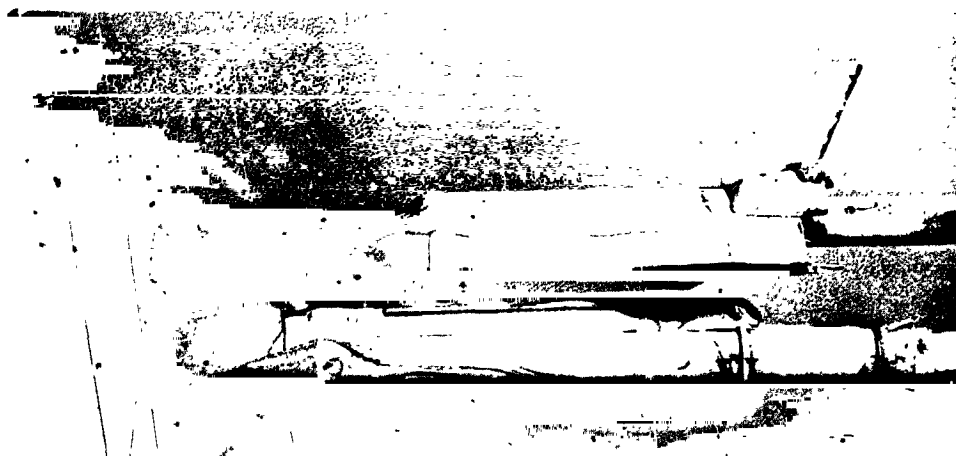
Side View
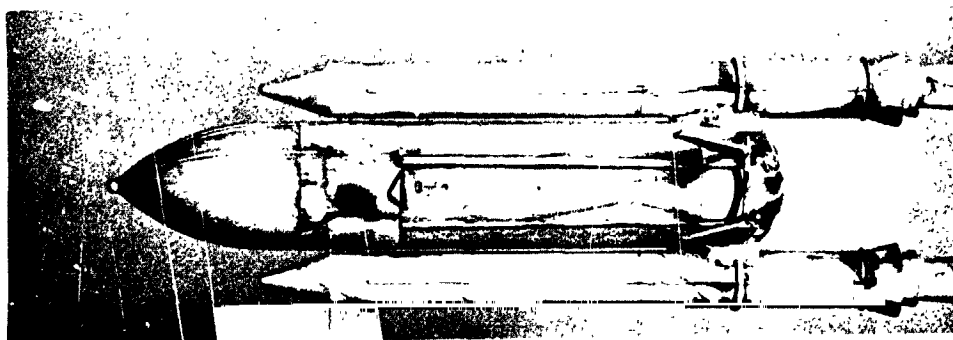
Top View (Orbiter Removed)
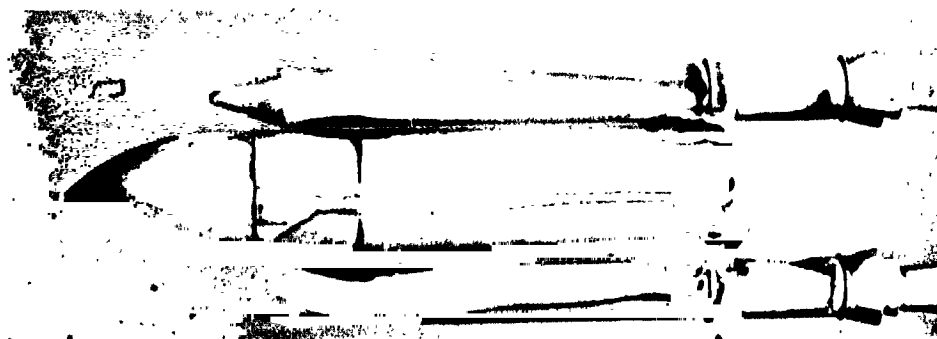
Bottom View (Orbiter Removed)

Figure 13. Continued

$M_\infty = 1.96$
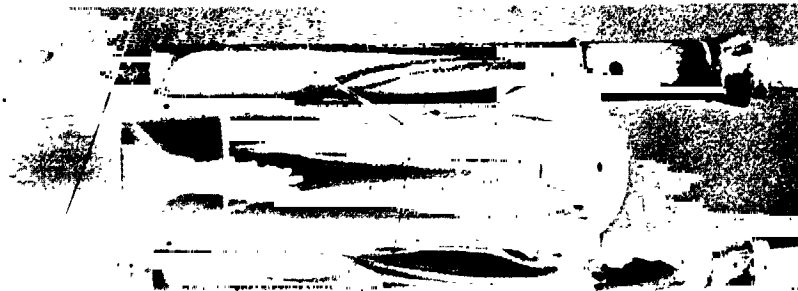
Bottom View (Orbiter Removed)
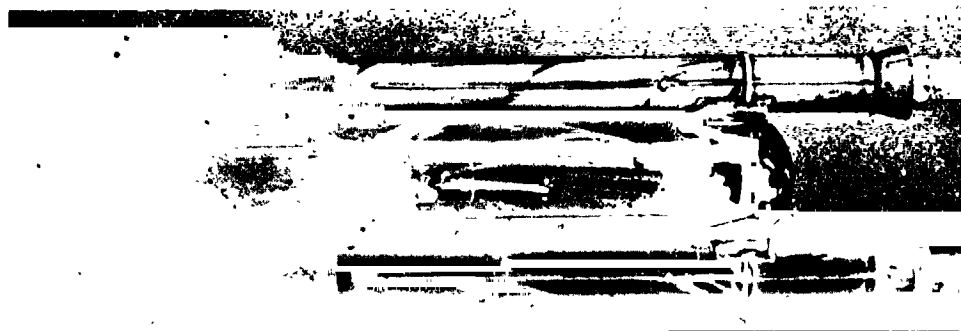
Top View (Orbiter Removed)

Figure 13. Concluded

$M_\infty = 2.99$
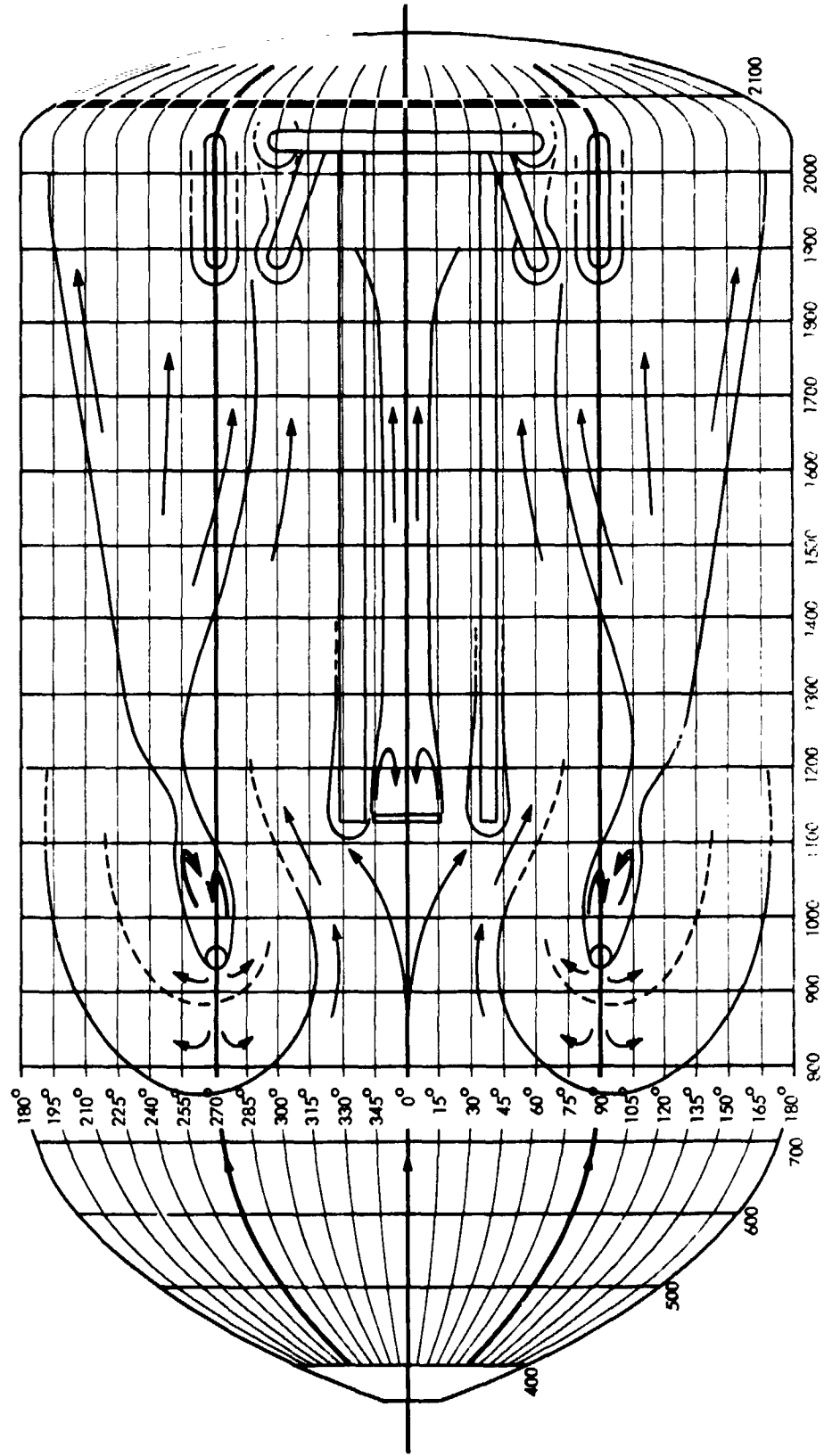
Figure 14. External Tank Flow Diagrams for Space Shuttle Launch Configuration

$M_\infty = 0.80$
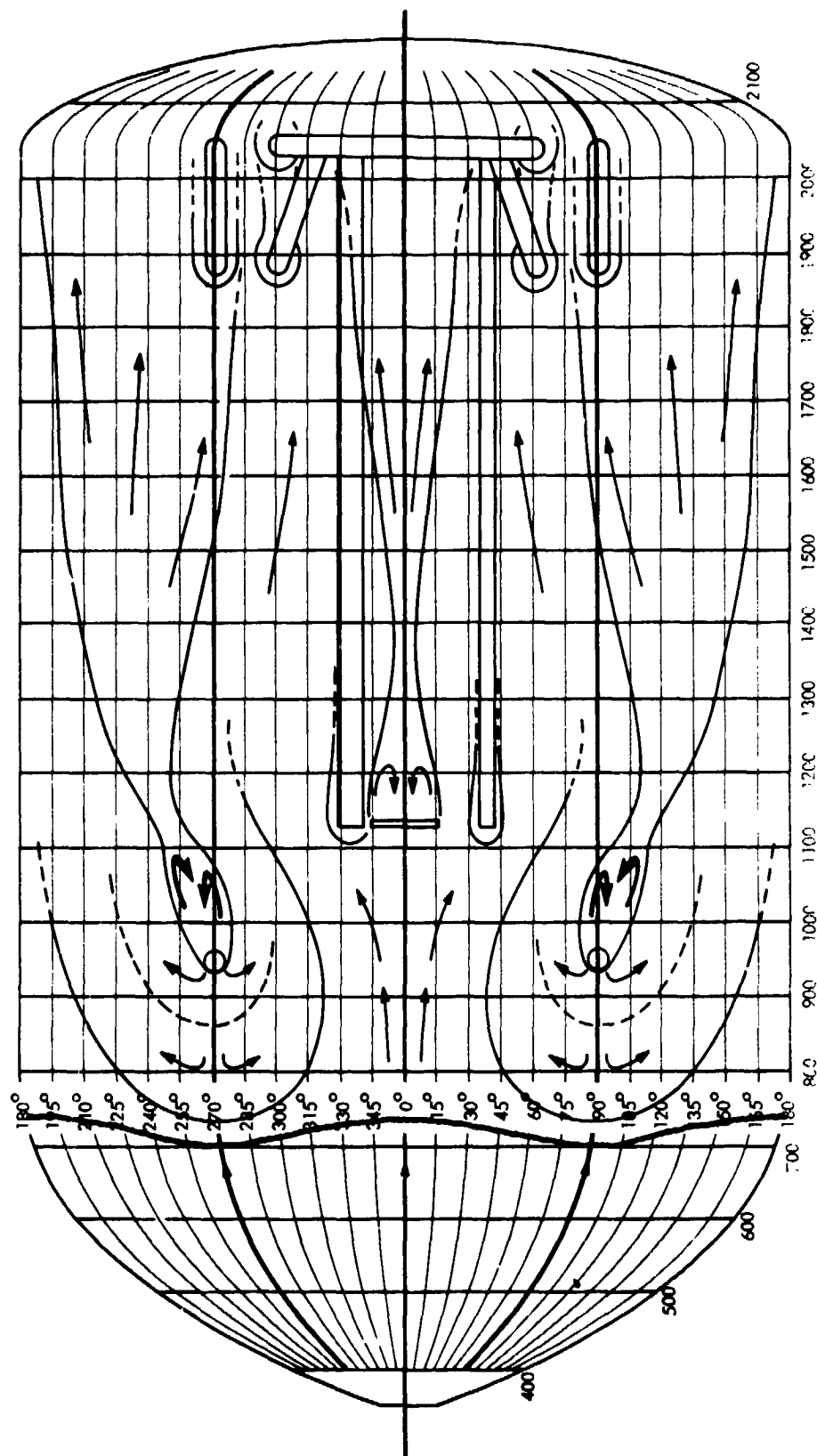
Figure 14. Continued

$M_\infty = 0.90$
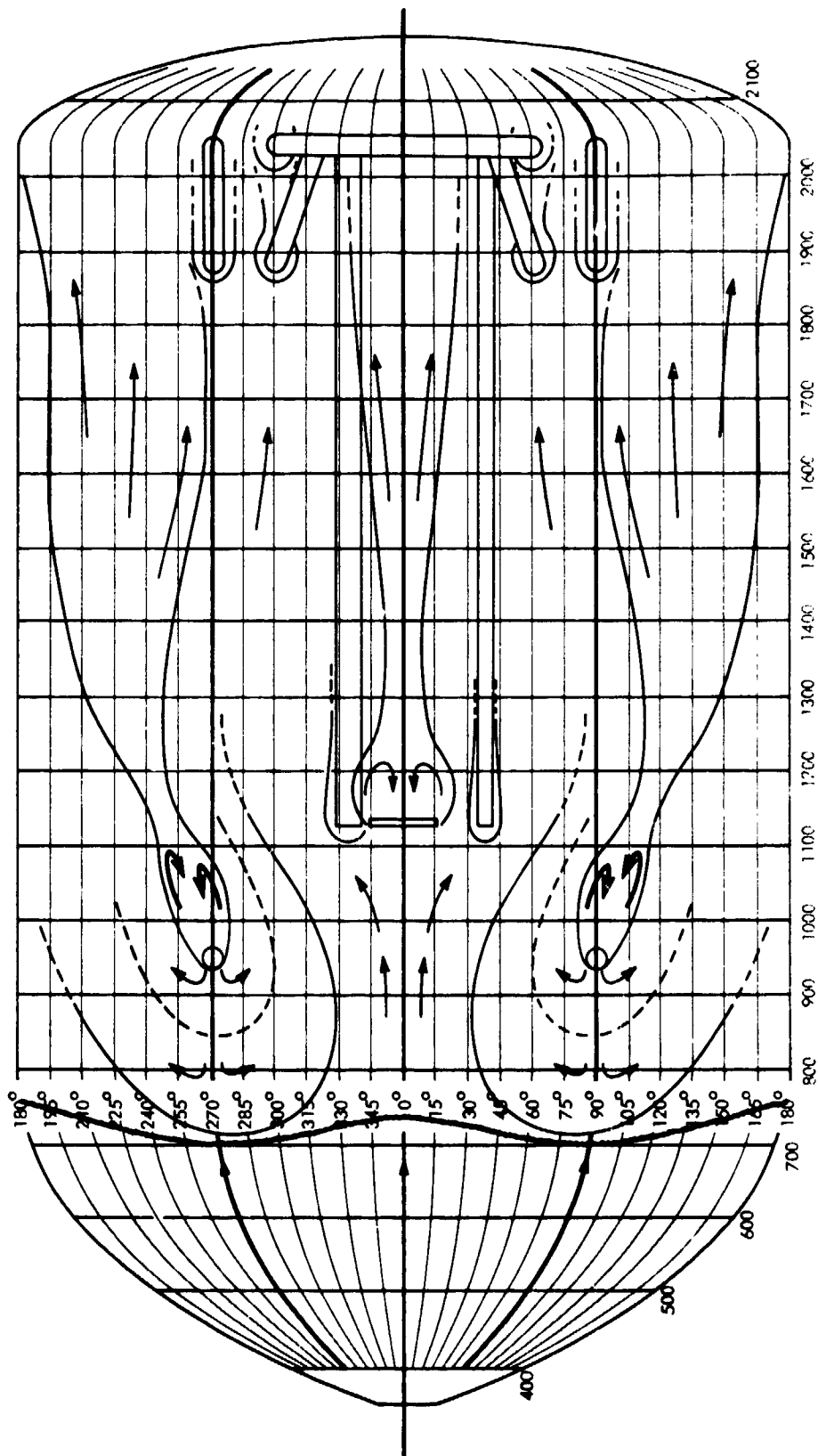
Figure 14. Continued

$M_\infty = 0.95$

54
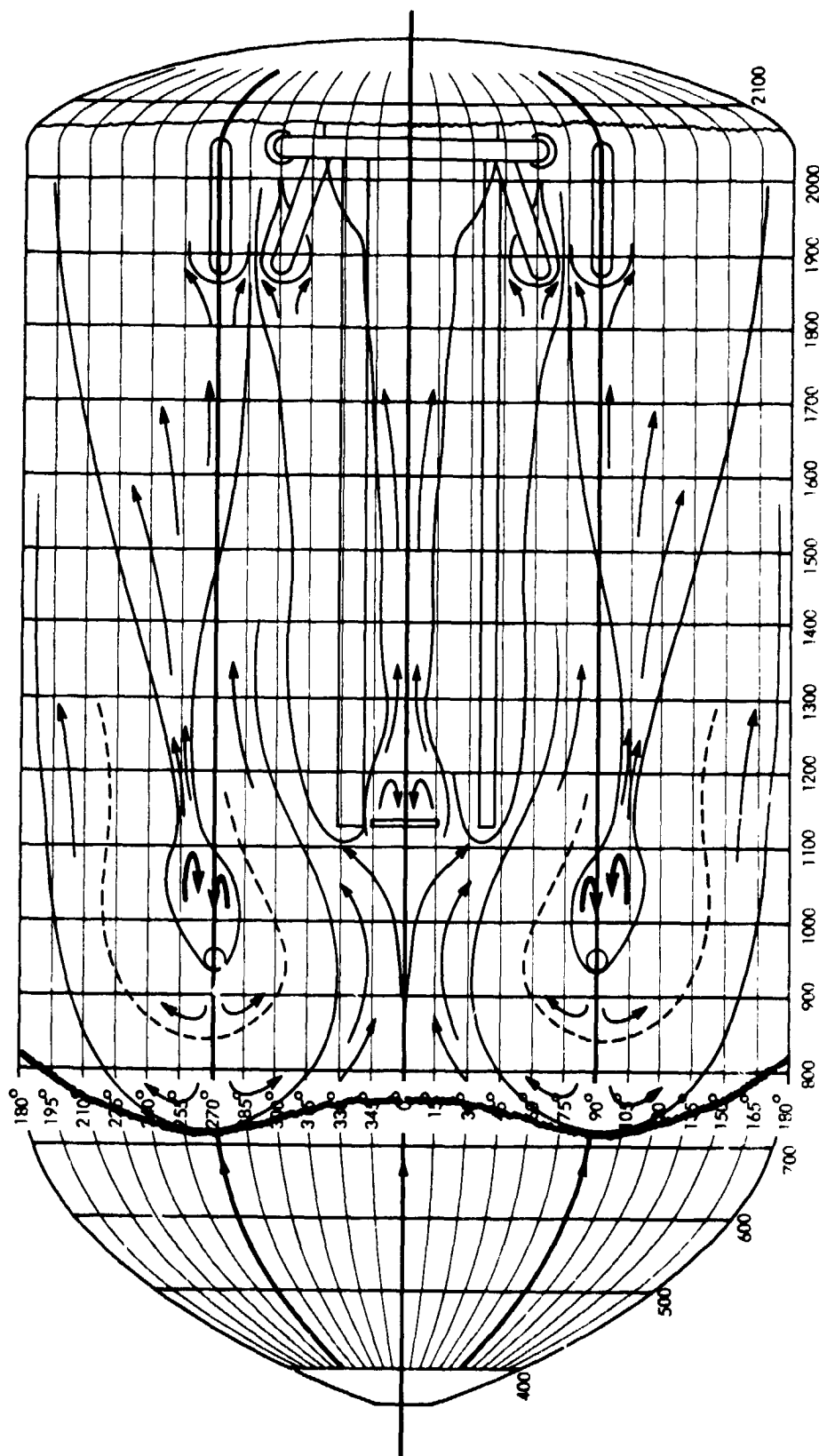
Figure 14. Continued

M_∞ 1.00
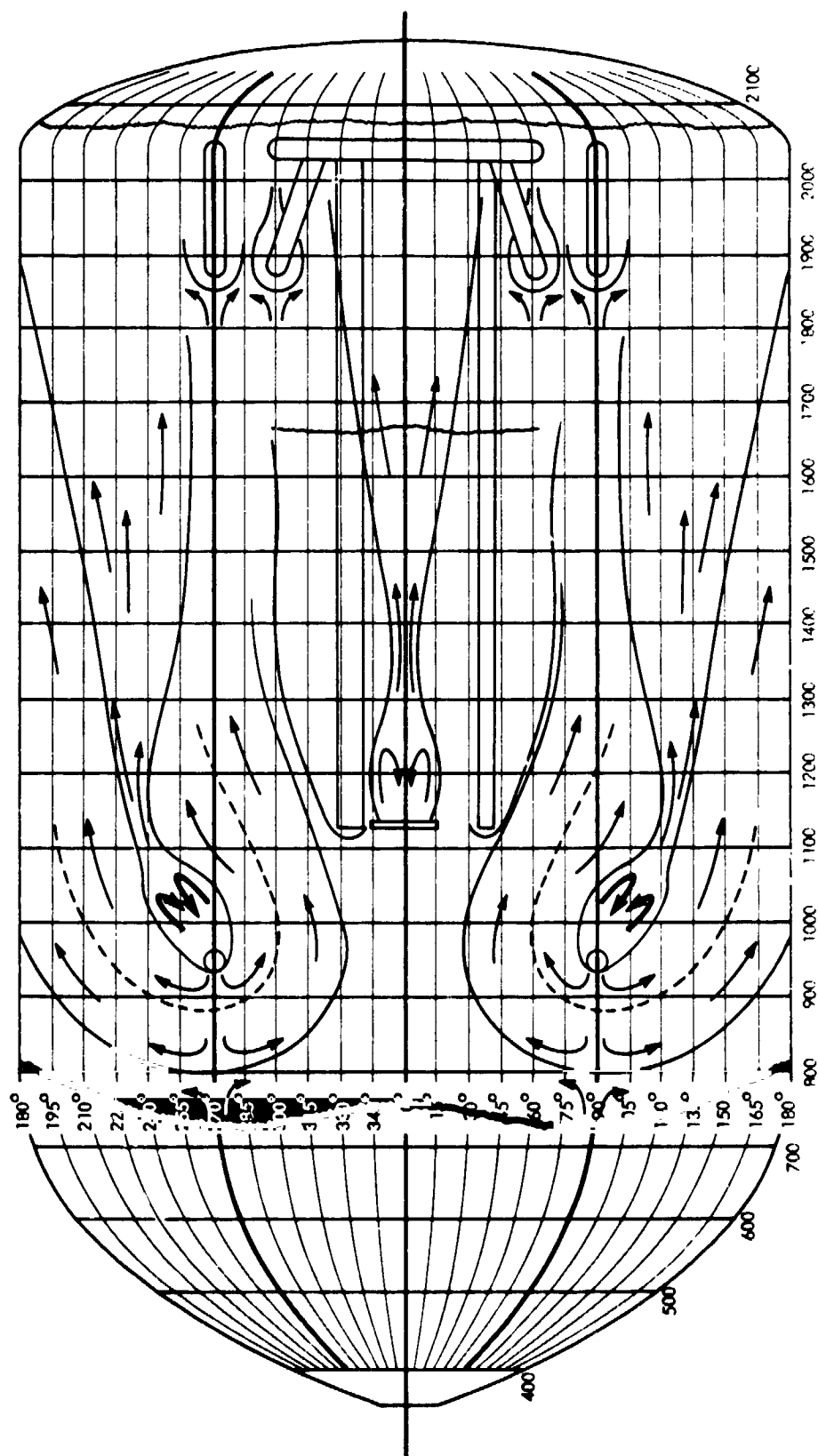
Figure 14. Continued

M_∞ 1.10

Figure 14. Continued

M_∞ 1.20
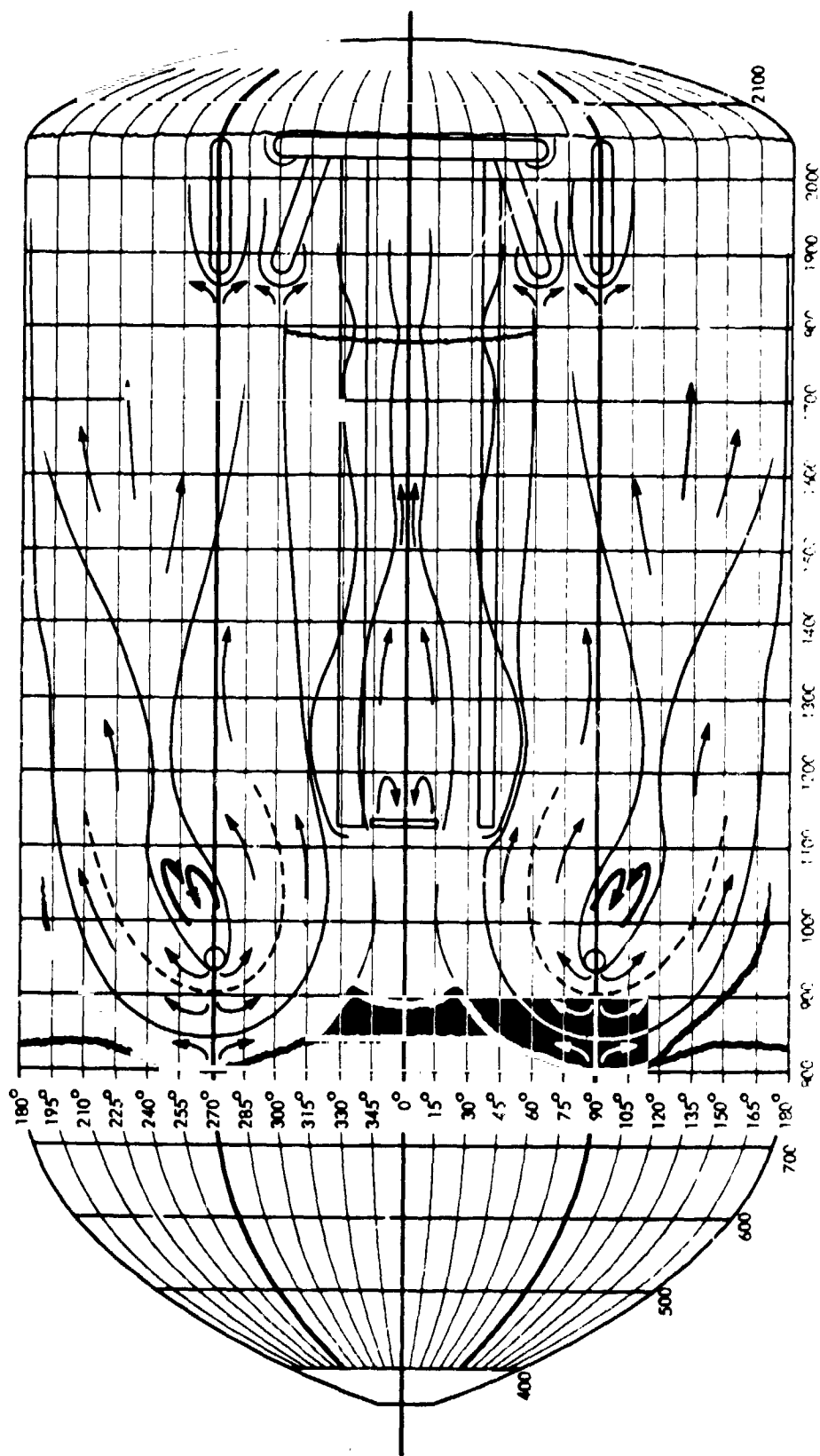
Figure 14. Continued

M_∞ 1.46
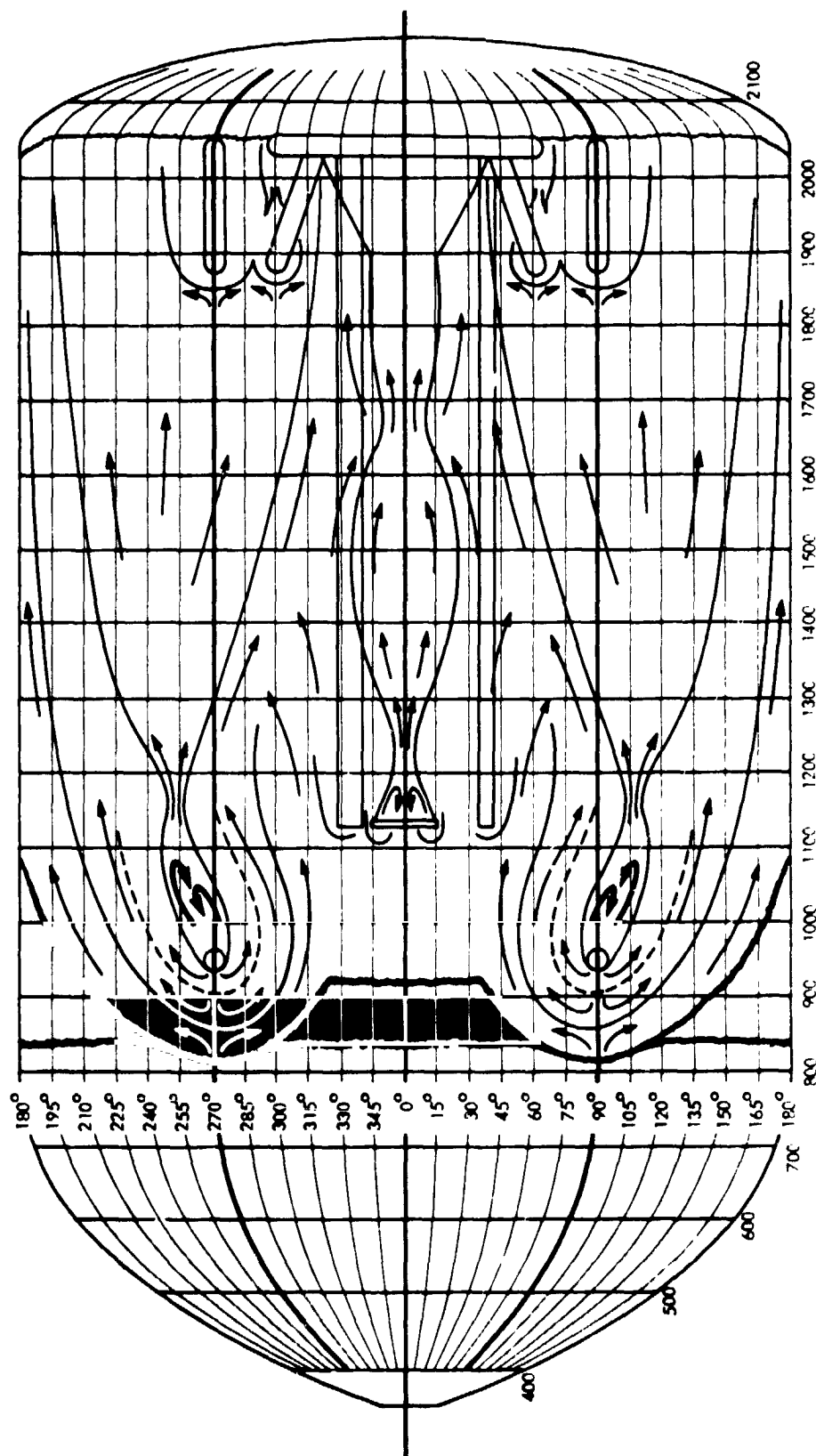
Figure 14. Continued

$M_\infty = 1.96$

59
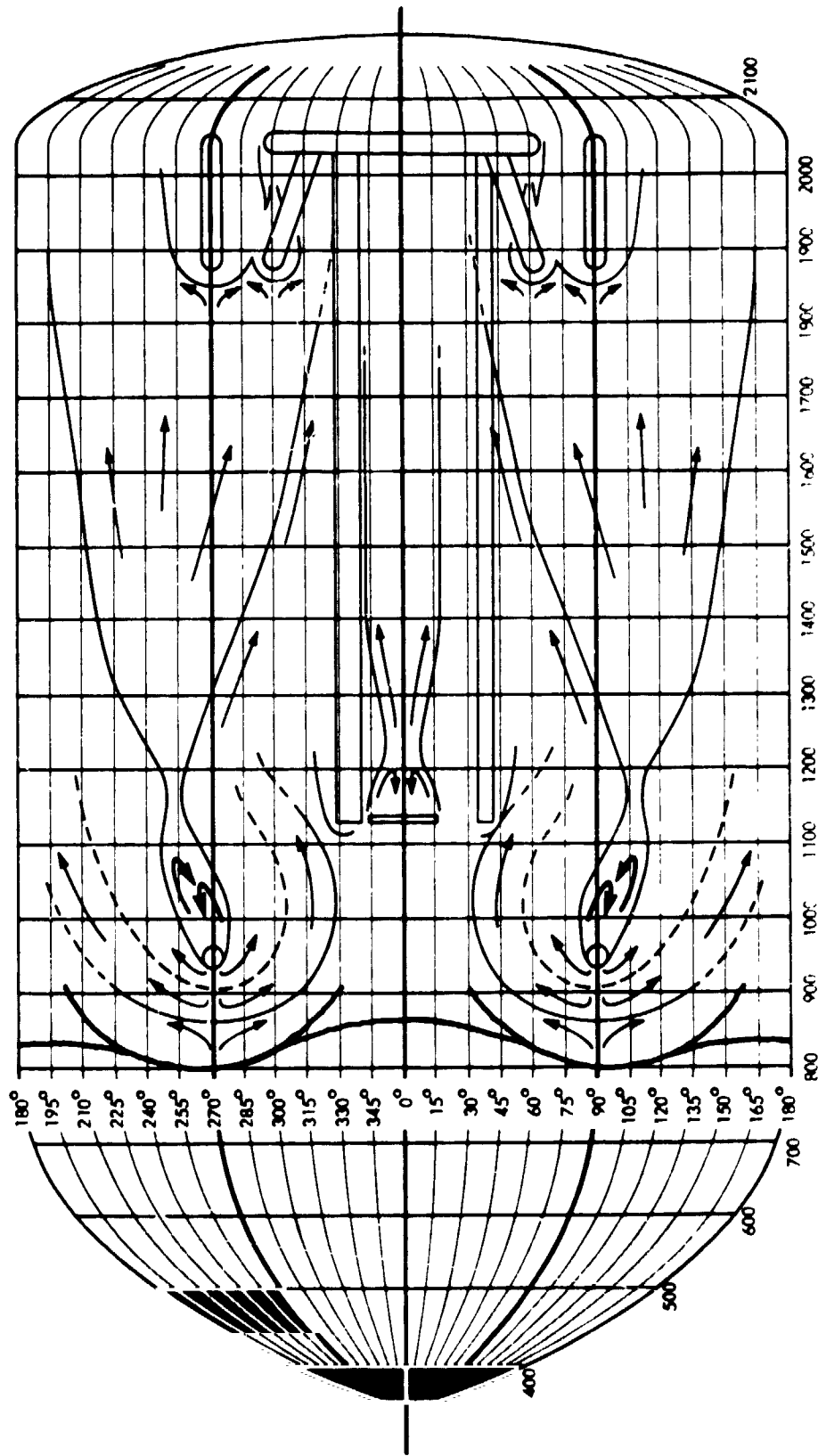
Figure 14. Concluded

M_∞ 3.00
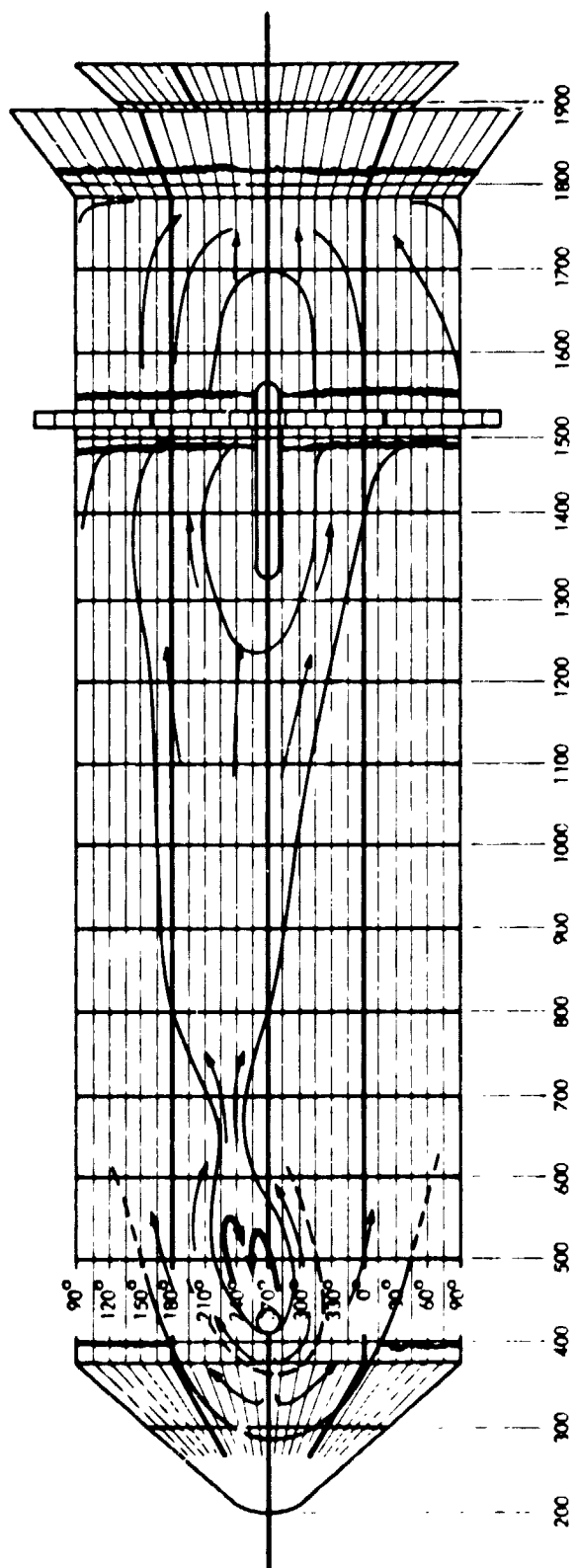
Figure 15. Solid Rocket Booster Flow Diagrams for Space Shuttle Launch Configuration

M_∞ 0.80
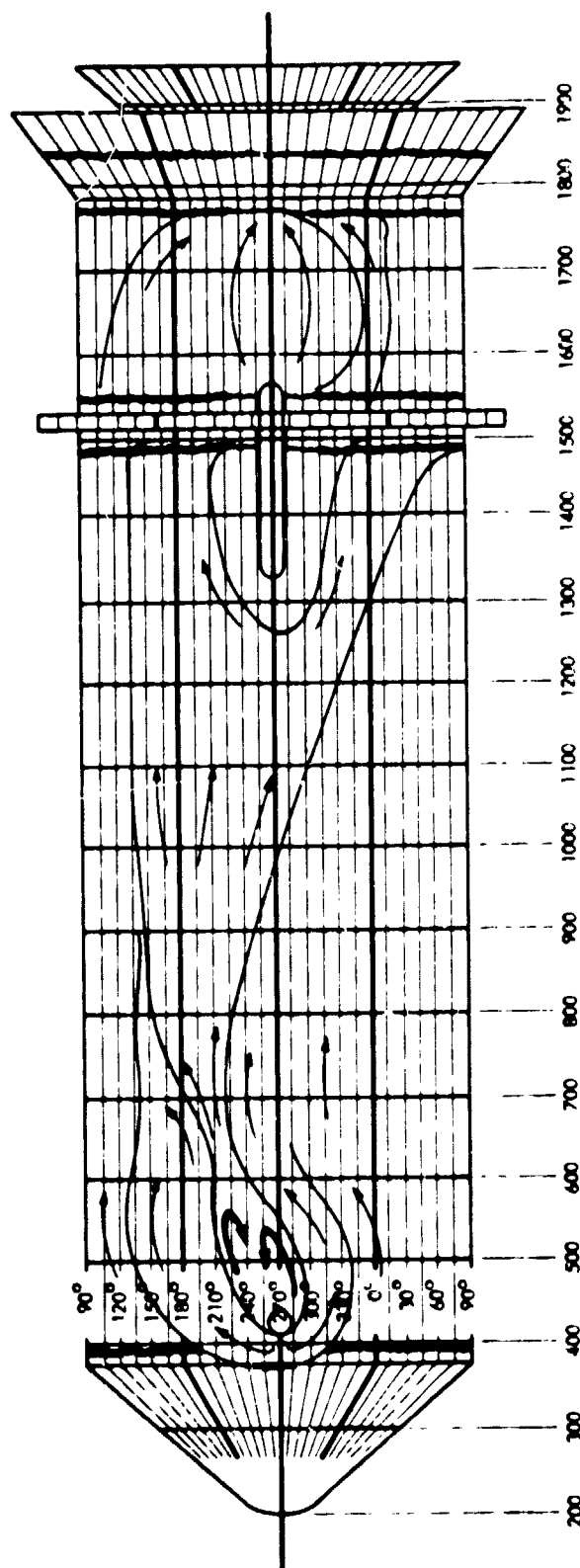
Figure 15. Continued

$M_\infty - 0.90$
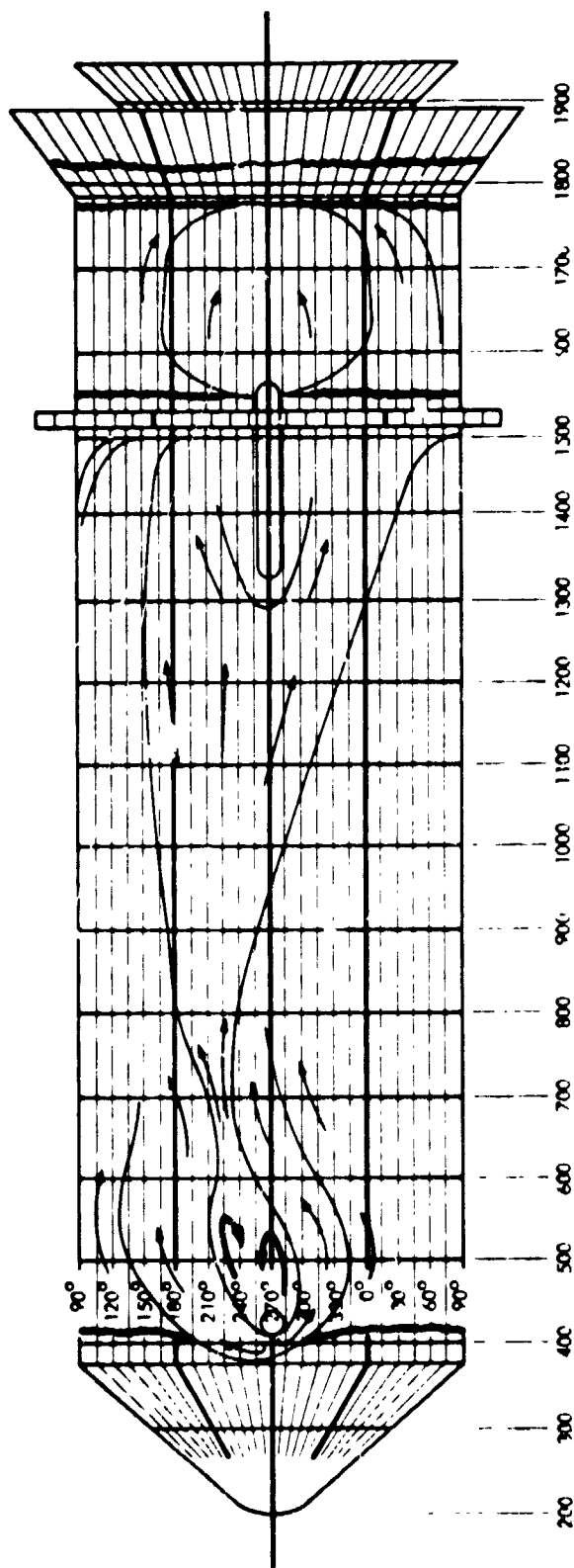
Figure 15. Continued

$M_\infty = 0.05$
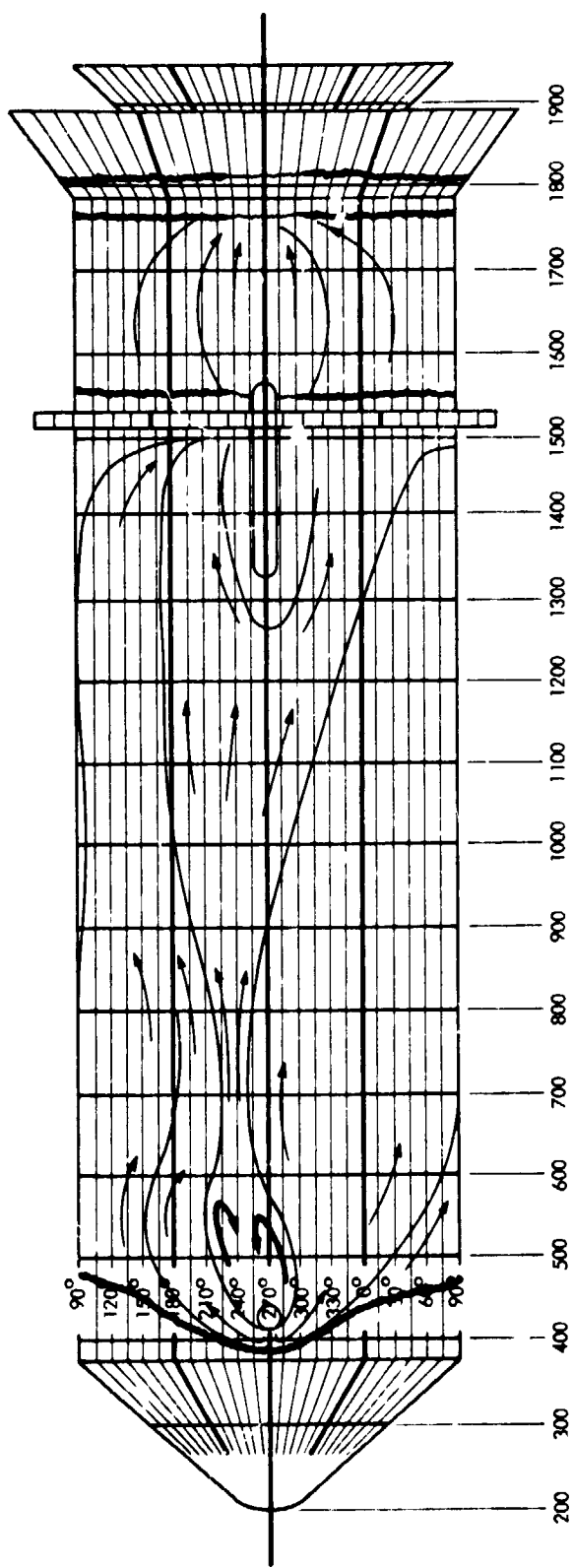
Figure 15, Continued

$M_\infty = 1.00$
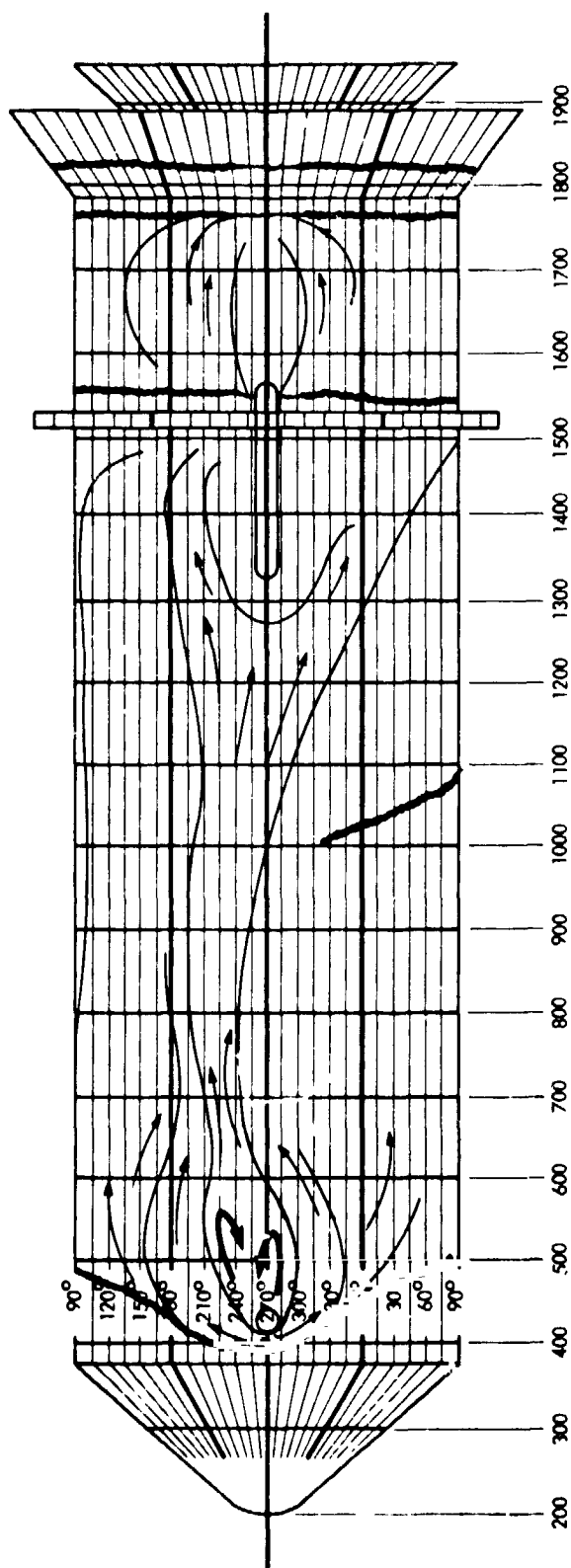
Figure 15. Continued

$M_\infty = 1.10$
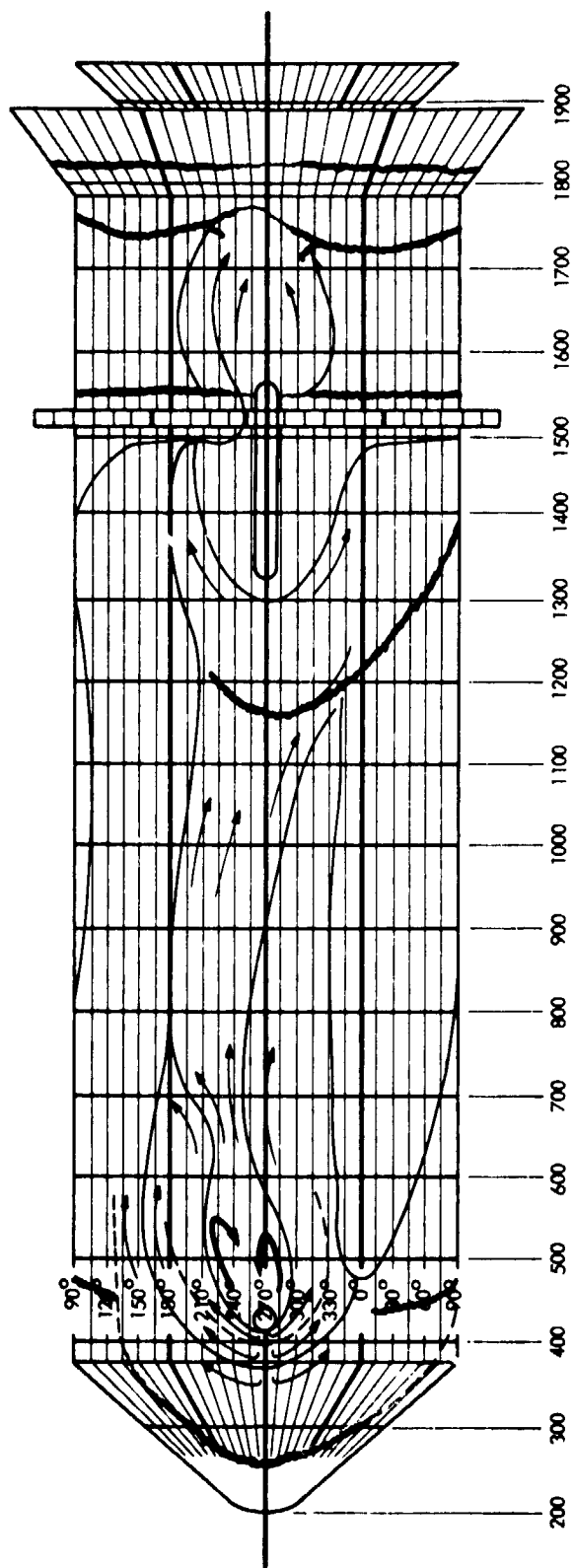
Figure 15. Continued

$M_\infty = 1.20$

66
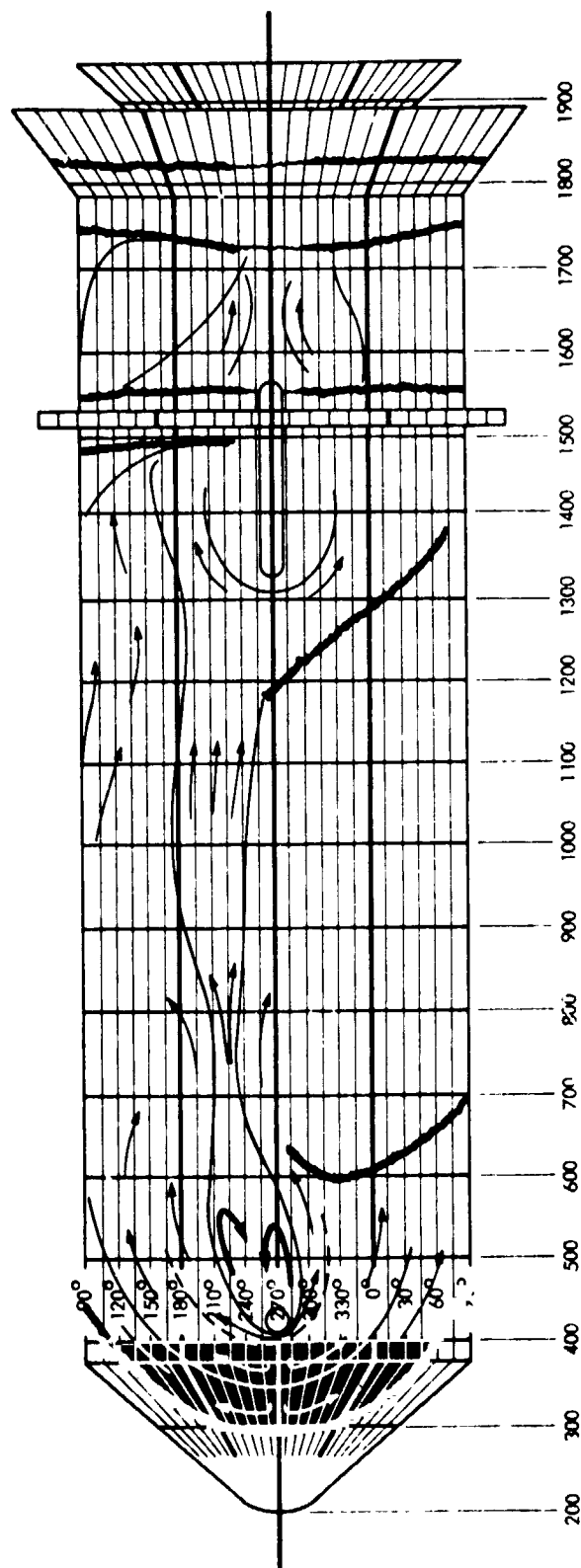
Figure 15. Continued

$M_\infty = 1.46$
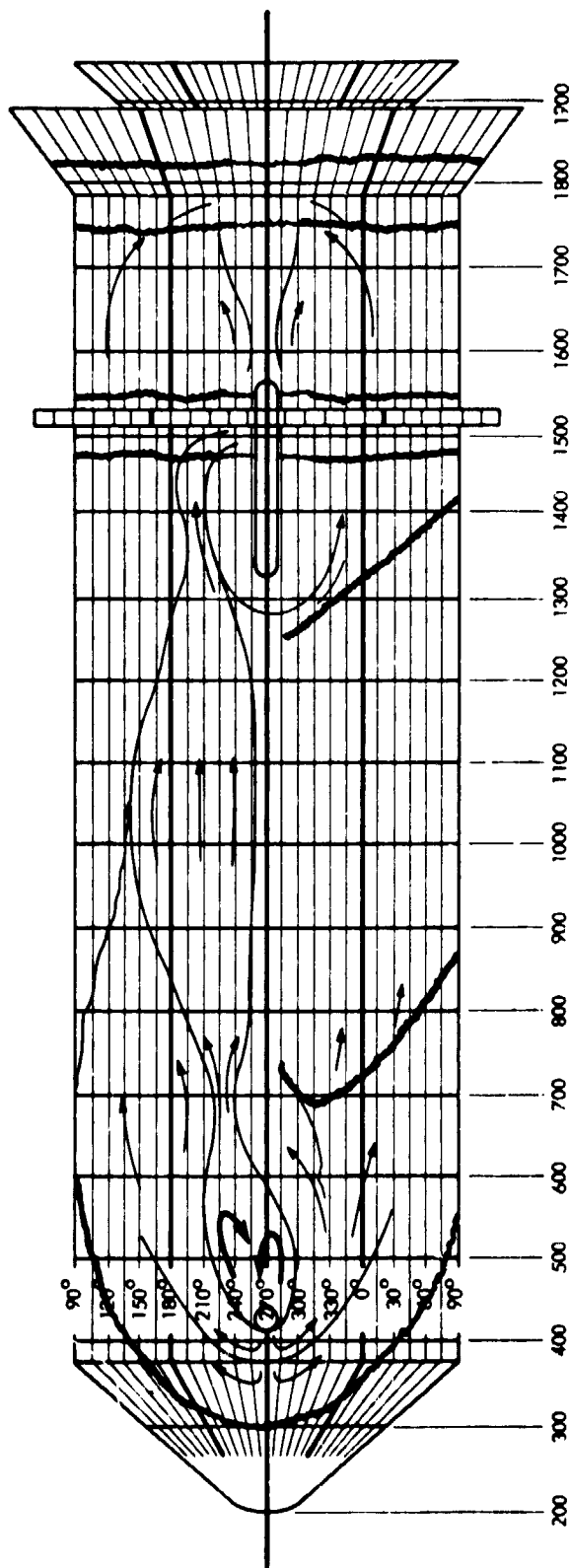
Figure 15. Continued

M_∞ - 1.96
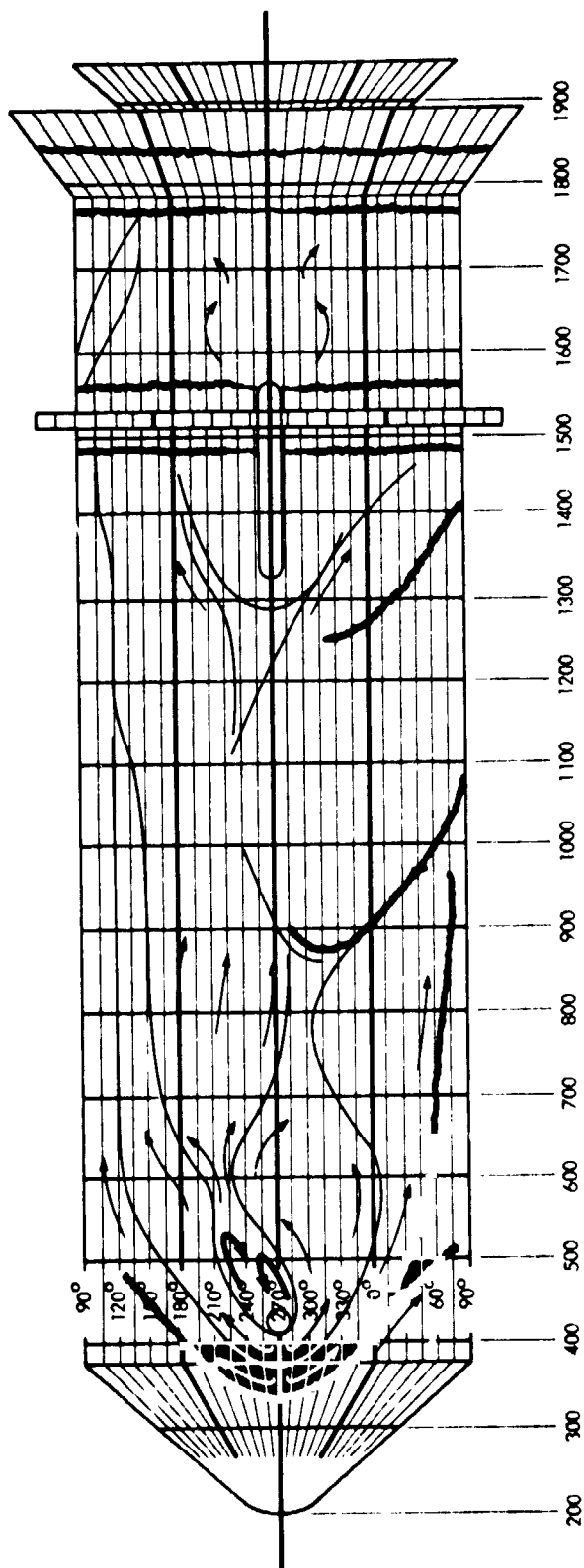
Figure 15. Concluded

$M_\infty = 3.00$

● Reference 18

○ Reference 31

● Variation over Mach number
● Range from 0.60 to M_a

Steven's Prediction
(Reference 32)

Separated Flow
Reattachment
Disturbance

Range for Homogeneous
Separated Flow

ET

SRB

Attached Flow Disturbances

Fluctuating Pressure Coefficient, $\sqrt{\overline{P^2}}/q_\infty$

Cone-Cylinder Angle, $\sim \theta_N$, deg
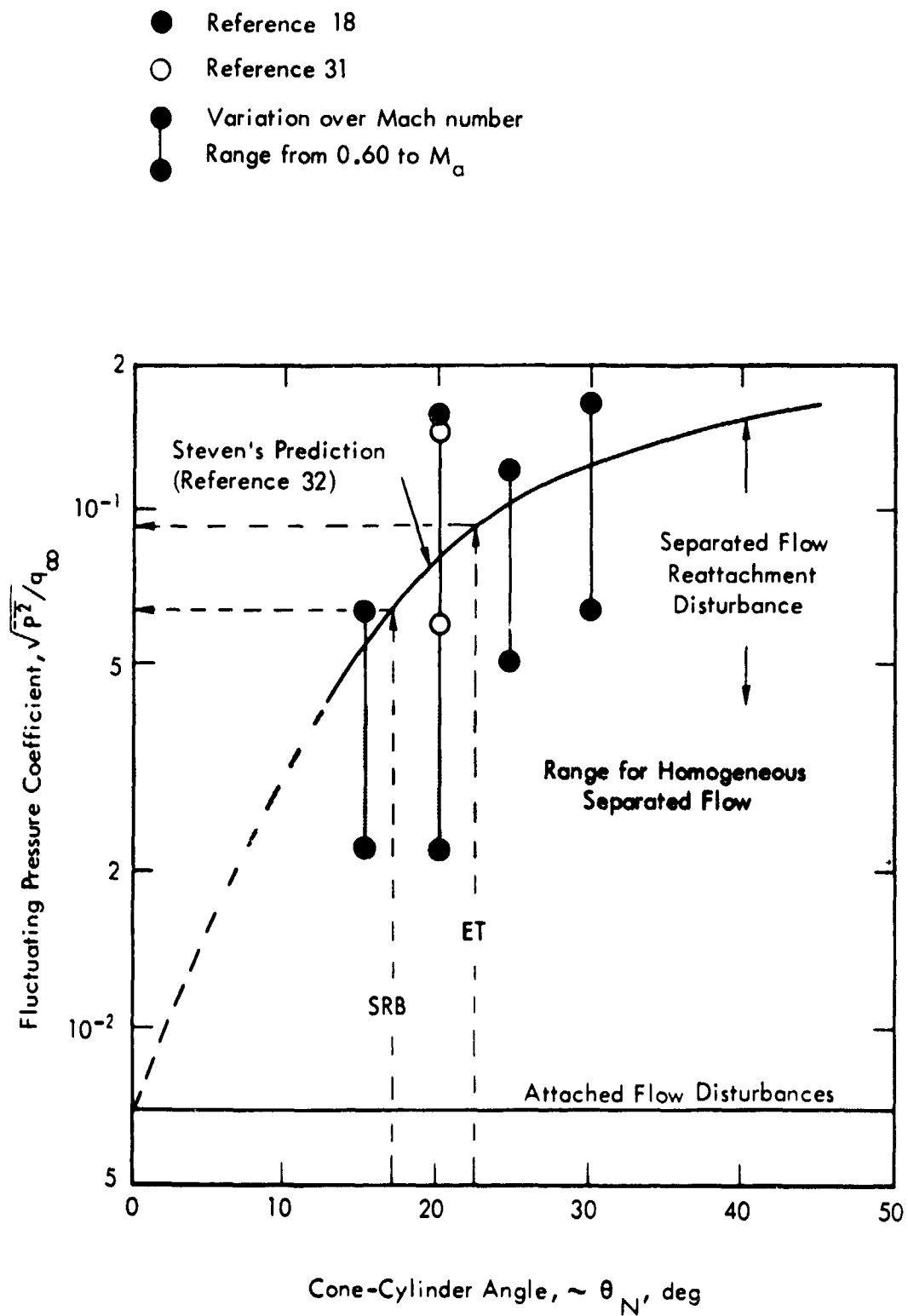
Figure 16. Maximum Fluctuating Pressure Coefficient for Separated Flow Behind a Cone-Cylinder Shoulder for Transonic Flight $(0.6 \leq M_\infty \leq M_a)$

70
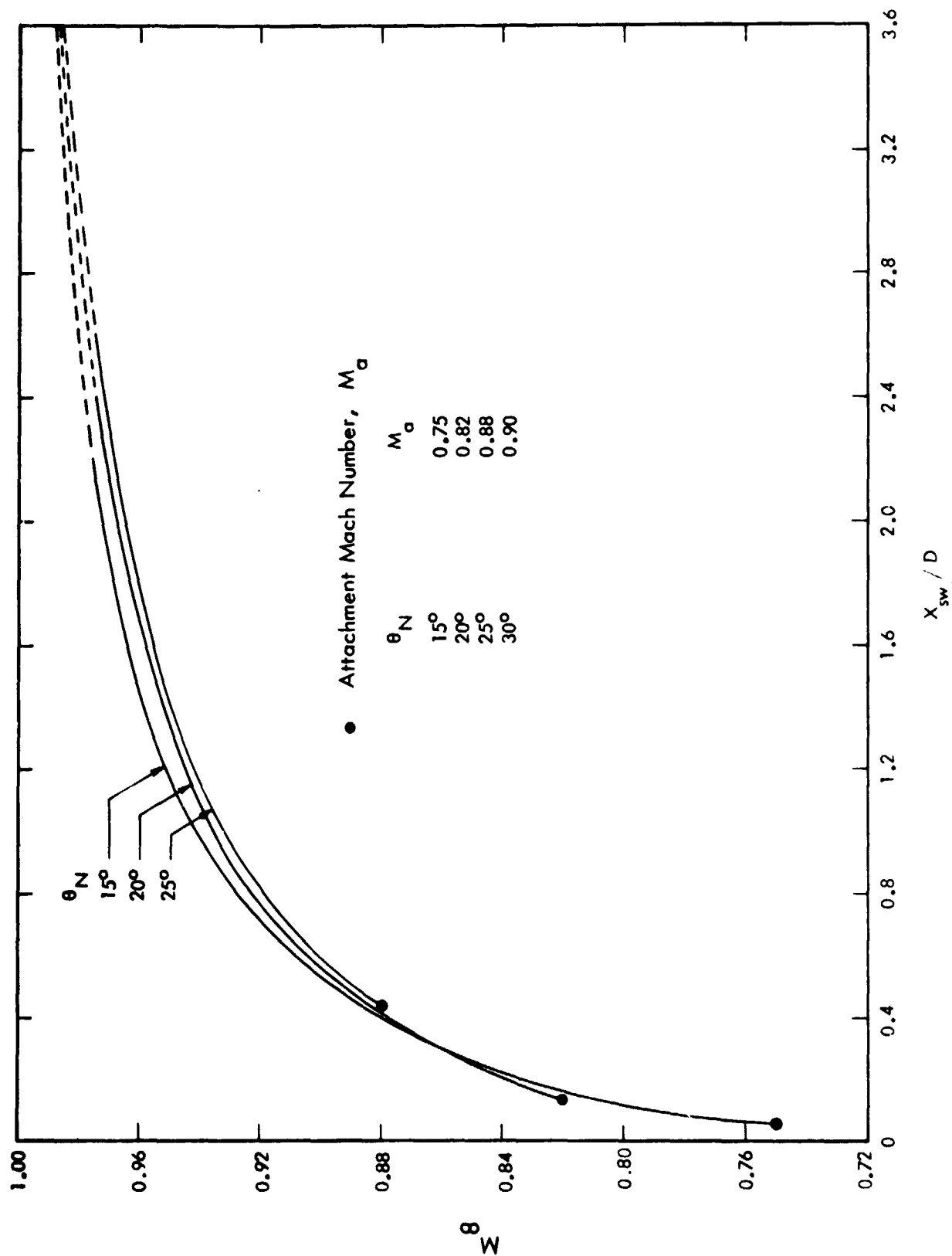
Figure 17. Variation of Terminal Shock-Wave Location with Free-Stream Mach Number for Interference-Free Flow Over Cone-Cylinder Bodies

71
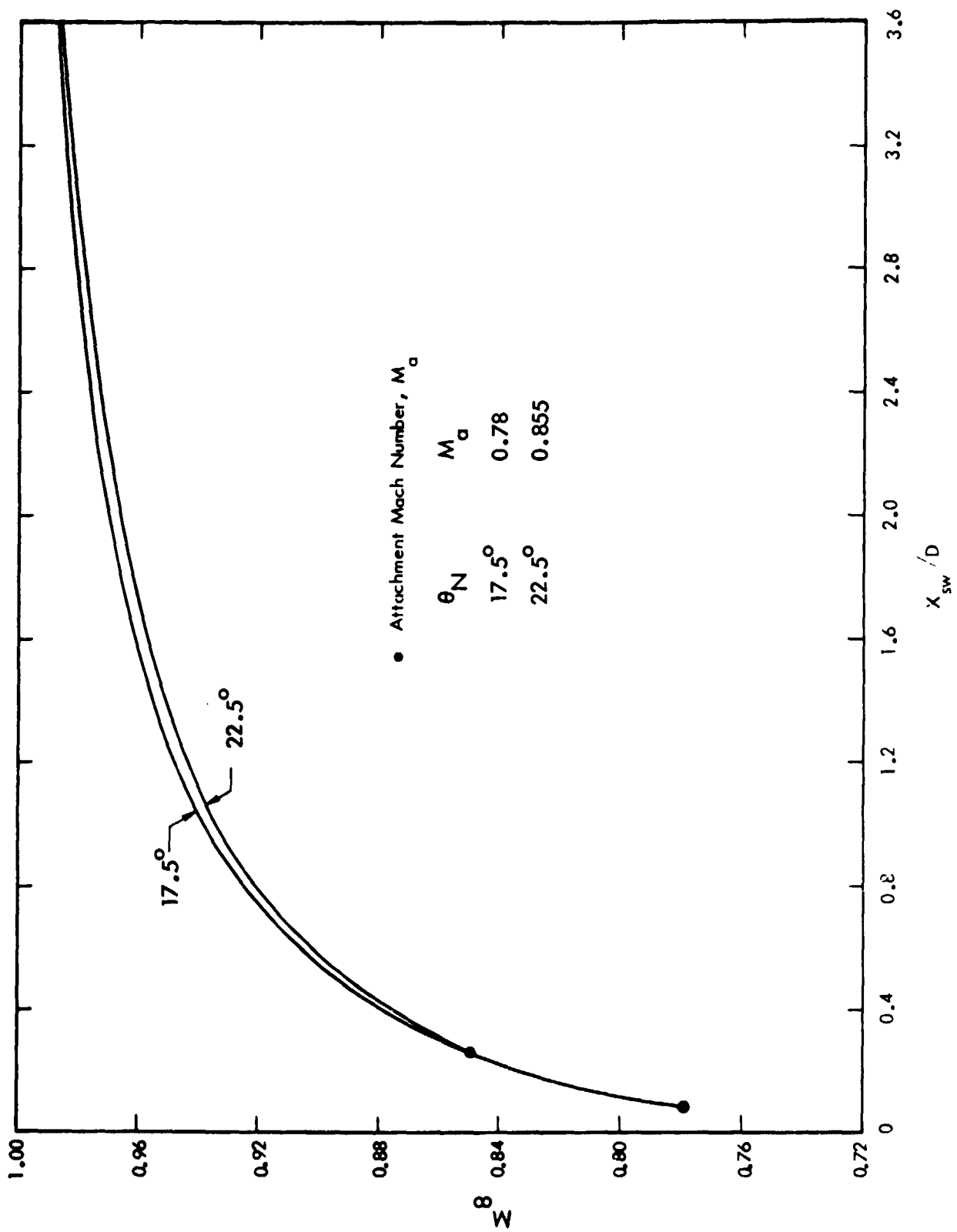
Figure 18. Variation of Terminal Shock-Wave Location, Interpolated for 17.5° and 22.5°
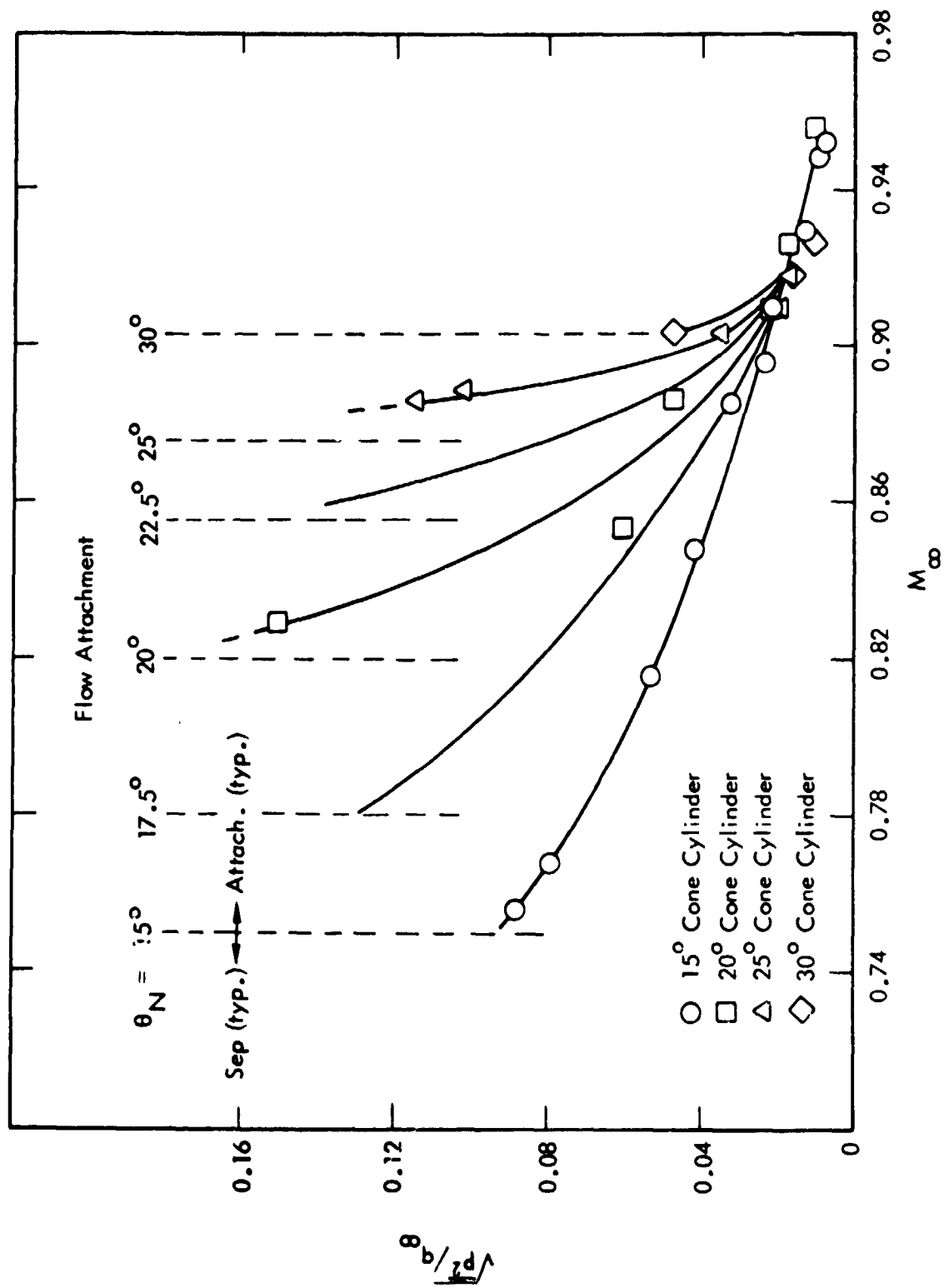
Figure 19. Variation of Transonic Shock-induced Pressure Fluctuations with Free-stream Mach Number for Various Cone-cylinder Configurations (Reference 18)
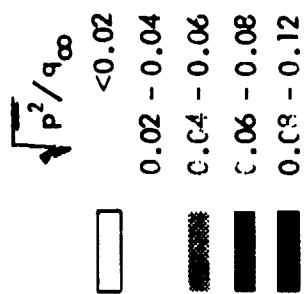
73

$\sqrt{\overline{p^2}}/q_\infty$

	<0.02
	0.02 – 0.04
	0.04 – 0.06
	0.06 – 0.08
	0.08 – 0.12

● Denotes location of wind tunnel data on ET

✖ Denotes ET location to which wind tunnel data from the adjacent orbiter surface was applied
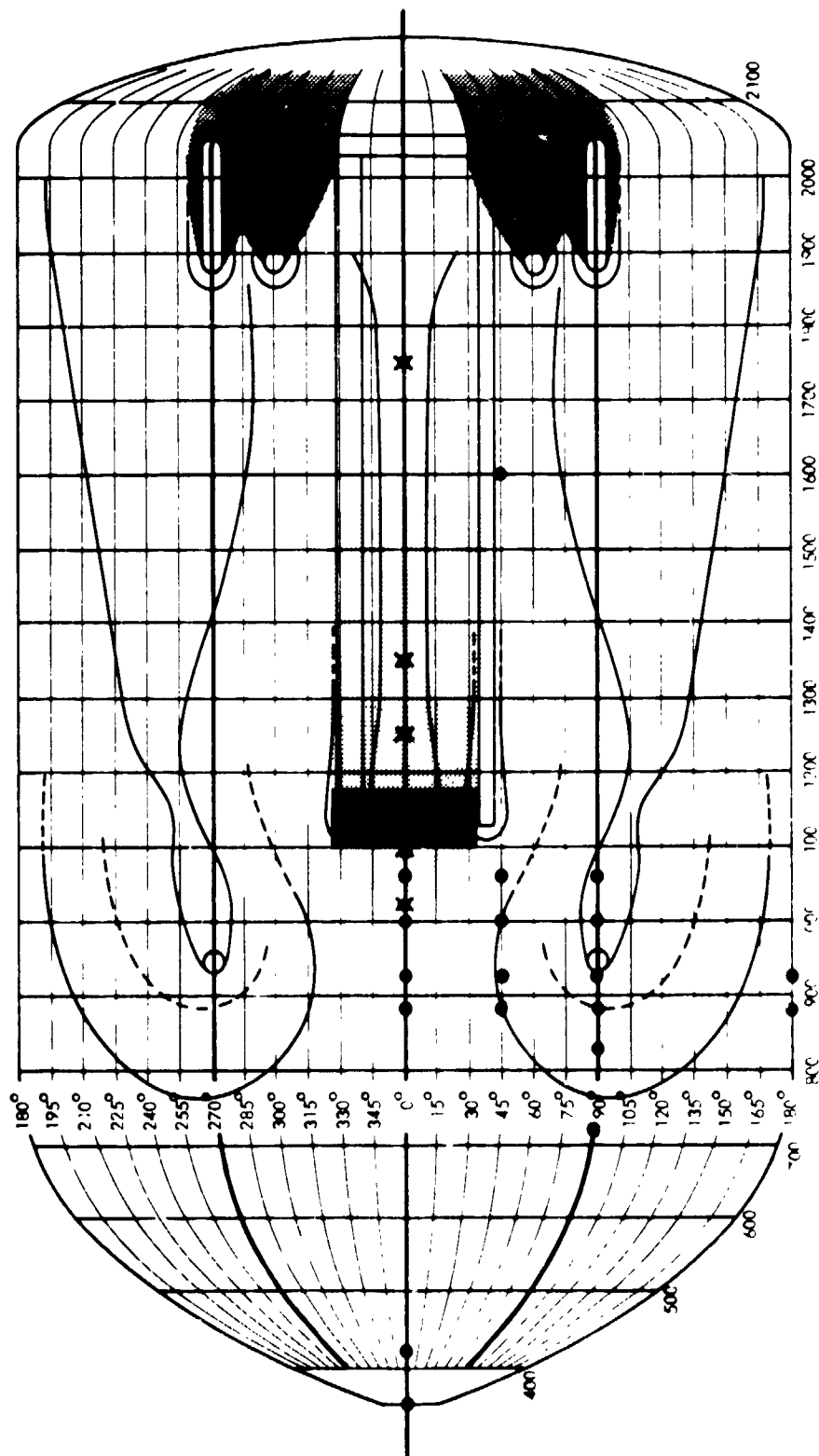
Figure 20. External Tank Fluctuating Pressure Environments
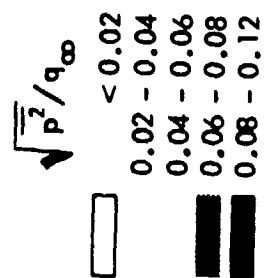
$M_\infty = 0.80$

Figure 20. Continued

$M_\infty = 0.90$

- ● Denotes location of wind tunnel data on ET
- ★ Denotes ET location to which wind tunnel data from the adjacent orbiter surface was applied

$\sqrt{\overline{p^2}}/q_\infty$

< 0.02
0.02 - 0.04
0.04 - 0.06
0.06 - 0.08
0.08 - 0.12

75

Figure 20. Continued

M_∞ 0.95

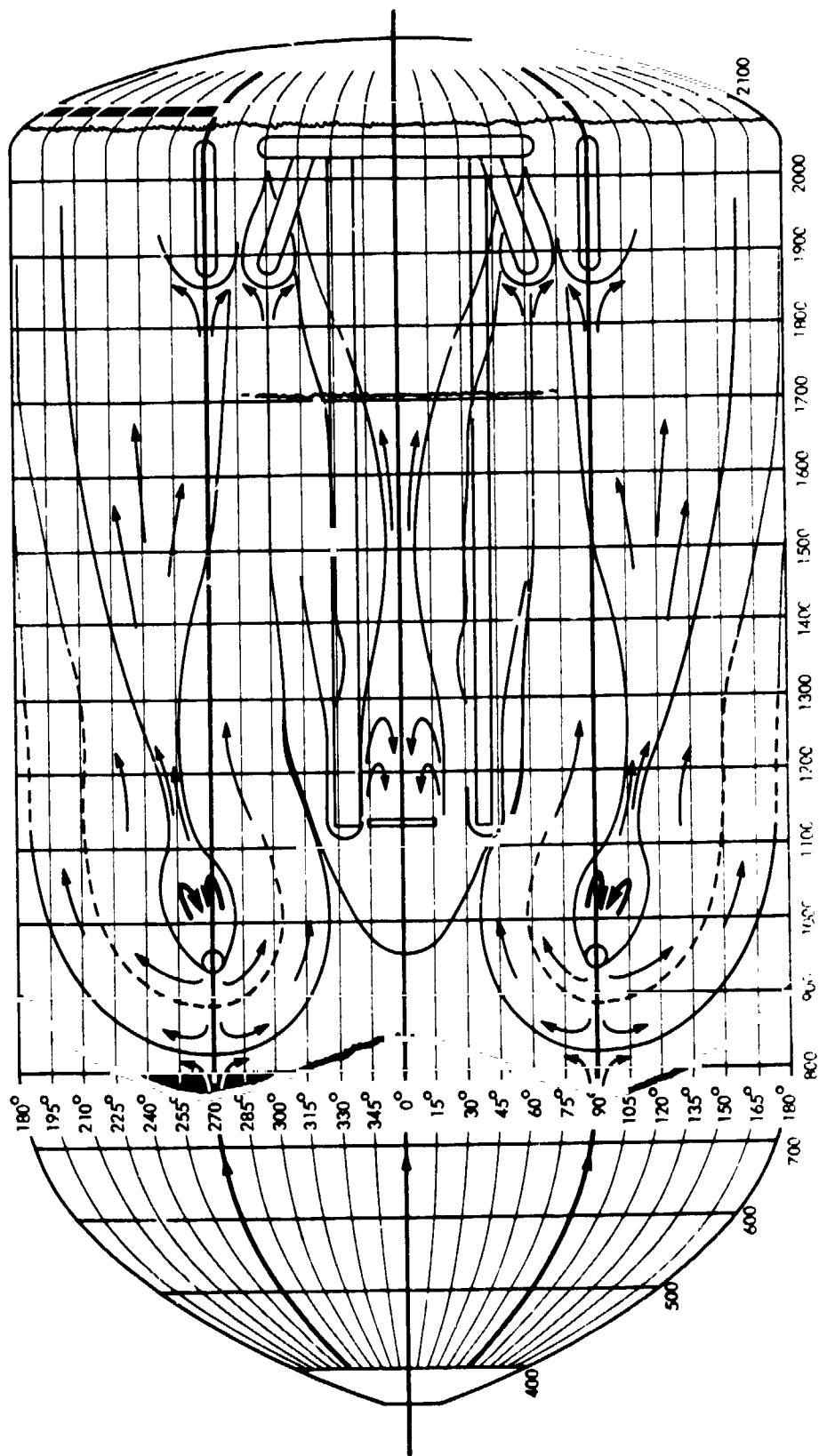Figure 20. Continued

$M_\infty = 1.00$

77

Figure 20. Continued

$M_\infty = 1.10$

78

Figure 20. Continued

$M_\infty = 1.20$

$\sqrt{\overline{p^2}/q_\infty}$

	< 0.02
	0.02 – 0.04
	0.04 – 0.06
	0.06 – 0.08
	0.08 – 0.12

● Denotes location of wind tunnel data on ET

✱ Denotes ET location to which wind tunnel data from the adjacent orbiter surface was applied

Figure 20. Continued
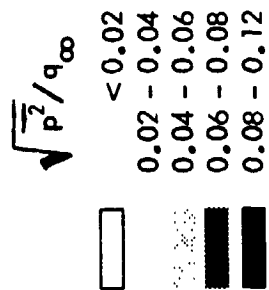
$M_\infty = 1.45$

Figure 20. Continued

$M_\infty = 1.96$

81

Figure 20. Concluded

$M_\infty = 3.00$
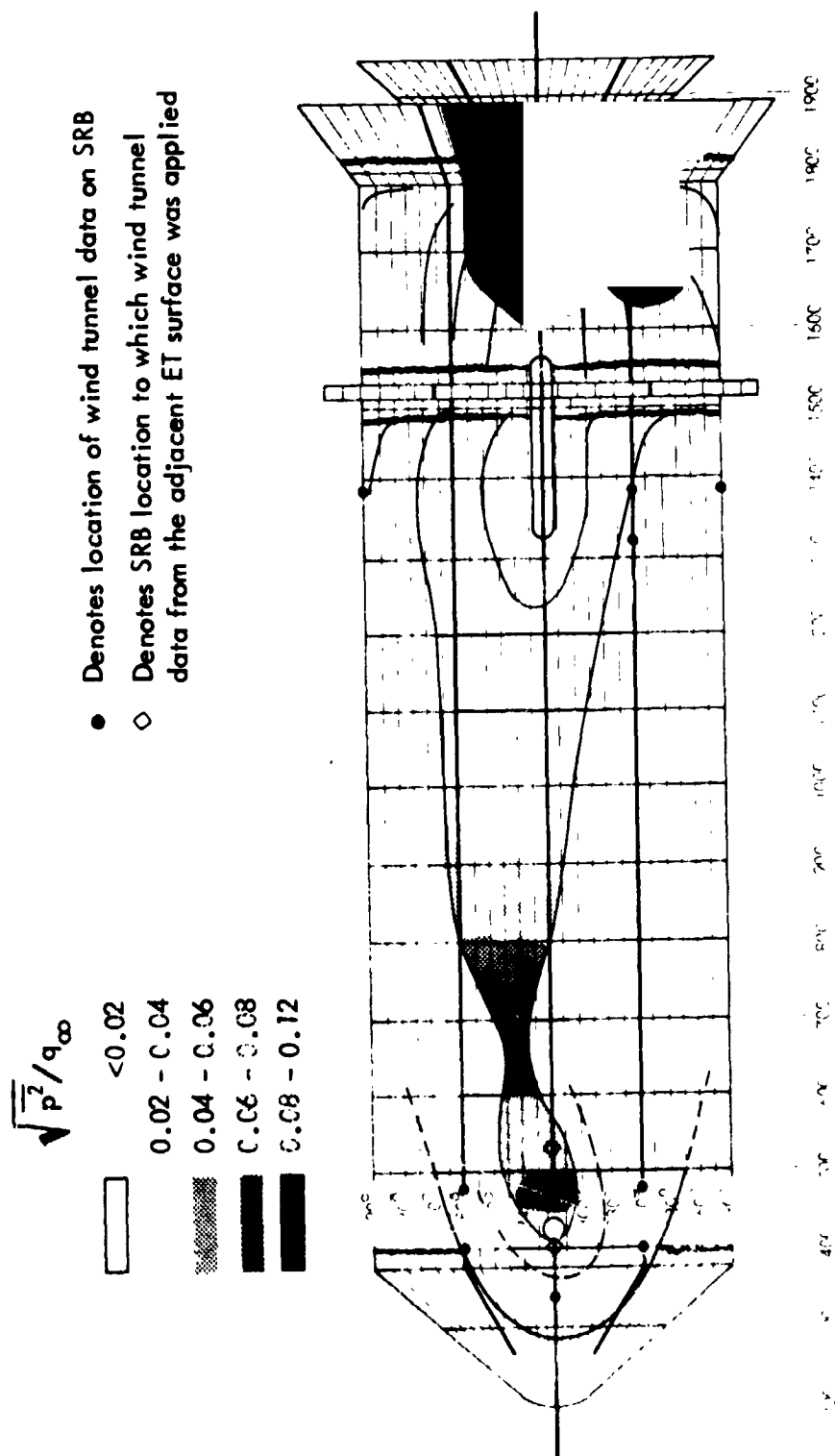
Figure 21. Solid Rocket Booster Fluctuating Pressure Environments

$$M_\infty = 0.80$$

• Denotes location of wind tunnel data on SRB

◊ Denotes SRB location to which wind tunnel data from the adjacent ET surface was applied

$\sqrt{\overline{p^2}}/q_\infty$

□	<0.02
	0.02 - 0.04
▓	0.04 - 0.06
■	0.06 - 0.08
∥	0.08 - 0.12

83

- Denotes location of wind tunnel data on SRB
- ◇ Denotes SRB location to which wind tunnel data from the adjacent ET surface was applied

$$\sqrt{\overline{p^2}}/q_\infty$$

	< 0.02
	0.02 – 0.04
	0.04 – 0.06
	0.06 – 0.08
	0.08 – 0.12
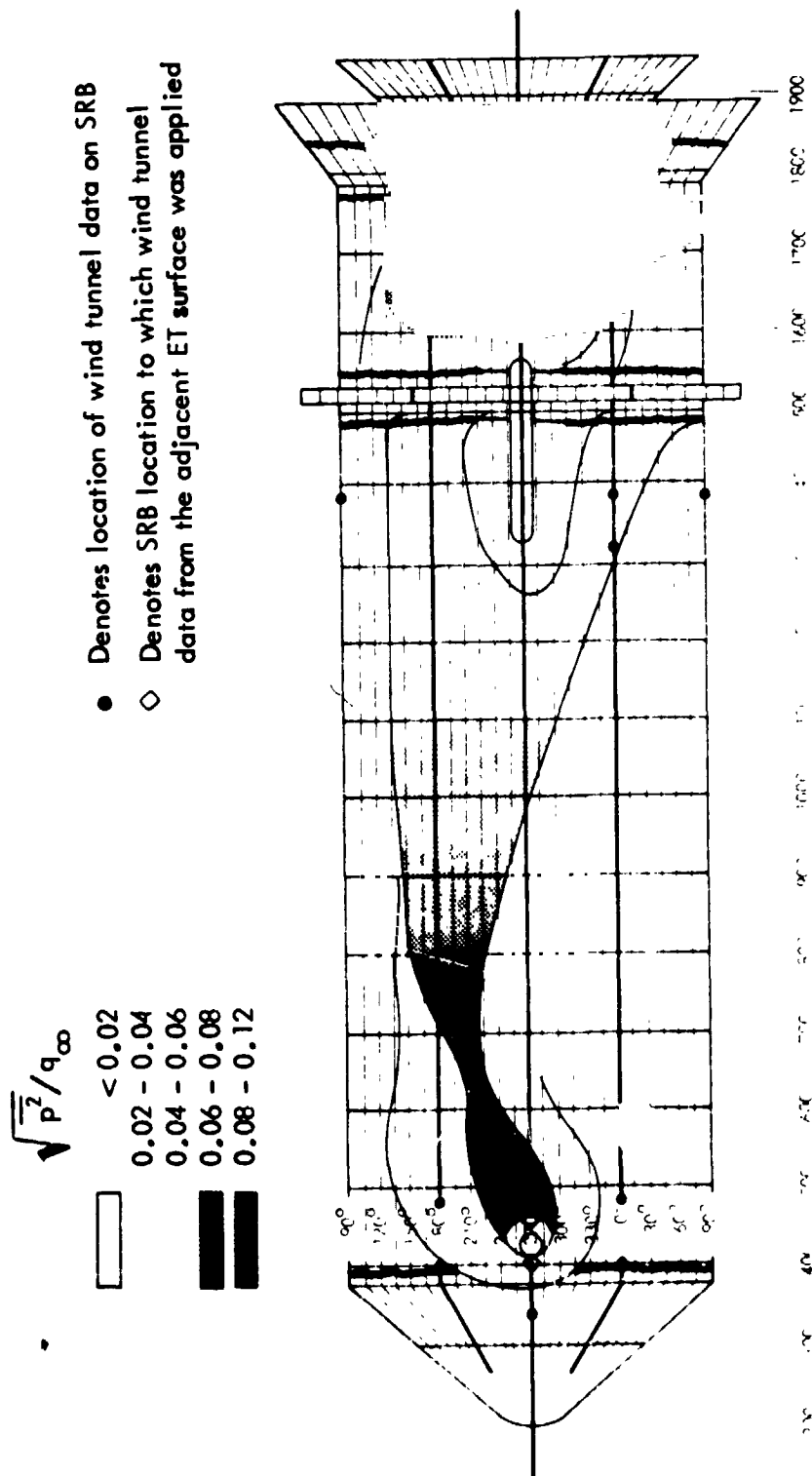
Figure 21. Continued

$M_\infty = 0.90$

Figure 21. Continued

$M_\infty = 0.95$

Legend:

$\sqrt{\overline{p^2}}/q_\infty$

	< 0.02
	0.02 – 0.04
	0.04 – 0.06
	0.06 – 0.08
	0.08 – 0.12

● Denotes location of wind tunnel data on SRB

◇ Denotes SRB location to which wind tunnel data from the adjacent ET surface was applied

Figure 21. Continued

$M_\infty = 1.00$

Legend:

● Denotes location of wind tunnel data on SRB

◇ Denotes SRB location to which wind tunnel data from the adjacent ET surface was applied

$\sqrt{\overline{p^2}}/q_\infty$

< 0.02

0.02 – 0.04

0.04 – 0.06

0.06 – 0.08

0.08 – 0.12
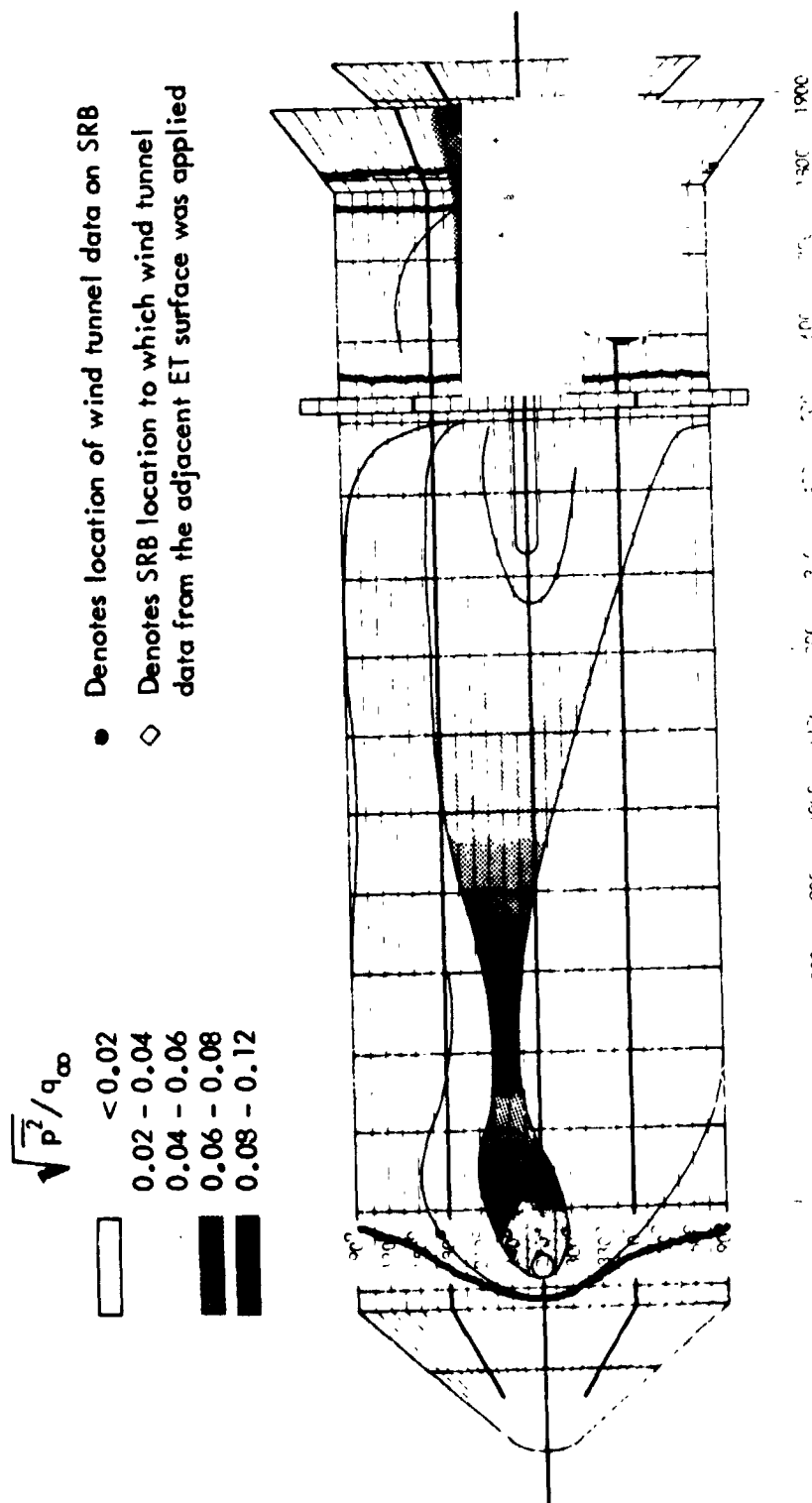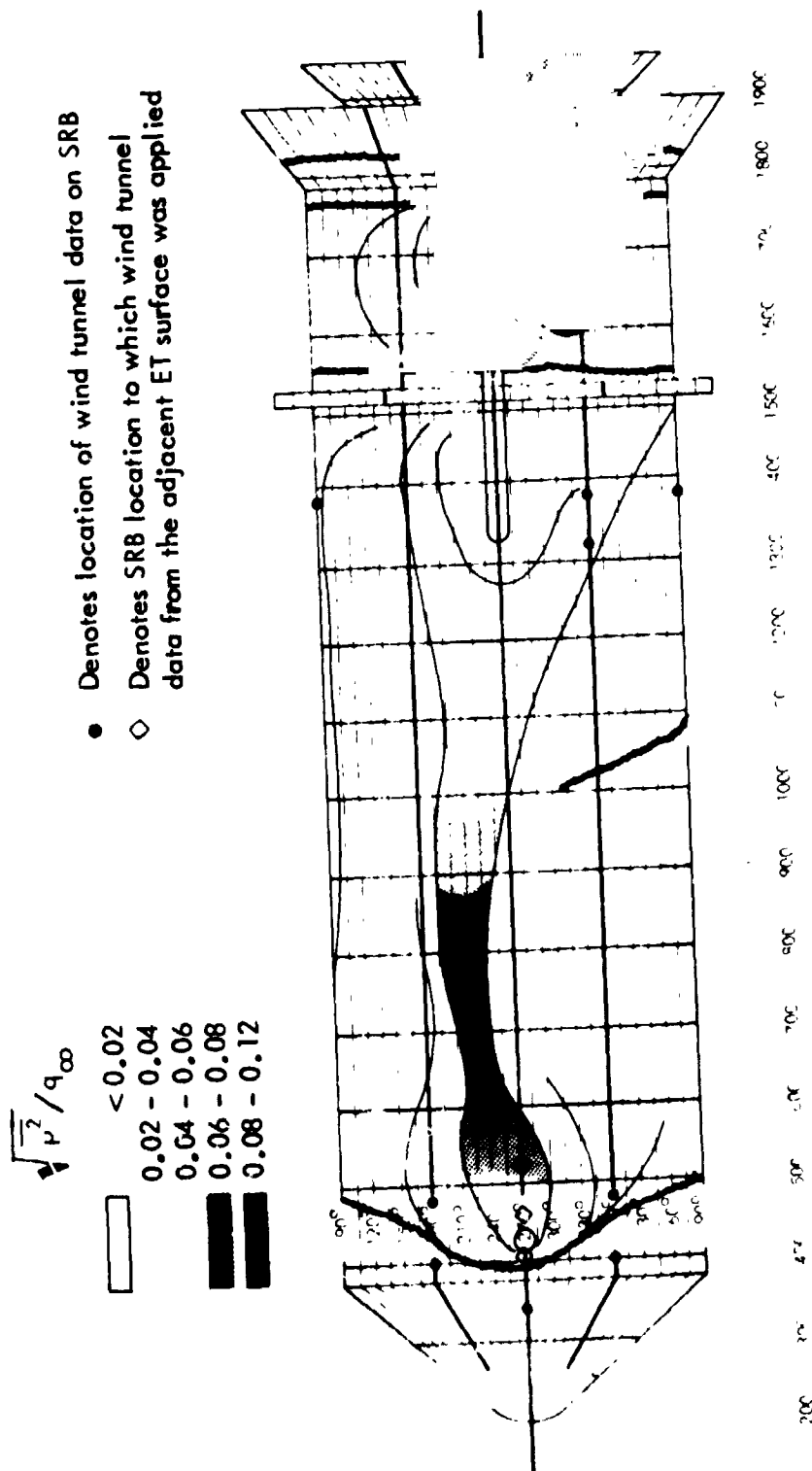
Figure 21. Continued

$M_\infty = 1.10$

Denotes location of wind tunnel data on SRB

Denotes SRB location to which wind tunnel data from the adjacent ET surface was applied

$$\sqrt{\overline{p^2}}/q_\infty$$

< 0.02
0.02 – 0.04
0.04 – 0.06
0.06 – 0.08
0.08 – 0.12

$\sqrt{\overline{p^2}}/q_\infty$

    < 0.02

    0.02 – 0.04

    0.04 – 0.06

    0.06 – 0.08

    0.08 – 0.12

● Denotes location of wind tunnel data on SRB

◇ Denotes SRB location to which wind tunnel data from the adjacent ET surface was applied
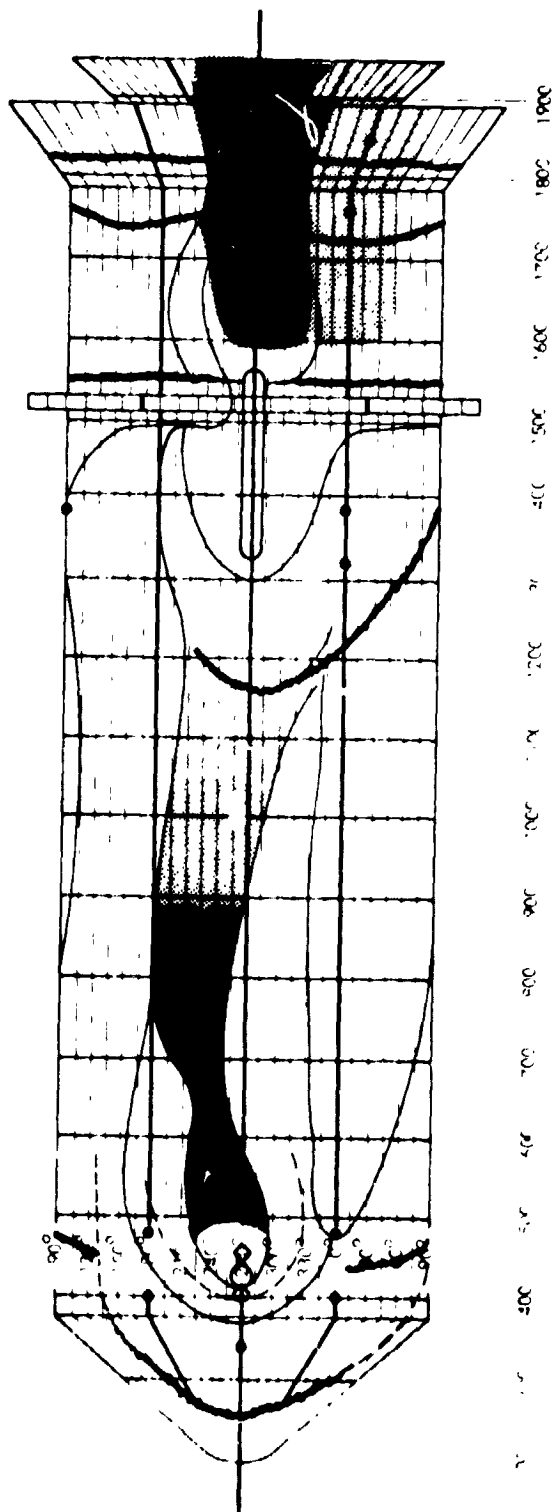
Figure 2i. Continued

$M_\infty = 1.20$

• Denotes location of wind tunnel data on SRB

◡ Denotes SRB location to which wind tunnel data from the adjacent ET surface was applied

$$\sqrt{\overline{p^2}/q_\infty}$$

< 0.02
0.02 - 0.04
0.04 - 0.06
0.06 - 0.08
0.08 - 0.12

Figure 21. Continued
$M_\infty = 1.46$
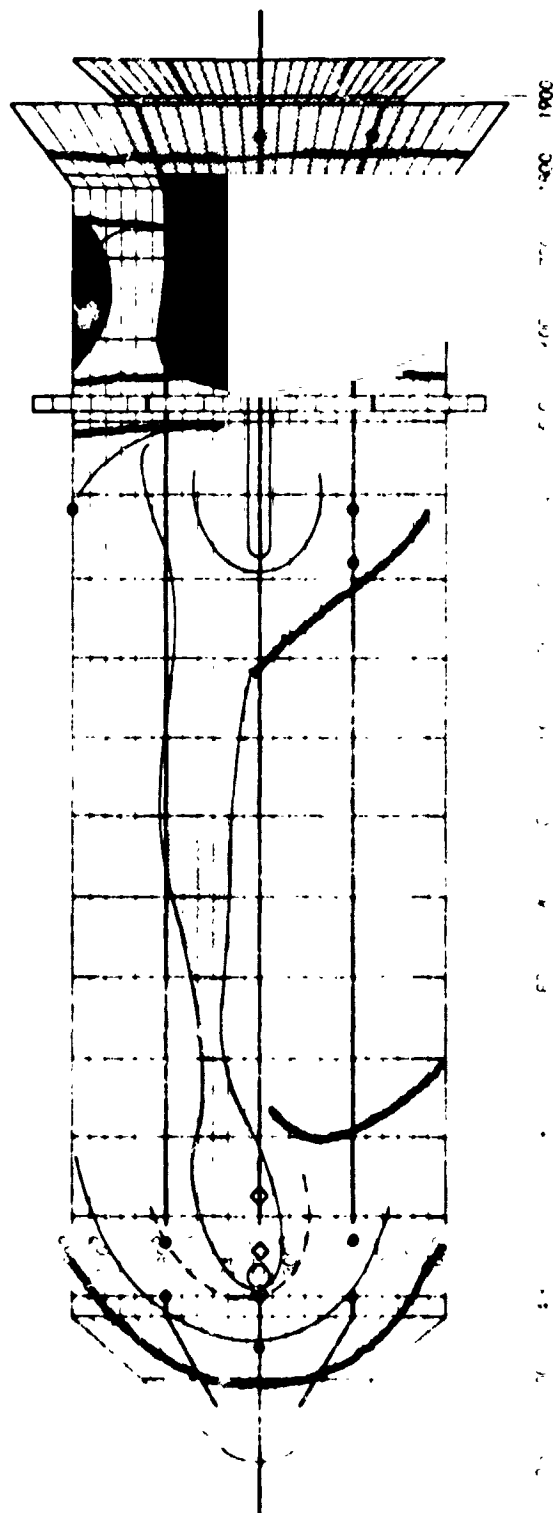
Figure 21. Continued

$M_\infty = 1.96$

Denotes location of wind tunnel data on SRB

Denotes SRB location to which wind tunnel data from the adjacent ET surface was applied

$\sqrt{\overline{p^2}}/q_\infty$

< 0.02
0.02 – 0.04
0.04 – 0.06
0.06 – 0.08
0.08 – 0.12

Figure 21. Concluded.
$M_\infty = 3.00$

Legend (on figure):
- Denotes location of wind tunnel data on SRB
- Denotes SRB location to which wind tunnel data from the adjacent ET surface was applied

$\sqrt{\overline{p^2}}/q_\infty$

< 0.02
0.02 - 0.04
0.04 - 0.06
0.06 - 0.08
0.08 - 0.12

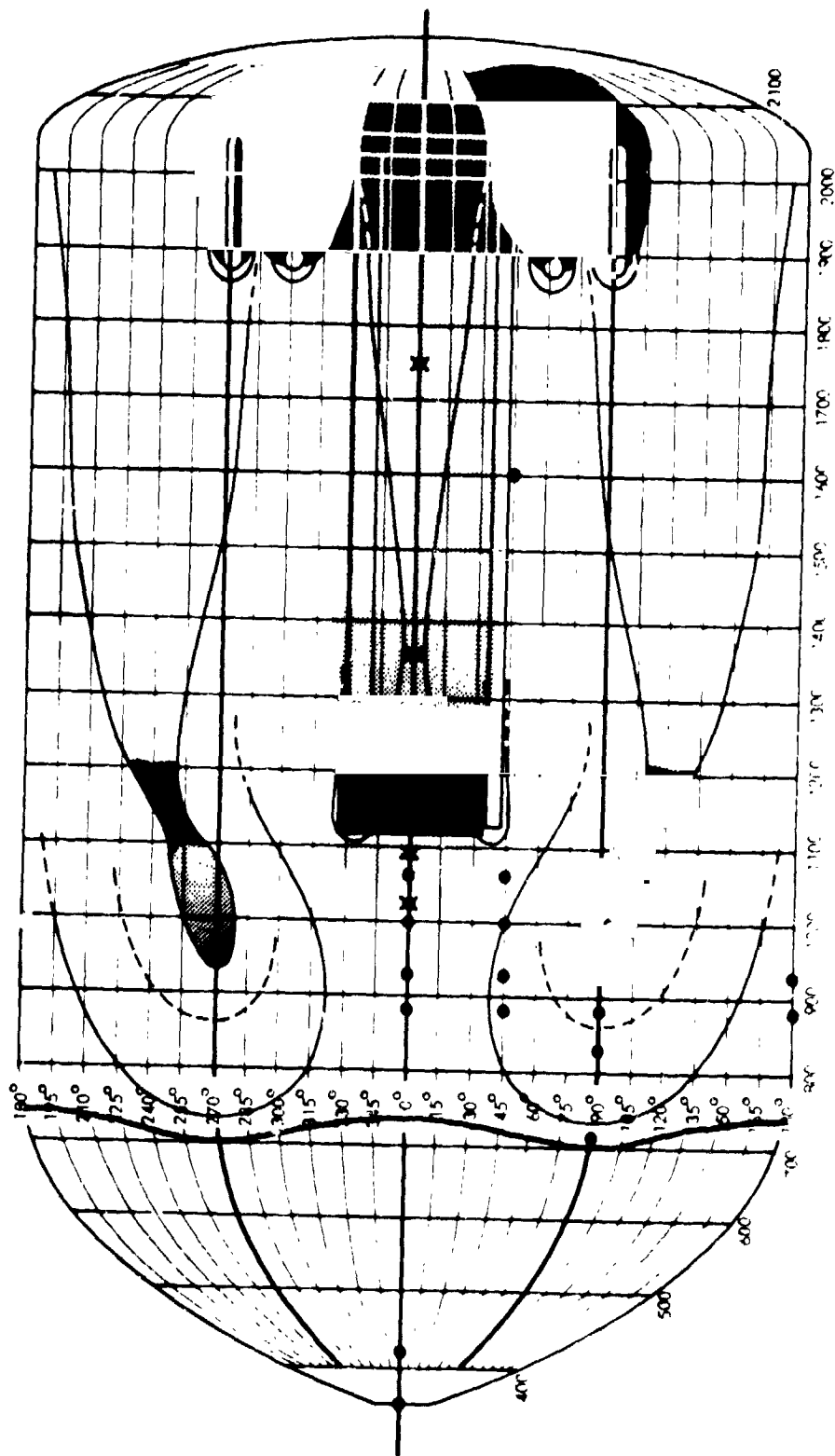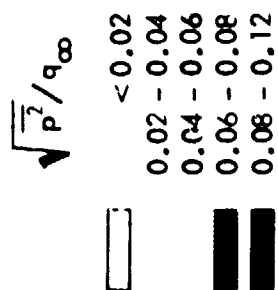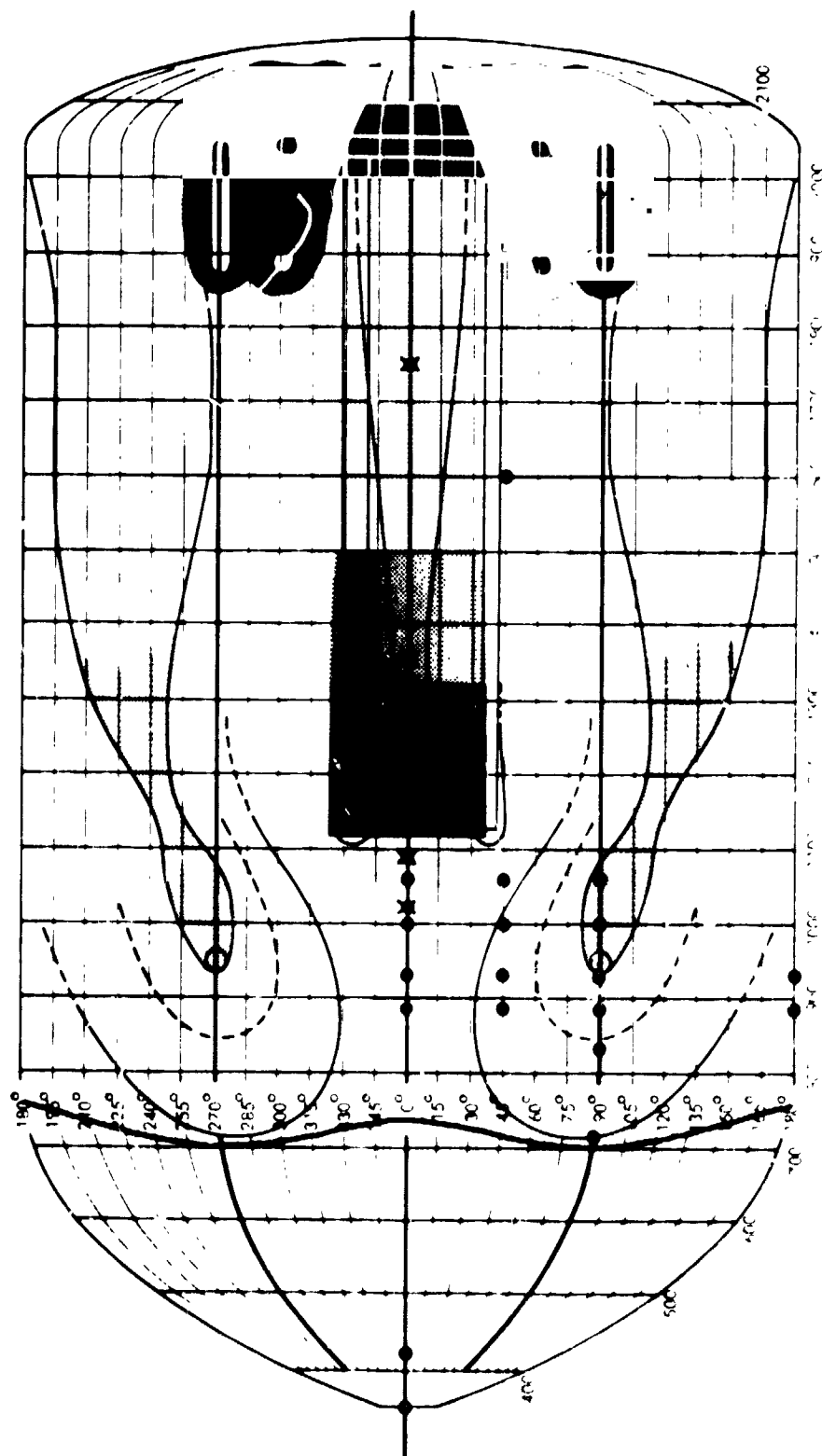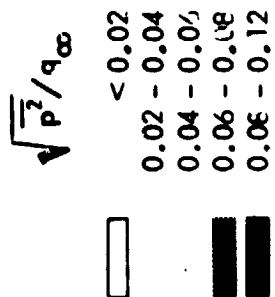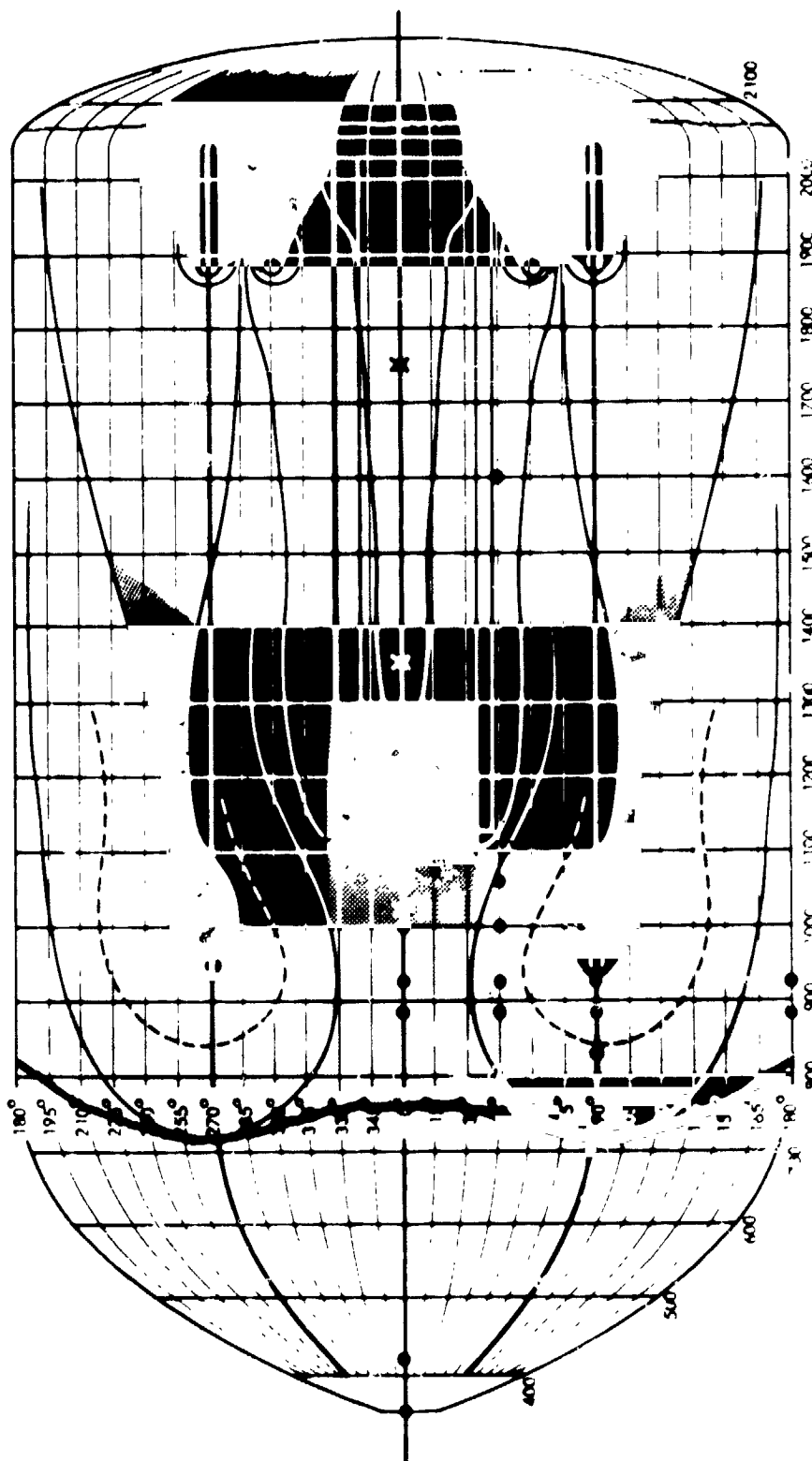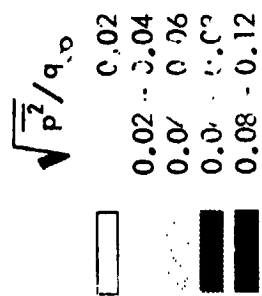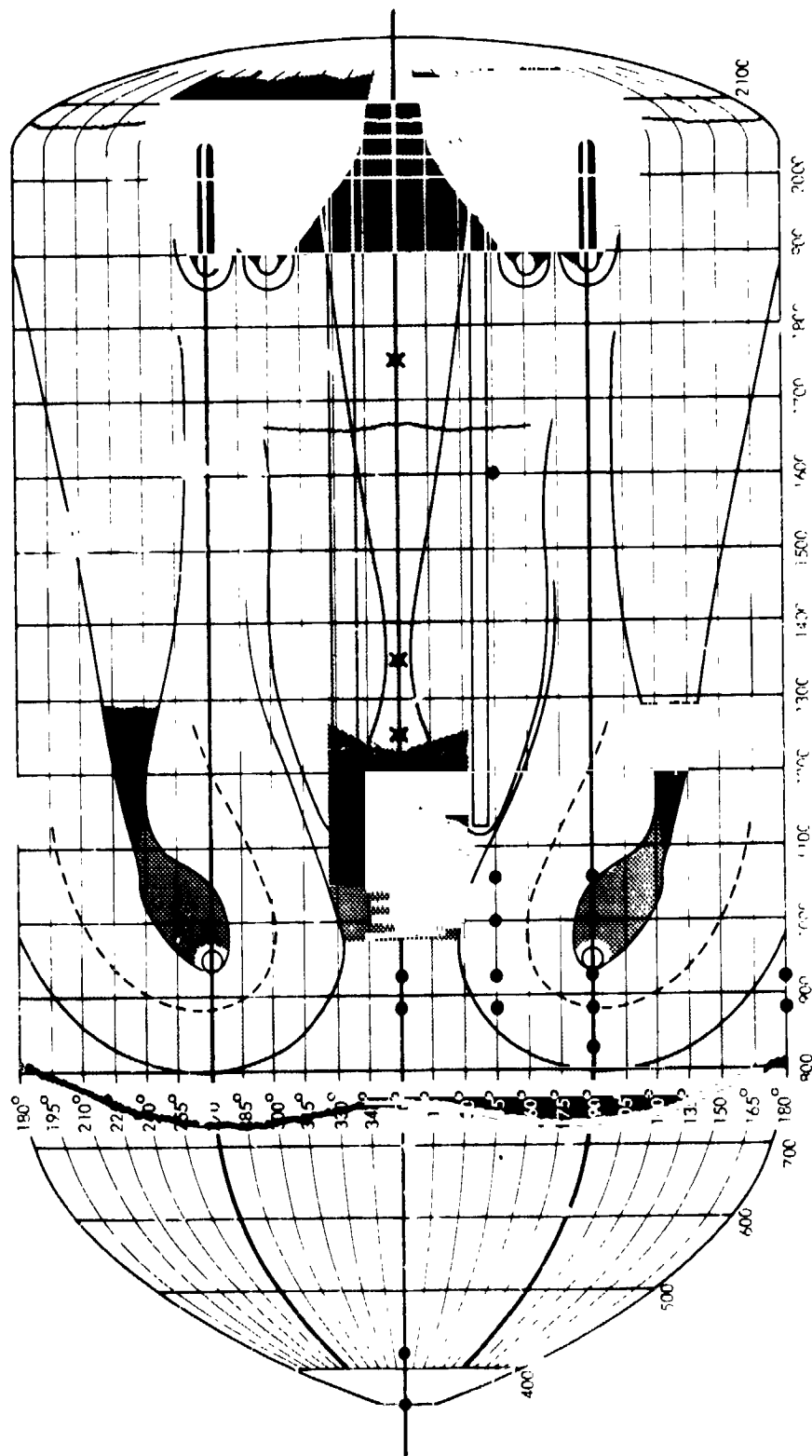
APPENDIX A

SUMMARY OF PREDICTION METHODS FOR
IN-FLIGHT FLUCTUATING PRESSURE ENVIRONMENTS

APPENDIX A

SUMMARY OF PREDICTION METHODS FOR
IN-FLIGHT FLUCTUATING PRESSURE ENVIRONMENTS

1.0   INTRODUCTION

When a vehicle moves through air there are two basic means by which it can produce noise: (1) by its propulsion mechanism (motor-jet, rocket, etc.,) and (2) by its interaction with its surroundings. At low speeds, for example, during and immediately after lift-off, the first of these is by far the dominant one while near or above the speed of sound, mechanism (2) becomes most important.

During any flight cycle for an aerospace vehicle, there are three important phases of the flight which should be investigated in order to assess the structural loading due to fluctuating pressures. These are listed in the chronological order in which they occur.

- Lift-off phase during which acoustic excitation results from the rocket exhaust noise.

- Launch flight to orbit phase, during which rocket exhaust noise diminishes and aerodynamic fluctuating pressures (pseudo-sound) starts to dominate. From an aerodynamic noise viewpoint, this phase becomes most critical at transonic Mach numbers $(0.60 \leq M \leq 1.6)$

- Re-entry phase during which only aerodynamic fluctuating pressures are present.

This Appendix is devoted to the specification of surface fluctuating pressures resulting from unsteady aerodynamic phenomena during the launch phase of flight. Aerodynamic fluctuating pressures (pseudo-sound) are zero at launch and increase to peak values as the vehicle passes through the transonic Mach number range. Previous wind tunnel and flight data show that fluctuating pressures are proportional to free-stream dynamic pressure q_{∞} $(= \gamma P_{\infty} M_{\infty}^2 / 2$, where γ is the ratio of specific heats, P_{∞} is the free-stream static pressure, and M_{∞} is the free-stream Mach number) for a given unsteady flow phenomenon. However, peak fluctuating pressures do not necessarily occur at maximum q_{∞} for certain regions of a vehicle due to the non-homogeneous nature of the flow field. For example, regions of the vehicle exposed to separated flow and the impingement of oscillating shock waves will experience fluctuating pressures at least an

order of magnitude greater than regions exposed to attached flow. Thus, if separated flow and oscillating shock waves are present, say at Mach numbers other than the range of maximum q_∞ , then peak fluctuating pressures will also be encountered at conditions other than at maximum q_∞ . Thus, it is easily seen that vehicle configuration is very important in the specification of fluctuating pressure levels since the source phenomena are high! configuration dependent in addition to varying with Mach number and angle of attack.

In light of the foregoing discussion, one general statement can be made in regard to aerodynamic fluctuating pressures. Regions exposed to the same unsteady phenomenon will experience fluctuating pressure levels which are proportional to free-stream dynamic pressure. Thus, it can be readily seen that a fundamental parameter in the specification of the surface excitation is free-stream dynamic pressure and its variation with Mach number. For a given configuration, Mach number and angle of attack define the phenomena, and dynamic pressure defines the fluctuating pressure levels associated with the phenomena.

Unsteady aerodynamic flow and the attendant fluctuating pressures experienced by aerospace vehicles naturally depend on the flight environments and the geometry of the vehicle. There are an infinite number of possible configurations and any discussion of their fluctuating pressure environment must be general. Practically all experimental data for unsteady aerodynamic flow have been acquired for bodies of revolution which are typical of missile configurations. As a result of these studies, it is well known that certain basic unsteady flow conditions will occur regardless of the detailed geometry of the vehicle. The occurrence of these basic fluctuating pressure phenomena and their statistical properties can be predicted quite accurately. It is convenient to discuss these basic flow conditions for bodies of revolution; however, this is certainly no restriction on either the feasibility or the practicality of predicting their occurrence on more complicated configurations. Thus, in the following paragraphs, general features of typical bodies of revolution are defined and the unsteady flow fields which they encounter are discussed. Furthermore, aerospace vehicles may have a number of protuberances projecting from their surface in which case the flow field is complicated

A-2

by the super-position of the protuberance flow field onto the flow field of the basic structure. Most protuberances are three-dimensional projections and general characteristics of these flows should be considered as separate and unique problems.

2.0 BASIC FLUCTUATING PRESSURE PHENOMENA

Examples of several bodies of revolution are shown in Figure 1. For the purpose of the present discussion, three basic configurations will be considered as specified below:

- Cone-cylinder shroud
- Cone-cylinder-flare shroud
- Cone-cylinder-boattail shroud

Virtually all axisymmetric vehicles fall into one of these categories although numerous modifications to the basic geometry have been employed in the past.

Several fluctuating pressure environments having different statistical properties may exist over a vehicle at any given instant in the flight trajectory. It is convenient to consider three separate Mach number ranges — subsonic, transonic, and supersonic — for each of the three basic shroud configurations. Further, the flow fields will depend on the angle of attack of the vehicle which causes nonsymmetrical loading (both statically and dynamically); however, for the purpose of this discussion, nonsymmetrical loading will not be discussed.

Schematics of subsonic, transonic and supersonic flow fields for the basic configurations are shown in Figure 1. At subsonic speeds, all three configurations experience regions of attached flow and separated flow. The cone-cylinder portion of each configuration induces separated flow immediately aft of the cone cylinder juncture for cones having half-angles greater than approximately 15 degrees. Re-attachment occurs within approximately one diameter aft of the shoulder (depending on cone angle) for the cone-cylinder and boattail configurations, whereas for the flare body, separation may continue over the flare. Both the flare and boattail induce separation for typical configurations. At high transonic speeds, the flow negotiates the shoulder of a cone-cylinder

body without separating, reaches supersonic speed immediately aft of the shoulder and produces a near-normal, terminal, shock wave a short distance aft of the shoulder. The boundary layer immediately aft of the shock may or may not separate depending on the strength of the shock wave. At transonic speeds, the boattail and flare region produce separated flow which may be accompanied by weak shock waves in the vicinity of the separation and reattachment points. At supersonic speeds, the cone-cylinder configurations produce regions of attached flow. For the flare configuration, the separated flow is bounded by shock waves at the separation and reattachment points, whereas for the boattail configuration, separation occurs at the shoulder of the boattail (expansion region) and is bounded at the reattachment point by a shock wave.

It is evident that even simple vehicle shapes, such as cone-cylinders, produce complex and highly nonhomogeneous flow fields at certain Mach numbers — particularly at subsonic and transonic speeds. The unsteady flow phenomena are of particular importance at transonic speeds, since in this range, fluctuating pressures reach maximum values due to their proportionality to dynamic pressure. In order to assess the fluctuating pressure environment of a vehicle of any arbitrary geometry, it is convenient to discuss the statistical properties of the fluctuating pressures for each of the basic types of unsteady flow condition. From Figure 1 it will be noted that the following flow conditions may occur for various regions of a vehicle.

- Attached flow
- Separated flow
- Shock-boundary layer interaction

Each of the above flow conditions exhibits different statistical characteristics. Attached flow pressure fluctuations result from the disturbances within turbulent boundary layers. Separated flow pressure fluctuations result from disturbances within the separated shear layer and instabilities associated with the separation and reattachment points. Pressure fluctuations for shock-boundary layer interaction result from the movement of the shock wave and the static pressure discontinuity associated with the shock wave. The statistical characteristics of each fluctuating pressure environment

that are important in the analysis of structural response may be classified under three parameters:

- The overall ievel
- The power spectrum
- The cross-power spectrum (or narrow band cross correlation)

Each unsteady flow condition with general statistical characteristics will be discussed separately in the following subsections.

2.1   Attached Turbulent Boundary Layers

The surface fluctuating pressures beneath attached turbulent boundary layers have been the subject of both theoretical and experimental study for a number of years. The turbulent boundary layer extends over a considerable portion of the surface of vehicles in flight and, thus, it is considered to be one of the principle sources of aero-acoustic excitation to the vehicle structure. Several years ago, workers such as Kraichman, Lilley, and Hodgson developed theoretical formulations for the fluctuating pressures under turbulent boundary layers and, more recently, several carefully planned experiments have provided additional information on the statistical characteristics of the pertubations. Lowson, Reference 1 , presents a good summary of the results of studies on this subject, with the exception of some recent measurements by NASA-Ames. In Lowson's report, the basic mechanism underlying the production of the surface pressure fluctuations beneath turbulent boundary layers is discussed, together with a presentation of empirical and semi-empirical prediction techniques. This section of the present discussion is a brief overview of Lowson's prediction formulae with the exception of the power spectra, which has been modified to be more consistent with the power spectra at low Strouhal numbers. The following discussion presents a review of the experimental results and prediction formulae in terms of the most important statistical parameters.

Overall Level

The correct method of presenting overall fluctuating pressure levels for surfaces beneath the convected turbulence in boundary layers is in terms of the root-mean-square fluctuating pressure level, $\sqrt{\overline{p^2}}$. Free-stream dynamic pressure, q_∞, local dynamic pressure, q_l, and wall shear stress, τ_ω, have been used to normalize $\sqrt{\overline{p^2}}$ so that meaningful data collapse can be realized throughout the Mach number range. The most generally accepted normalizing parameter is q_∞ and thus, will be used in the current expressions.

The effects of free-stream Mach number, M_∞, on the normalized RMS intensities of the fluctuating pressures in attached flows are shown in Figure 2. There is significant scatter in the data which may be attributed to several factors: 1) background noise and free-stream turbulence in the testing medium, 2) instrumentation quality and the precision of the experimental technique, 3) data acquisition and reduction techniques, etc. For the range of Mach numbers covered in the data of Figure 2, the normalized RMS value of the fluctuating pressure varies from $\sqrt{\overline{p^2}}/q_\infty \approx 0.006$ at subsonic Mach numbers to 0.002 at supersonic Mach numbers. Lowson, Reference 1, proposed the following semi-empirical prediction formula which appears to agree with the general trend in the data:

$$\sqrt{\overline{p^2}}\Big/q_\infty = 0.006/(1 + 0.14 M_\infty^{\,2}) \tag{1}$$

It is important to note that this formula has some theoretical basis and is not strictly an empirical approximation of measured results (see Reference 1). The use of this formula at high supersonic and hypersonic Mach numbers should be done so with the understanding that it has not been verified in this Mach number range and may lead to significant error. However, in the Mach number range up to, say $M_\infty = 3.0$, it is in good agreement with experimental results.

It should be noted that the results presented in Figure 2, particularly the wind tunnel results, were obtained for both homogeneous and stationary flows at free-stream conditions and in the absence of external pressure gradients. Consideration should be given to local conditions which deviate from free-stream conditions.

Power Spectra

Power spectra represent the distributions of the mean square fluctuating pressure with frequency. Power spectra for attached turbulent boundary layers are found to scale on a Strouhal number basis; that is, the frequency is normalized by multiplying by a typical length and dividing by a typical velocity. The advantages of using normalized spectra are obvious since it enables similar, homogeneous, flows to be represented by a single spectrum regardless of the scale of the flow field or the free-stream velocity.

Numerous studies have been conducted to determine the proper parameters to be used to nondimensionalize the spectra for various aero-acoustic environments. Unfortunately, the choice of parameters which best collapses the data appear to be dependent on the nature of the fluctuating pressure environment. In general, free-stream velocity is used as the normalizing velocity parameter, although a typical eddy convection velocity (itself a function of frequency) has been used occasionally. The local convection velocity appears to correspond more closely with the physical situation for fluctuating pressures due to turbulent eddies. Selection of a typical length is more difficult. Boundary layer thickness (δ_b), displacement thickness (δ^*), wall shear stress (τ_ω) and momentum thickness (θ) have all been used by various investigators. The most generally used typical lengths are δ_b and δ^*.

Lowson, Reference 1, proposed an empirical formula for the power spectrum for attached turbulent boundary layers based, primarily, on the experimental results of Speaker and Ailman. In comparing this formula with other data, and in particular, with recent measurements at supersonic speeds by NASA-Ames, the Lowson prediction appears to underestimate the spectral levels at low Strouhal numbers and also gives too large a roll-off at high Strouhal numbers. Therefore, a new formula is presented

which appears to be more representative of experimental findings throughout the Mach number range. In this formula, it will be noted that δ^* and U_∞ (the free-stream velocity) have been used as normalizing parameters. The power spectral density, $\phi(\omega)$ is given by the relation:

$$\frac{\phi(\omega) U_\infty}{q_\infty^2 \delta^*} = \frac{(\overline{P^2}/q_\infty^2)}{\dfrac{\omega_0 \delta^*}{U_\infty} \left\{ 1 + (\omega/\omega_0)^{0.9} \right\}^{2.0}} \qquad (2)$$

where

$$\omega_0 = 0.5 \frac{U_\infty}{\delta^*}$$

$$\overline{P^2}/q_\infty^2 = \frac{(0.006)^2}{(1 + 0.14 M_\infty^2)^2}$$

$$\delta^* = \delta_b/8 \quad \text{for} \quad M < 1.0$$

$$\delta^* = \frac{(1.3 + 0.43 M_\infty^2)\, \delta_b}{10.4 + 0.5 M_\infty^2 \left[1 + 2.10^{-8}\, R_e \right]^{1/3}} \qquad \text{for} \quad M > 1.0$$

$$\delta_b = x \left[0.37\, R_e^{-0.2} \left\{ 1 + \left(\frac{R_e}{6.9 \cdot 10^7} \right)^2 \right\}^{0.1} \right]$$

x = Downstream distance from the leading edge

R_e = Reynolds number = $U_\infty\, x/\nu$

ν = Kinematic viscosity

A comparison of the predicted power spectrum with experimental spectra is presented in Figure 3.

Cross-Power Spectra

The final requirement in determining the characteristics of the fluctuating pressure field of the turbulent boundary layer is to define the narrow band, space correlation function or co-power spectral density. This parameter is the key function needed to describe an impinging pressure field on a structure in order to calculate the induced mean-square response of the structure (see, for example, Reference 17 for the structural response computational technique). The spatial correlation properties of a fluctuating pressure field can be obtained only from a careful and detailed examination of the field at a large number of points. Measurements by several investigators have shown that the co-power spectral density of turbulent boundary layer pressure fluctuations in the direction of the flow can be approximated by an exponentially damped cosine function, and the lateral co-spectral density can be approximated by an exponential function. The general form of the cross-power spectral density is:

$$S_{pp}(\zeta, \eta, \omega) = \phi(\omega) A(\zeta, \eta, \omega) \cos\left(\frac{\omega \zeta}{U_c}\right) \qquad (3)$$

where $A(\zeta, \eta, \omega)$ is the modulus of the cross-power spectral density, and $\phi(\omega)$ is the power spectral density of the homogeneous field.

Here, it is assumed that the pressure field is homogeneous, in the sense that the cross-power spectral density is a function only of the separation distances (ζ in the longitudinal direction and η in the lateral direction) so that it is independent of the actual positions (say x and $x + \zeta$ longitudinally and y and $y + \eta$ laterally). Further, ω and U_c are the circular frequency and convection velocity, respectively. Assuming that $A(\zeta, \eta, \omega)$ is separable into its longitudinal and lateral components, and normalizing by the power spectral density of the homogenous field gives (Reference 1):

$$G_{pp}(\zeta, \eta, \omega) = G_\zeta(\zeta, \omega) G_\eta(\eta, \omega) = \left\{ A_\zeta(\zeta, \omega) \cdot \cos\left(\frac{\omega\zeta}{U_c}\right) \right\} \cdot A_\eta(\eta, \omega)$$

$$= C(\zeta, \omega) \cdot C(\eta, \omega) \tag{4}$$

where $C(\zeta, \omega)$ and $C(\eta, \omega)$ are the correlation coefficients in the longitudinal and lateral directions, respectively. The assumed separable form leads to the prediction that the magnitude of C is constant along straight lines on the surface, forming a diamond pattern surrounding the origin. This characteristic is somewhat physically unreasonable (see Reference 2); however, for purposes of calculating the induced structural response the assumption of separability greatly simplifies the mathematics and, hence, it is generally accepted. However, Lowson (Reference 1) notes that a more likely form for the lines of constant amplitude would be elliptic, suggesting that the usual separable solution underestimates the correlation area by $\pi/2$. Thus, integration of formula containing the cross-spectral density function should be multiplied by a factor of $\pi/2$ to allow for its probable underestimate of the correlation area at any frequency.

Measurements of the correlation coefficients have been made by Bull and others (see Reference 1) and the results are presented in Figures 4a and 4b. It is seen that the data in Figures 4a and 4b have been collapsed based on Strouhal numbers $\frac{\zeta\omega}{U_c}$ and $\frac{\eta\omega}{U_c}$. From these data, the following empirical expressions were derived for the correlation coefficients:

$$C(\zeta, \omega) = \exp\left(-0.10 \left|\zeta\right| \omega/U_c\right) \cdot \cos\left(\frac{\omega\zeta}{U_c}\right) \tag{5}$$

$$C(\eta, \omega) = \exp\left(-0.715 \left|\eta\right| \omega/U_c\right) \tag{6}$$

These correlation curves have been inserted in Figures 4a and 4b for comparison. Typical values of the convection velocity (itself a function of frequency) for subsonic flow are $U_c = 0.6\ U_\infty$ for the small scale eddies near the wall and $U_c = 0.9\ U_\infty$ for the large scale eddies near the outer edge of the boundary layer.

The accuracy of Equations (5) and (6) break down at small values of $\dfrac{\omega \zeta}{U_c}$; however, in Reference 3, Bull presents measured asymptotic values of the correlation coefficients for small values of $\dfrac{\omega \zeta}{U_c}$ and $\dfrac{\eta \zeta}{U_c}$. Based on these data, the Equations (5) and (6) may be corrected to include the lower frequencies, and the resulting expressions are:

$$C(\zeta, \omega) = \exp\left(-0.10\ \left|\zeta\right|\ \omega/U_c\right) \cdot \exp\left(-0.27\left|\zeta\right|\Big/\delta_b\right) \cdot \cos\left(\frac{\omega \zeta}{U_c}\right) \quad (7)$$

$$C(\eta, \omega) = \exp\left(-0.72\ \left|\eta\right|\ \omega/U_c\right) \cdot \exp\left(-2.0\ \left|\eta\right|\Big/\delta_b\right) \quad (8)$$

These expressions appear to be valid at both subsonic and supersonic speeds.

2.2 Separated Flow

Separated flows as induced by steps, wedges, flares and other, basically two-dimensional geometric changes have undergone considerable study only in recent years. Considerably less data is available on the fluctuating pressure environments within separated flow regions than is the case with attached turbulent boundary layers. Furthermore, there are various types of separated flows and little is known of the similarities and differences of their statistical properties. Example separated flow environments are listed below:

- Blunt body-induced separation (as occur at cone-cylinder and flare-cylinder expansion corners at subsonic Mach numbers)

- Flare-induced, step induced, and wedge-induced separation (as occur in compression corners)

- Shock-induced separation (as occur on cylinders, airfoils, etc., beneath terminal shock waves at transonic speeds and due to shock wave impingement at supersonic speeds)

- Boattail-induced and rearward facing-step-induced separation (such as occur in the base region of launch vehicles).

All of the foregoing environments differ to some degree in their aerodynamic structure. However, some basic comments can be made in regard to their fluctuating pressure characteristics. First, all of these environments may be regarded as two-dimensional type separated flows having mean separation and reattachment lines which are normal to the free-stream. Second, a general characteristic is that if the flow separates from an expansion corner, the separation line is quite stable in that oscillations which produce fluctuating pressures are not generated. However, if separation occurs, say, on the cylindrical portion of a payload shroud (flare induced separation) the separation point is unstable and may produce significant fluctuating pressures, particularly at supersonic speeds where the separation is accompanied by an oblique shock wave.

Third, the reattachment point of the separated flow field produces rather large fluctuating pressure levels for virtually all types of separated flow fields. The region within the separated flow field (between the separation and reattachment points) is a fairly homogeneous environment which is characterized by fluctuating pressure levels greater than those for attached flow but less than those encountered at the separation and reattachment points. Example data for various separated flow fields are presented in the following sections.

Overall Level

A typical example of the fluctuating pressures resulting from blunt-body separation is shown in Figure 5 (results taken from Reference 18). These data were obtained at high subsonic Mach numbers for a 25-degree cone-cylinder configuration. The axial distribution of $\sqrt{\overline{P^2}} / q_\infty$ shows a relatively nonhomogeneous environment with a peak level which moves aft with increasing Mach number. The peak in $\sqrt{\overline{P^2}} / q_\infty$ results from the reattachment of the separated flow from the shoulder. Thus, the extent of the separated region increases with increasing Mach number. Peak levels of rms fluctuating pressure reach 11 percent of free-stream dynamic pressure at a free-stream Mach number of 0.70, and results from the instability of the reattachment point. It will be noted that the fluctuating pressure levels near the shoulder (X/D = 0) are relatively low (same order of magnitude as generally found within the homogeneous region of two-dimensional separated flows and typical of the environment for separated shear layers) thus indicating that the separation point which occurs at the shoulder is relatively stable. Separated flow over the boattail region of a bulbous vehicle may be expected to exhibit fluctuating pressure characteristics very similar to the cone-cylinder; however, the blunt-body separation on a cone-cylinder body is limited to the subsonic speed range, whereas, the boattail configuration may induce separation at all Mach numbers.

Typical fluctuating pressure data for flare-induced separation are presented in Figure 6 (results taken from Reference 14). These data clearly show the region of homogeneous separated flow, bounded on the upstream by the oscillating shock wave (forward peak in $\sqrt{\overline{P^2}}/q_\infty$), and on the downstream by the reattachment perturbations (aft peak in $\sqrt{\overline{P^2}}/q_\infty$). Surface fluctuating pressures for the separated flow region range from 1.5 to 2.7 percent of the free stream dynamic pressure. Levels associated with the upstream shock wave generally range from 4 to 8 percent of the free-stream dynamic pressure (see Reference 14); whereas, levels in the region of reattachment may range from 6 to 12 percent of q_∞ and agree reasonably well with the reattachment levels for blunt body separation. Further discussion of shock-wave oscillation data is presented in a later section.

The variation of fluctuating pressure level, normalized by free-stream dynamic pressure, with local Mach number (M_ℓ) for various separated flow environments downstream of expansion corners is presented in Figure 7. The regions aft of cone-cylinder junctures and rearward-facing steps, and in the near wake of boattail configurations are represented by the data presented in Figure 7. These environments will be referred to as expansion induced separated flows and it will be noted that the attendant fluctuating pressures exhibit the same general trend with local Mach number. The largest levels occured at low Mach numbers and decreased as local Mach numbers increased. These data represent the region of plateau static pressure and the tolerance brackets on the data represent the variations due to non-homogeneous flow within the region of constant static pressure rather than scatter in the measurements. A good empirical approximation to these experimental measurements is:

Expansion Induced Separated Flow:

$$\sqrt{\overline{P^2}}/q_\infty = \frac{0.045}{1 + M_\ell^2} \tag{9}$$

This equation is similar in form to that previously proposed for attached turbulent boundary layers.

Fluctuating pressure measurements for the region of plateau static pressure upstream of compression corners are presented in Figure 8. The regions immediately upstream of forward-facing steps, wedges, and flares are represented by the data presented in Figure 8. Also, the previous fluctuating pressure data for expansion induced separated flow, shown in Figure 7, are presented in this figure for comparison. In general, the compression corner data show an increase in fluctuating pressure level with increasing free-stream Mach number in the range, $1.0 \leq M_{\infty} \leq 2.0$ — reaching a constant level at Mach numbers above 2.0. Free-stream Mach number is used here because adequate data is not available for determining the local Mach number in the vicinity of the compression induced separated flow region. Derivation of an empirical prediction formula for the fluctuating pressure level within compression induced separated flows has not been attempted at this time.

Power Spectra

The most comprehensive available data for power spectra of the fluctuating pressure within separated flows was obtained for the homogeneous region of compression corners at supersonic Mach numbers (References 14, 19, 20 and 21). These data, presented in Figure 9, were obtained for forward facing steps, wedges and conical frustums. All data, represented by the cross-hatched band, showed a distinct similarity in spectral characteristics when compared using normalized spectral level and frequency expressed as functions of local velocity, free-stream dynamic pressure, and local boundary layer thickness. A number of velocity, length and pressure parameters were used to collapse the data; however, local velocity (U_ℓ), local boundary layer thickness (δ_ℓ) and free-stream dynamic pressure appeared to be adequately representative of the parameter dependence of the fluctuating pressures for the configurations studied. Power spectra of the fluctuating pressures within the homogeneous region of separated flows may be represented by the following empirical formula:

$$\frac{\phi(f) U_\ell}{q_\infty^2 \delta_\ell} = \frac{\overline{P^2}/q_\infty^2}{\frac{f_0 \delta_\ell}{U_\ell} \left\{ 1 + \left(f/f_0 \right)^{0 \cdot 83} \right\}^{2.15}} \tag{10}$$

where $\qquad f_0 = 0.17 \dfrac{U_\ell}{\delta_\ell}$

$\overline{P^2}/q_\infty^2 = \dfrac{0.045}{1+M_\ell^2}$, Figure 7 , for expansion induced separated flows.

$\overline{P^2}/q_\infty^2 = $ the results as determined in Figure 8 for compression induced separated flows.

and the subscripts ℓ and ∞ refer to local and free-stream conditions respectively.

It is anticipated that Equation 10 can be used with good accuracy to predict the power spectra for fluctuating pressures within the homogeneous region of expansion induced separated flows although it was derived based on data taken in compression corners.

Cross-Power Spectra

Typical cross-power spectra for the homogeneous region of two-dimensional separated flows are presented in Figure 10. Again, noting that the co-spectral density is the same as the narrow-band spatial correlation, it is seen that the separated flow exhibits spatial coherence very similar to that of attached turbulent boundary layers. The damping of the sinusoidal cross spectra for separated flow is exponential at high values of $\omega \zeta/U_c$ as is the case for attached flow. Thus as a first approximation, the normalized longitudinal co-spectra may be represented by:

$$C(\zeta, f) = e^{-a \omega \zeta/U_c} \cos \frac{\omega \zeta}{U_c} \tag{11}$$

The damping coefficient, a, is dependent on free-stream Mach number according to the results presented in Reference 14. The Chyu and Hanely results show damping coefficients ranging from approximately 0.13 at $M_\infty = 2.5$ to a value of 0.33 at $M_\infty = 1.6$. This suggests that the turbulence structure in separated flows decays somewhat more rapidly than for attached flow which has a coefficient of exponential decay of 0.10. It should be noted that the exponential decays represent the envelope of the cross-spectra for various spatial distances, ς. For a given value of ς, the cross-spectra can be represented by the exponential envelope only at high frequencies, the lower limits of which increase with increasing distance between measurement points.

The loss of coherence at low frequencies precludes a general collapse of the data using a constant damping coefficient. This problem was overcome by Coe and Rechtien, Reference 20, by introducing an attenuation coefficient which is related to the nor-malized modulus of the cross-power spectral density by

$$\left| G\left(\varsigma, \frac{f\,\delta_\ell}{U_\ell}\right)\right|_{norm} = e^{-\alpha\,\varsigma} \tag{12}$$

The normalized modulii for available or selected transducer spacings, ς, were curve-fitted by an exponential function using the method of least squares to obtain a non-dimensional attenuation-coefficient function $\alpha\left(\varsigma, f\,\delta_\ell/U_\ell\right)\cdot h$ in References 19-21. The parameter h is the height of the protuberances used to generate the separated flow field. Empirical approximations of the attenuation coefficient, based on the experi-mental results of Coe and Rechtien, are:

$$\alpha\left(\varsigma, \frac{f\,\delta_\ell}{U_\ell}\right) = 0.75/\text{in.} \quad,\quad \frac{f\,\delta_\ell}{U_\ell} < 6\times10^{-3} \tag{13}$$

A-17

$$\alpha\left(\zeta, \frac{f\delta_\ell}{U_\ell}\right) = 0.75\left[\frac{f\delta_\ell/U_\ell}{\left(f\delta_\ell/U_\ell\right)_0}\right], \tag{14}$$

$$6 \times 10^{-3} \leq \frac{f\delta_\ell}{U_\ell} \leq 6 \times 10^{-2}$$

$$\text{where} \qquad \left(\frac{f\delta_\ell}{U_\ell}\right)_0 = 6 \times 10^{-3}$$

$$\alpha\left(\zeta, \frac{f\delta_\ell}{U_\ell}\right) = 1.5 / \text{in.} \quad, \quad \frac{f\delta_\ell}{U_\ell} > 6 \times 10^{-2} \tag{15}$$

Lateral Direction

$$\alpha\left(\eta, \frac{f\delta_\ell}{U_\ell}\right) = 0.75 / \text{in.} \quad, \quad \frac{f\delta_\ell}{U_\ell} < 6 \times 10^{-3} \tag{16}$$

$$\alpha\left(\eta, \frac{f\delta_\ell}{U_\ell}\right) = 0.75 / \text{in.}\left[\frac{f\delta_\ell/U_\ell}{\left(f\delta_\ell/U_\ell\right)_0}\right]^{0.3} \quad, \quad \frac{f\delta_\ell}{U_\ell} \geq 6 \times 10^{-3} \tag{17}$$

$$\text{where} \qquad \left(\frac{f\delta_\ell}{U_\ell}\right)_0 = 6 \times 10^{-3}$$

It will be noted that the longitudinal and lateral attenuation coefficients are the same at Strouhal numbers, $f\delta_\ell/U_\ell < 6 \times 10^{-2}$ and that the lateral attenuation coefficient becomes larger than the longitudinal value at $f\delta_\ell/U_\ell \geq 6 \times 10^{-2}$. It was pointed out in Reference 19 that this spatial characteristic indicates that the predominant turbulence is nonconvective at the lower frequencies and that contours of equal

correlation would be circular; whereas, at $f\delta_\ell/U_\ell > 6 \times 10^{-2}$ the divergence of the longitudinal and lateral attenuation coefficients indicate a progressively extended correlation pattern in the direction of the free-stream with increasing frequency. This statement is not entirely true since the usual separable form of the cross-power spectral density leads to the prediction that the magnitude of the normalized modulus is constant along straight lines on the surface, forming a diamond pattern surrounding the origin rather than a circular or elliptic pattern. Under the assumption of separability of the longitudinal and lateral cross-power spectra, the following equations (which employ the attenuation coefficient) may be used as prediction formula for the normalized longitudinal and lateral co-spectra.

Longitudinal Co-Spectra

$$C\left(\zeta,\ \frac{f\delta_\ell}{U_\ell}\right) = e^{-\alpha_\zeta\ \zeta}\ \cos\ \frac{\omega\zeta}{U_c} \tag{18}$$

Lateral Co-Spectra

$$C\left(\eta,\ \frac{f\delta_\ell}{U_\ell}\right) = e^{-\alpha_\eta\ \eta} \tag{19}$$

where $\qquad \alpha_\zeta = \alpha\left(\zeta,\ \dfrac{f\delta_\ell}{U_\ell}\right)\qquad$ as defined in Equations 13, 14 and 15.

$\qquad\qquad\quad \alpha_\eta = \alpha\left(\eta,\ \dfrac{f\delta_\ell}{U_\ell}\right)\qquad$ as defined in Equations 16 and 17.

2.3 Shock-Wave Oscillation

Generally, shock wave oscillation produces the most intense fluctuating pressure levels that are usually encountered by a vehicle. As for the case of separated flow, there are many types of shock-wave oscillation and little is known in regard to the similarities and differences of their statistical parameters. Typical shock waves encountered by vehicles are:

- Terminal shock waves for regions of transonic flow

- Displaced oblique shock waves as induced by the separated flow in compression corners at local supersonic speeds

- Reattachment shock waves in the vicinity of the reattachment point for separated flows generated by both compression and expansion corners.

- Impingement shock waves as caused by local bodies such as strap-on rockets.

All shock waves may be expected to produce similar fluctuating pressure environments since the movement of the shock wave results from the interaction with the separated flow at the foot of the shock wave (see Reference 19) and the fluctuating pressure is the result of the modulation of the pressure gradient through the shock wave. A special case of shock wave oscillation is referred to as an alternating flow condition, whereby, the flow at an expansion corner intermittently fluctuates between a separated and attached condition. This environment is illustrated schematically in Figure 11 for a 25 degree cone angle together with the more common terminal shock—wave oscillation case. Example data for various shock wave oscillation environments are presented in the following sections.

Overall Level

The axial distribution of rms fluctuating pressure resulting from terminal shock wave oscillation is shown in Figure 11 (from Reference 18). A special case of terminal shock wave oscillation results when the terminal shock wave moves forward to the expansion shoulder of a cone-cylinder. For this case, the flow intermittently fluctuates between the blunt-body separated flow condition and the attached flow condition at high sub-sonic (low transonic) Mach numbers. This condition represents an alternating unbalance between the large pressure rise through the shock wave that exceeds the values required to separate the flow and the small pressure rise that is too small to maintain fully separated conditions.

Extremely large fluctuating pressures result from this condition; however, it should be noted that this phenomenon occurs over a small Mach number range and generally is of very low frequency. Thus for large Mach number transients, this phenomenon may not occur. On the other hand, some experimental studies using aeroelastic wind tunnel models indicate that this phenomenon may become coupled with the vibrational response of vehicles such that flutter in the lower order bending modes would result for certain configurations — particularly for bulbous shaped payloads on rather slender launch vehicles.

As Mach number is increased above the range of alternating flow, the localized oscillation of the shock wave produces intense fluctuating pressures for the region in close proximity to the shock wave as shown in Figure 11. The shock wave moves aft with diminishing strength with increasing Mach number such that the rms fluctuating pressure levels also decreases. In addition to the results presented in Figure 11, the fluctuating pressures which occur at the separation and reattachment points for separated flow over compression corners (Figure 6) are fairly complete examples of shock-wave oscillation data.

A-21

Power Spectra

Only recently has comprehensive data been presented on the spectral characteristics
of shock-wave oscillation. Much of the previous data were presented in linear—
linear graphical form rather than using log—log scales. As a result, much resolution
was lost at the high frequencies. Recent experimental data by Coe and Richtien
(Reference 20) gives a clearly defined spectrum for shock wave oscillation at $M_\infty = 2.0$;
however, data at other Mach numbers have not been published. Data obtained for
three-dimensional protuberance flows do agree with the Coe and Richtien data and
thus substantiates their limited published results. The normalized power spectra for
shock-wave oscillation for both two- and three-dimensional protuberances (References
18 and 19) are presented in Figure 12. The power spectrum shows a relatively steep
roll-off starting at a Strouhal frequency $(f\,\delta_0/U_0)$ of 1×10^{-2}, where the subscript
0 denotes local velocity and boundary layer thickness upstream of the shock wave. The
roll-off is 8 dB per octave for the range $1 \times 10^{-2} \leq f\,\delta_0/U_0 \leq 2 \times 10^{-1}$ and above
this range the roll-off changes suddenly to 4 dB per octave. These unique spectral
characteristics of shock-wave induced fluctuating pressures are explained by the
physical behavior of the shock-wave oscillation and the resulting pressure time history.
The shock wave is basically a pressure discontinuity which becomes slightly distorted
by the boundary layer such that a finite gradient through the shock wave is observed
at the surface. Oscillation of the shock wave produces a wave form which approaches
a random-rectangular wave as the displacement of the oscillation increases. Superim-
posed upon this signal is the low amplitude, high frequency disturbance associated
with the attached boundary layer (for that portion of the signal when the shock wave

is aft of the measurement point) and the moderate amplitude and frequency disturbances
associated with separated flow (for that portion of the signal when the shock wave is
forward of the measurement point). The roll-off rate of the power spectrum for a ran-
dom-rectangular wave form is 6 dB per octave which is 2 dB lower than the experi-
mentally observed value. Above $f\,\delta_0/U_0 = 2 \times 10^{-1}$, the power spectral density

for the random modulation of the shock wave diminishes below the power spectral density for the turbulence portion of the signal. Thus, the roll-off rate changes to a value roughly equal to that for separated flow since this environment is the larger of the two turbulence generating mechanisms (the other being attached flow).

Noting that the power spectra for shock wave oscillation is composed of 1) low frequency spectral energy of the shock wave and 2) high frequency spectral energy of the separated flow and attached boundary layer, the resulting empirical formula for the power spectra may be written as a combination of power spectra of the contributing sources:

$$\left[\phi(f)\right]_{SW}^{H} = \left[\phi(f)\right]_{SW}^{I,H} + k_{1}\left[\phi(f)\right]_{S}^{H} + k_{2}\left[\phi(f)\right]_{A}^{H} \qquad (20)$$

where the subscripts and superscripts denote the following:

Subscripts: SW - shock wave

S - separated flow

A - attached flow

Superscripts: I - absence of viscosity (inviscid)

H - homogeneous flow

The constants, k_{1} and k_{2} are weighting functions which account for that portion of the total energy resulting from the presence of viscous flow in the form of separated flow and attached flow respectively. It should be noted that the two secondary environments (separated flow and attached flow) are not simultaneously superimposed on the shock wave signal but rather are time shared. This, together with the fact that these environments may be correlated with the gross motion of the shock wave results in values of k_{1} and k_{2} less than 1.0. Finally, for peak overall levels of shock wave oscillation (corresponding to a point located at the mean position of the shock wave) the contribution of attached flow is negligible in comparison to that for separated flow. Thus, Equation 20 may be simplified to

A-23

$$\left[\phi\,(f)\right]_{SW}^{H} \;=\; \left[\phi\,(f)\right]_{SW}^{I,\,H} + k_{1}\left[\phi\,(f)\right]_{S}^{H} \tag{21}$$

Based on the experimental data of Reference 19, the power spectra $\left[\phi(f)\right]_{SW}^{I,\,H}$ for shock wave oscillation in the absence of viscous flow normalized by local inflowing boundary layer thickness and velocity and free-stream dynamic pressure is given by:

$$\left[\frac{\phi(f)\,U_{0}}{q_{\infty}^{2}\,\delta_{0}}\right]_{SW}^{I,\,H} \;=\; \frac{\left(\overline{P^{2}}\Big/q_{\infty}^{2}\right)_{SW}^{I,\,H}}{\left(\dfrac{f_{0}\,\delta_{0}}{U_{0}}\right)_{SW}\left\{1+\left(f/f_{0}\right)^{1.55}\right\}^{1.7}} \tag{22}$$

where:

$$\left[\overline{P^{2}}\Big/q_{\infty}^{2}\right]_{SW}^{I,\,H} \;=\; \left[\overline{P^{2}}\Big/q_{\infty}^{2}\right]_{SW}^{H} - k_{1}\left[\overline{P^{2}}\Big/q_{\infty}^{2}\right]_{S}^{H}$$

$\left[\overline{P^{2}}\Big/q_{\infty}^{2}\right]_{SW}^{H}$ – overall level of shock oscillation peak corresponding to the mean location of the shock wave.

$\left[\overline{P^{2}}\Big/q_{\infty}^{2}\right]_{S}^{H}$ – overall level of homogeneous separated flow as defined from Figures 7 and 8.

The subscript 0 denotes local velocity and boundary layer thickness upstream of the shock wave.

$$\left(\frac{f_0 \delta_0}{U_0} \right)_{SW} = 1 \times 10^{-2}$$

$$k_1 = 0.25$$

determined empirically from experimental data of Reference 19

Substitution of Equations 10 and 22 into Equation 21 gives the final expression for the power spectra for shock wave oscillation.

$$\left[\frac{\phi(f)\, U_0}{q_\infty^2\, \delta_0} \right]_{SW}^{H} = \frac{\left(\overline{P^2} \big/ q_\infty^2 \right)_{SW}^{I,H}}{\left(\dfrac{f_0 \delta_0}{U_0} \right)_{SW} \left\{ 1 + \left(f / f_0 \right)^{1.55} \right\}^{1.7}} +$$

$$0.25\ \frac{\left(\overline{P^2} \big/ q_\infty^2 \right)_{S}^{H}}{\left(\dfrac{f_0 \delta_0}{U_0} \right)_{S} \left\{ 1 + \left(f / f_0 \right)^{0.83} \right\}^{2.15}} \quad (23)$$

where $(f_0 \delta_0 / U_0)_S$ is now defined for conditions upstream of the shock wave.

A comparison of the predicted power spectra for shock-wave oscillation with experimental measurements is presented in Figure 13. Also shown in the upper right hand corner of this figure is the variation in $\sqrt{\overline{P^2}}/q_\infty$ with distance upstream from the 45 degree wedge. It should be noted that this prediction formula holds true only at a point corresponding to the mean location of the shock wave. On either side of the shock wave, the influence of the shock diminishes rapidly due to its small displacement such that the environment is basically either attached or separated flow with some low frequency intermittency due to the shock wave. It is convenient to refer to these regions as non-homogeneous attached and separated flows and they will be discussed later in Section 2.4.

Cross-Power Spectra

Very little data has been published in the form of cross-power spectra of fluctuating pressures beneath oscillating shock waves. Because oscillating shock waves at a given flight condition are confined to relatively small areas of the vehicle surface, it is extremely difficult to define the spatial characteristics of the attendant fluctuating pressures. Fluctuating pressures in the vicinity of the shock wave are highly non-homogeneous; although they do appear to be related in both spectral shape and spatial coherence. The only significant results or the spatial coherence of fluctuating pressures in the vicinity of shock-waves are those by Coe and Rechtien (Reference 20) Their data indicate that the fluctuating pressures generated by the shock wave are related only at frequencies below $f\delta_0/U_0 = 0.08$ for the region immediately downstream of the mean location of the shock wave (Figure 14). For the region immediately upstream of the shock-wave, a small degree of coherence is also evident in this frequency range as well as at $f\delta_0/U_0 \geq 0.2$. A comparison of the power spectra and coherence function shows some very interesting characteristics of shock-induced fluctuating pressures. First, the power spectra of fluctuating pressures on each side of the peak level point show large low frequence energy which can be identified as having the same basic characteristics as the shock wave spectrum for $f\delta_0/U_0 \leq 0.08$. This is confirmed by the coherence of the data over the same frequency range $\left(f\delta_0/U_0 \leq 0.08 \right)$. For $f\delta_0/U_0 > 0.08$, power spectra immediately upstream and downstream of the shock wave show spectral characteristics identical to attached turbulent boundary layer and separated flow, respectively. Thus, for $f\delta_0/U_0 > 0.8$, the spatial correlation of fluctuating pressure immediately upstream of the peak should be characteristic of attached flow; whereas, immediately downstream of the peak they should be characteristic of separated flow. However, when the spatial correlation is normalized by the power spectral densities to obtain the coherence function, this coherence appears to be minimized due to the large spectrum level for the point of peak fluctuating pressure. Further discussion on this

characteristic will be given later in the section on non-homogeneous attached and separated flows.

The spatial decay of the low frequency, shock induced fluctuating pressure in the longitudinal direction as shown in Figure 14 may be represented by an exponential coherence function as follows:

$$\gamma \left(\zeta, \frac{f \delta_0}{U_0} \right) = e^{-80 \; f \delta_0 / U_0} \tag{24}$$

A comparison of this empirical prediction with experimental data is presented in Figure 14. It should be noted that, as separation distance is increased, the above formula fails to account for the low coherence at low frequencies. However, because the large non-homogeneous effects associated with the flow in close proximity of the shock wave, the application of classical statistical methods to define the spatial characteristics for large separation distances may be questionable. Thus, for regions under the peak, Equation 24 is felt to be an accurate representation of the spatial characteristics of the fluctuating pressures in the longitudinal direction.

The longitudinal co-spectra may be written:

$$C \left(\zeta, f \right) = e^{-40 \; f \delta_0 / U_0} \cos 2\pi \frac{f \delta_0}{U_0} \tag{25}$$

Published data is not available on the transverse spatial characteristics of shock-induced fluctuating pressures. However, it is anticipated that these disturbances will be reasonably correlated over much larger distances in the transverse direction than in the longitudinal direction because of the continuity of the shock wave in the plane normal to the flow.

A-27

2.4 Non-Homogeneous Attached and Separated Flows

Non-homogeneous attached and separated flows are defined as environments which are basically attached or separated; however, the statistical properties of their attendant fluctuating pressures vary with spatial location. Examples to be considered herein are attached and separated flows immediately upstream and downstream of oscillating shock waves, respectively. The non-homogeneity may result from intermittency of the shock wave oscillation or from a more basic modification to the turbulence structure of attached and separated flow due to the motion of the shock wave. The variations in both the overall level and power spectra with position relative to the shock wave are evident in Figure 13. These data are shown in comparison with homogeneous attached and separated flow data to illustrate the presence of low frequency energy due to the shock wave. Again, basic characteristics of the overall levels, power spectra, and cross-power spectra will be discussed for the purpose of defining empirical prediction techniques for the non-homogeneous attached and separated flows.

Overall Level

The overall fluctuating pressure levels for attached and separated flow in close proximity to an oscillating shock wave are bounded on the low side by the levels of fluctuating pressures corresponding to homogeneous environments and are bounded on the high side by the peak fluctuating pressures corresponding to shock wave oscillation. In essence, this means that the differences between the homogeneous and non-homogeneous fluctuating pressure levels may be attributed directly to fluctuating pressures induced by the oscillating shock wave for the case considered here. Thus, normalized fluctuating pressure levels for non-homogeneous flows may be defined as:

$$\left(\frac{\sqrt{\overline{P^2}}}{q_\infty}\right)^H_A \leq \left(\frac{\sqrt{\overline{P^2}}}{q_\infty}\right)^{NH}_A \leq \left(\frac{\sqrt{\overline{P^2}}}{q_\infty}\right)^H_{SW} \tag{26}$$

$$\left(\frac{\sqrt{\overline{P^2}}}{q_\infty}\right)_S^H \leq \left(\frac{\sqrt{\overline{P^2}}}{q_\infty}\right)_S^{NH} \leq \left(\frac{\sqrt{\overline{P^2}}}{q_\infty}\right)_{SW}^H \tag{27}$$

where the subscripts and superscripts are defined as follows:

Subscripts   A   -   attached flow

                  S   -   separated flow

                 SW   -   shock wave

Superscripts   H   -   homogeneous condition

                  NH   -   non-homogeneous condition

Under the assumption of statistical independence between the various sources, i.e., attached flow, separated flow and shock wave oscillation, the fluctuating pressure levels may be expressed as:

$$\left(\frac{\sqrt{\overline{P^2}}}{q_\infty}\right)_A^{NA} = \sqrt{\left[\left(\frac{\sqrt{\overline{P^2}}}{q_\infty}\right)_A^H\right]^2 + c_1\left[\left(\frac{\sqrt{\overline{P^2}}}{q_\infty}\right)_{SW}^H\right]^2} \tag{28}$$

$$\left(\frac{\sqrt{\overline{P^2}}}{q_\infty}\right)_S^{NH} = \sqrt{\left[\left(\frac{\sqrt{\overline{P^2}}}{q_\infty}\right)_S^H\right]^2 + c_2\left[\left(\frac{\sqrt{\overline{P^2}}}{q_\infty}\right)_{SW}^H\right]^2} \tag{29}$$

where c_1 and c_2 are weighting functions less than 1.0, which represent the contribution of the shock wave to the overall fluctuating pressure level. The values of c_1 and c_2 vary with spatial location relative to the shock wave and therefore, are difficult to predict. However, the above method of representation is useful in the prediction of power spectra for non-homogeneous flows as will be shown in the next section.

A-29

Power-Spectra

To predict the power spectra for non-homogeneous flows, a prior knowledge of the overall fluctuating pressure levels is required. Under the assumption of statistical independence between the various contributing sources, the power spectra for non—homogeneous environments may be written as the summation of power spectra of the contributing sources. Using the same symbolic representation as for the overall level, the power spectra for non-homogeneous environments may be written as:

$$\left[\phi(f)\right]_A^{NH} = \left[\phi(f)\right]_A^H + c_1 \left[\phi(f)\right]_{SW}^{I,H} \tag{30}$$

$$\left[\phi(f)\right]_S^{NH} = \left[\phi(f)\right]_S^H + c_2 \left[\phi(f)\right]_{SW}^{I,H} \tag{31}$$

From Equations 30 and 31 , c_1 and c_2 are given as

$$c_1 = \frac{\left(\dfrac{\overline{p^2}}{q_\infty^2}\right)_A^{NH} - \left(\dfrac{\overline{p^2}}{q_\infty^2}\right)_A^H}{\left(\dfrac{\overline{p^2}}{q_\infty^2}\right)_{SW}^{I,H}} \tag{32}$$

$$c_2 = \frac{\left(\dfrac{\overline{p^2}}{q_\infty^2}\right)_S^{NH} - \left(\dfrac{\overline{p^2}}{q_\infty^2}\right)_S^{H}}{\left(\dfrac{\overline{p^2}}{q_\infty^2}\right)_{SW}^{I,H}}$$

(33)

To determine the power spectra for non-homogeneous attached flow as caused by shock wave oscillation in the vicinity of the attached flow region, Equations 2, 22, and 32 are substituted into Equation 30, which gives a form normalized by local conditions upstream of the shock wave:

$$\left[\frac{\phi(f)\, U_0}{q_\infty^2\, \delta_0}\right]_A^{NH} = \frac{\left(\dfrac{\overline{p^2}}{q_\infty^2}\right)_A^{H}}{\left(\dfrac{f_0\, \delta_0}{U_0}\right)_A \left\{1 + \left(f/f_0\right)^{0.9}\right\}^2} + $$

$$\frac{\left(\dfrac{\overline{p^2}}{q_\infty^2}\right)_A^{NH} - \left(\dfrac{\overline{p^2}}{q_\infty^2}\right)_A^{H}}{\left(\dfrac{f_0\, \delta_0}{U_0}\right)_{SW} \left\{1 + \left(f/f_0\right)^{1.55}\right\}^{1.7}}$$

(34)

A-31

Similarly, substitution of Equations 10, 22, and 33 into Equation 31, leads to the following expression for non-homogeneous separated flow:

$$
\left[\frac{\phi(f)\, U_0}{c_\infty^2\, \delta_0}\right]_S^{NH} = \frac{\left(\dfrac{\overline{p^2}}{q_\infty^2}\right)_S^{H}}{\left(\dfrac{f_0\, \delta_0}{U_0}\right)_S \left\{1 + \left(f/f_0\right)^{0.83}\right\}^{2.15}} +
$$

$$
\frac{\left(\dfrac{\overline{p^2}}{q_\infty^2}\right)_S^{NH} - \left(\dfrac{\overline{p^2}}{q_\infty^2}\right)_S^{H}}{\left(\dfrac{f_0\, \delta_0}{U_0}\right)_{SW} \left\{1 + \left(f/f_0\right)^{1.55}\right\}^{1.7}} \tag{35}
$$

Comparison of these predictions with experimental measurements are shown in Figure 13.

A-32

APPENDIX — REFERENCES

1. Lowson, M. V., "Prediction of Boundary Layer Pressure Fluctuations," Wyle Laboratories Research Staff Report WR 67-15, October 1967.

2. Speaker, W. V. and Ailman, C. M., "Spectra and Space-Time Correlations of the Fluctuating Pressures at a Wall Beneath a Supersonic Turbulent Boundary Layer Perturbed by Steps and Shock Waves," NASA CR-486, May 1966.

3. Bull, M. K., "Properties of the Fluctuating Wall Pressure Field of a Turbulent Boundary Layer," AGARD Report 455, April 1963.

4. Bull, M. K., et al., "Wall Pressure Fluctuations in Boundary Layer Flow and Response of Simple Structure to Random Pressure Fields," University of Southampton, AASU Report 243, 1963.

5. Kistler, A. L. and Chen, W. S., "The Fluctuating Pressure Field in a Supersonic Turbulent Boundary Layer," Jet Propulsion Laboratory Technical Report No. 32-277, August 1962.

6. Belcher, P. M., "Predictions of Boundary Layer Turbulence Spectra and Correlations for Supersonic Flight," Presented at the 5th International Acoustic Congress, Liege, Belgium, September 1965.

7. Serafini, J. S., "Wall Pressure Fluctuations and Pressure Velocity Correlations in a Turbulent Boundary Layer," NASA TR R-165, December 1963.

8. Bakewell, H. P. Jr., et al., "Wall Pressure Correlation in Turbulent Pipe Flow," U. S. Navy Sound Laboratory Report No. 559, August 1962.

9. Shattuck, R. D., "Sound Pressures and Correlations of Noise on the Fuselage of a Jet Aircraft in Flight," NASA TN-D-1086, August 1961.

10. Willmarth, W. W. and Roos, F. W., "Resolution and Structure of the Wall Pressure Field Beneath a Turbulent Boundary Layer," J. Fluid Mech., Vol. 22, Part , pp. 81-94, 1965.

11. Maestrello, L., "Measurement of Noise Radiated by Boundary Layer Excited Panels," J. Sound Vib., 2 (2), 1965.

12. Hilton, D. A., "In-Flight Aerodynamic Noise Measurements on a Scout Launch Vehicle," NASA TN D-1818, July 1963.

13. Williams, D. J. M., "Measurements of the Surface Pressure Fluctuations in a Turbulent Boundary Layer in Air at Supersonic Speeds," University of Southampton, AASU Report No. 162, Department of Aeronautics and Astronautics, December 1960.

14. Chyu, W. J. and Hanly, R. D., "Power and Cross-Spectra and Space Time Correlation of Surface Fluctuating Pressures at Mach Numbers Between 1.6 and 2.5," AIAA Preprint No. 68-77, January 1968.

15. Maestrello, L., "Measurement and Analysis of the Response Field of Turbulent Boundary Layer Excited Panels," J. Sound and Vib., 2, No. 3, July 1965.

16. Willmarth, W. W. and Woolridge, C. E., "Measurements of the Fluctuation Pressure at the Wall Beneath a Thick Turbulent Boundary Layer," J. Fluid Mech., Vol. 14, pp. 187-210, 1962.

17. Bozich, D. J. and White, R. W., "Study of the Vibration Responses of Shells and Plates to Fluctuating Pressure Environments," Wyle Laboratories Research Staff Report WR 69-19, September 1969.

18. Robertson, J.E., "Wind Tunnel Investigation of the Effects of Reynolds Number and Model Size on the Steady and Fluctuating Pressures Experienced by Cone Cylinder Missile Configurations at Transonic Speeds," AEDC-TR-66-266, March 1967.

19. Coe, Charles F., "Surface Pressure Fluctuations Associated with Aerodynamic Noise," Basic Aerodynamic Noise Research Conference Proceedings, NASA SP-207.

20. Coe, Charles F., and Rechtien, R. D., "Scaling and Spatial Correlation of Surface Pressure Fluctuations in Separated Flow at Supersonic Mach Numbers," Paper presented at the AIAA Structural Dynamics and Aeroelasticity Specialist Conference, New Orleans, La., April 16-17, 1969.

21. Rechtien, Richard D., "A Study of the Fluctuating Pressure Field in Regions of Induced Flow Separation at Supersonic Speeds," University of Missouri - Rolla UMR Research Report, May 1970.

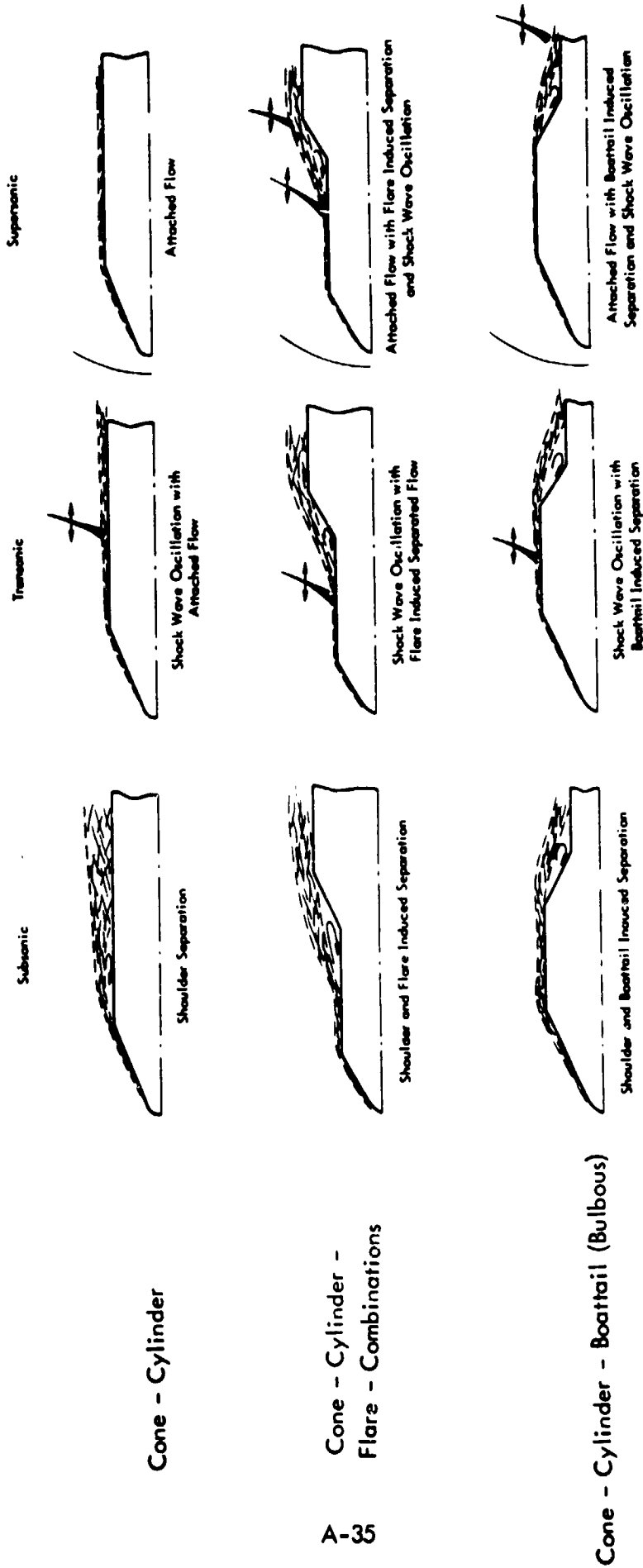**Basic Vehicle Geometry**

Mach Number Range

Subsonic

Transonic

Supersonic

Cone – Cylinder

Shoulder Separation

Shock Wave Oscillation with Attached Flow

Attached Flow

Cone – Cylinder – Flare – Combinations

Shoulder and Flare Induced Separation

Shock Wave Oscillation with Flare Induced Separated Flow

Attached Flow with Flare Induced Separation and Shock Wave Oscillation

Cone – Cylinder – Boattail (Bulbous)

Shoulder and Boattail Induced Separation

Shock Wave Oscillation with Boattail Induced Separation

Attached Flow with Boattail Induced Separation and Shock Wave Oscillation

Figure 1. Subsonic, Transonic, and Supersonic Flow Fields for Basic Vehicle Configurations
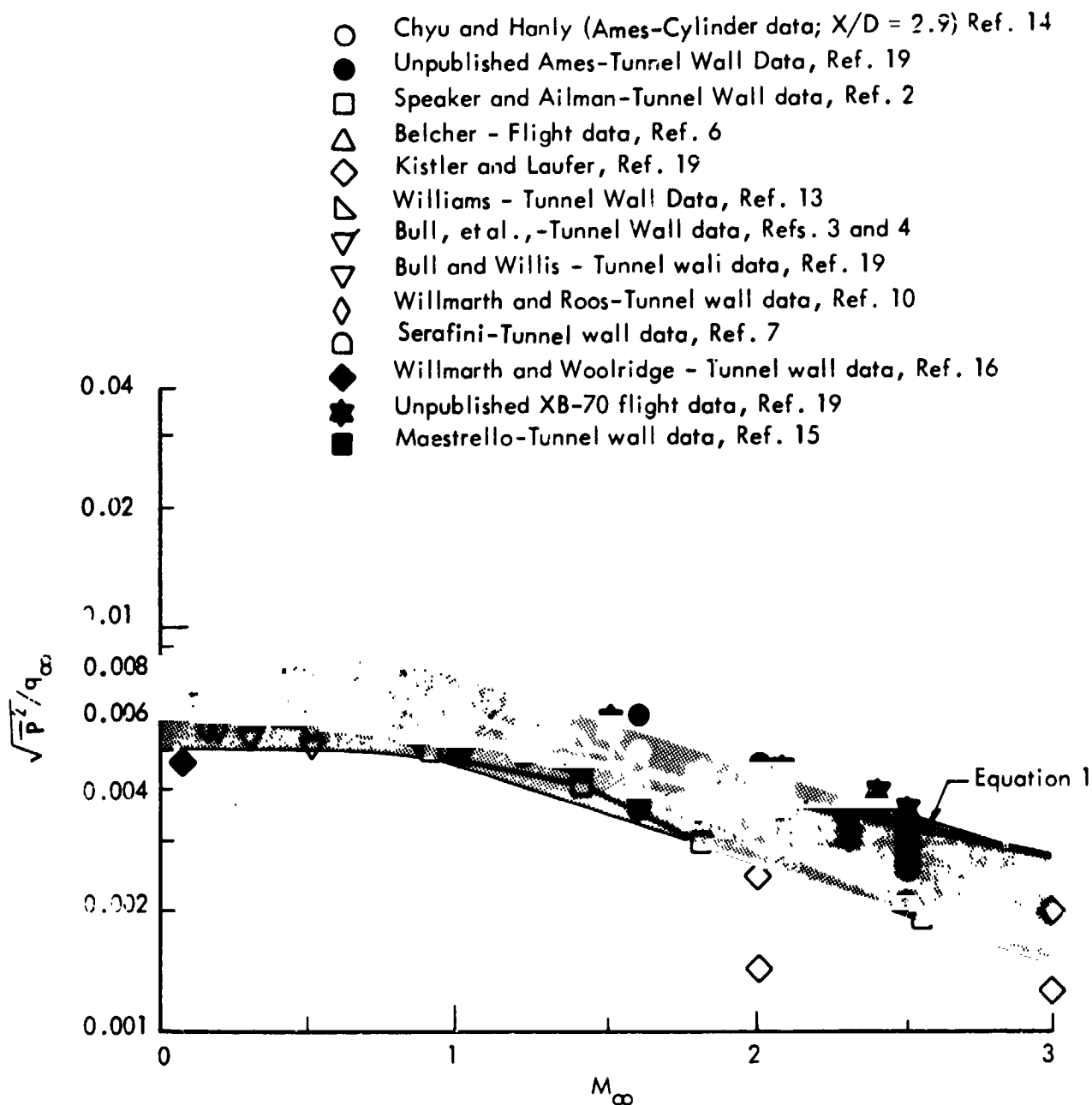
Figure 2. Comparison of Pressure Fluctuation Measurements beneath Attached Flows by Various Investigators
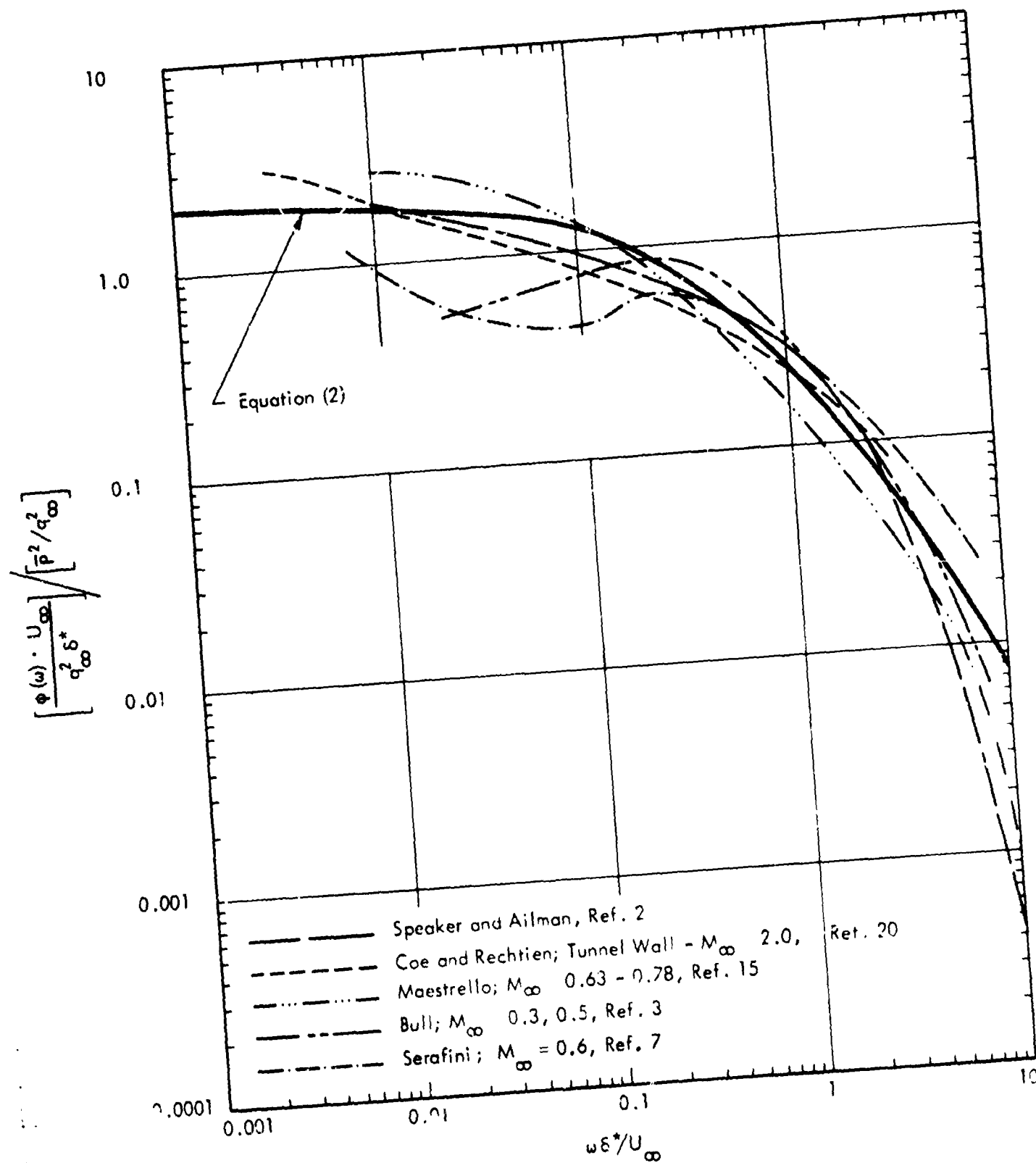
Figure 3. Power Spectra for Turbulent Boundary Layer Fluctuating Pressures

A-37
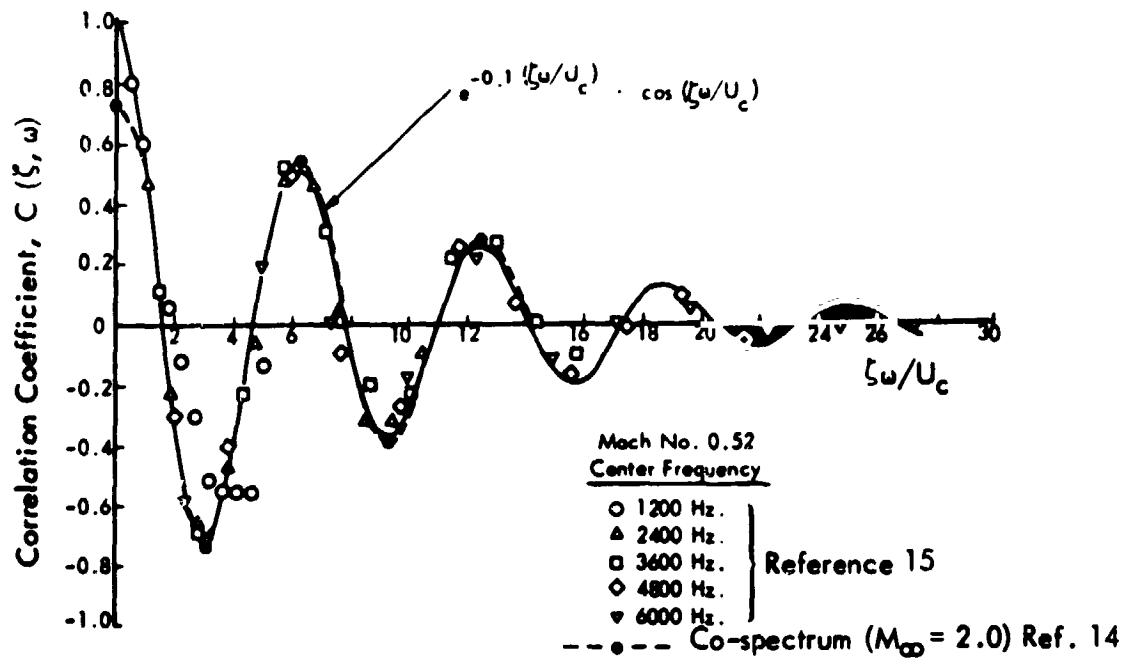
Figure 4a. Narrow Band Longitudinal Space Correlation Coefficient
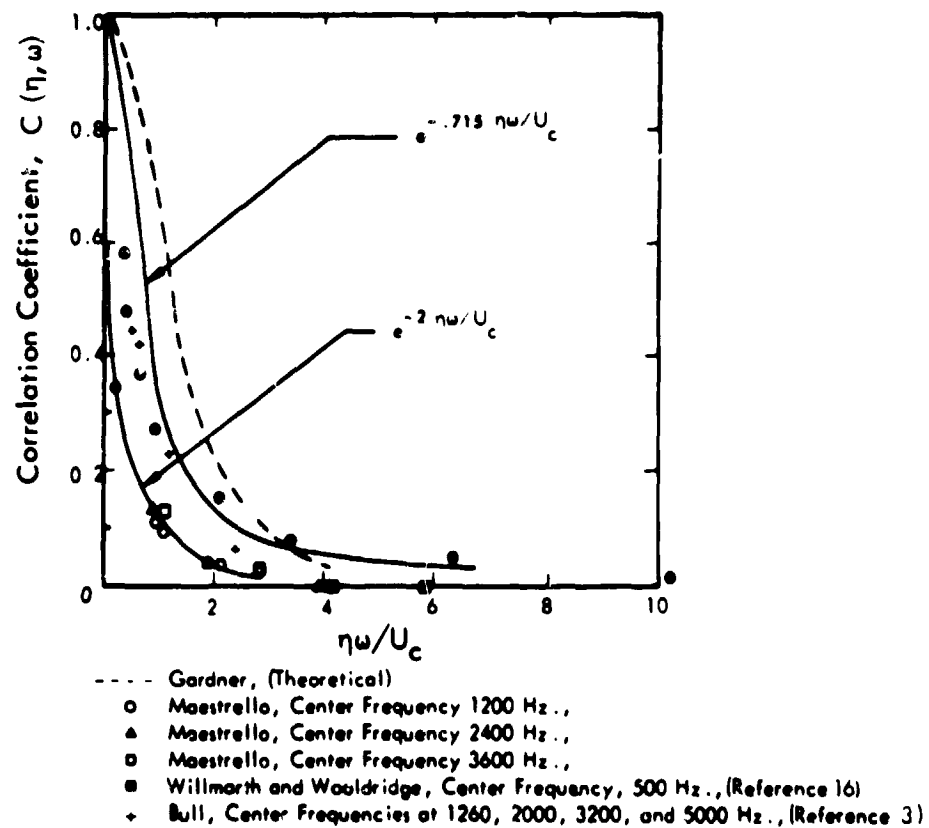for Boundary Layer Fluctuating Pressures

Figure 4b. Narrow Band Lateral Space Correlation Coefficient for
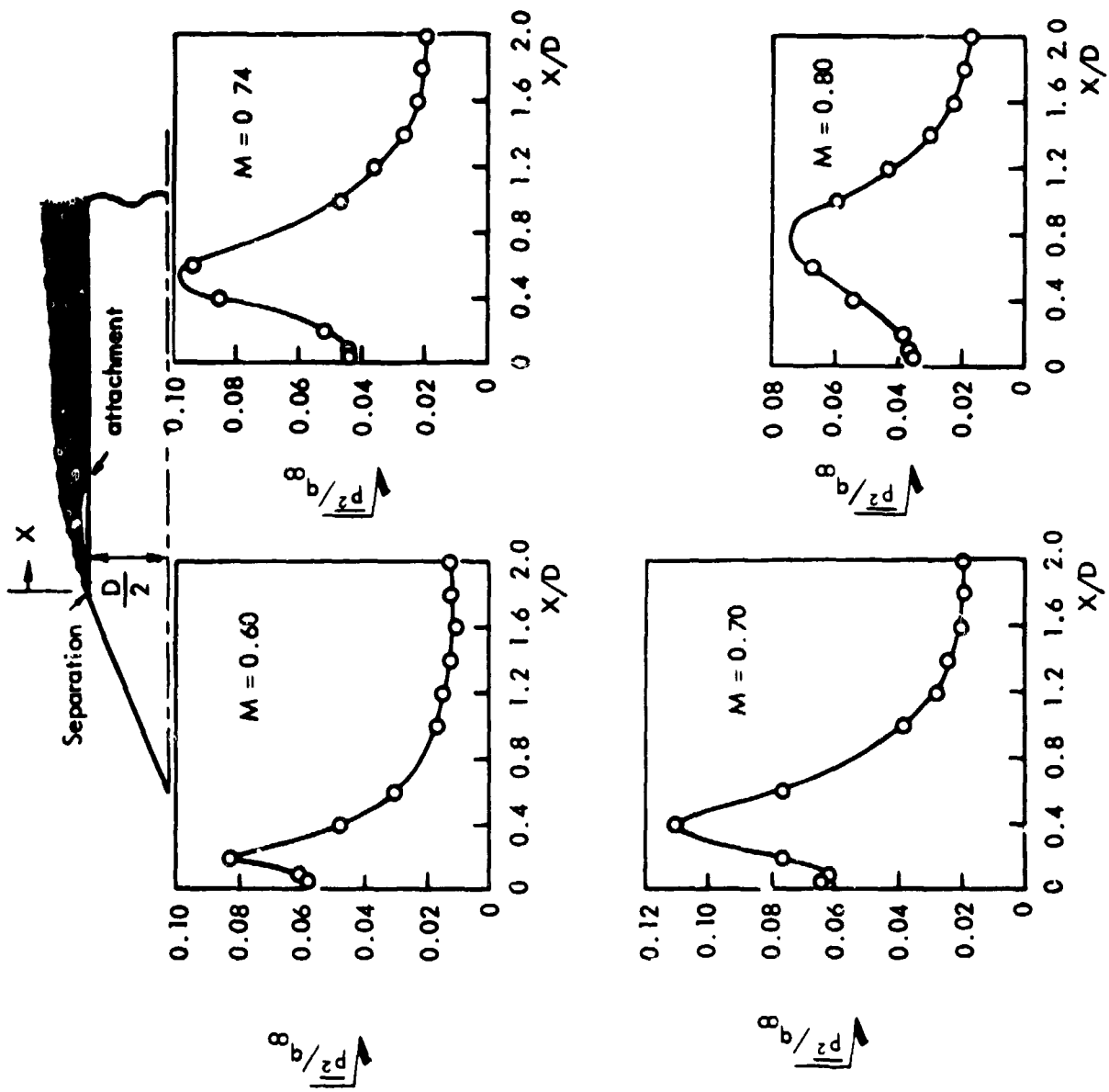Boundary Layer Fluctuating Pressures

A-38

Figure 5. Axial Distributions of Fluctuating Pressures for Blunt Body Separated Flow; 25 Degree Cone-Cylinder (Reference 18)

$$* \text{ NOTE: } C_P = \frac{P_{\ell_s} - P_\infty}{q_\infty} = \frac{(\text{local static pressure}) - (\text{free-stream static pressure})}{\text{free-stream dynamic pressure}}$$

O M = 1.6
● M = 2.5
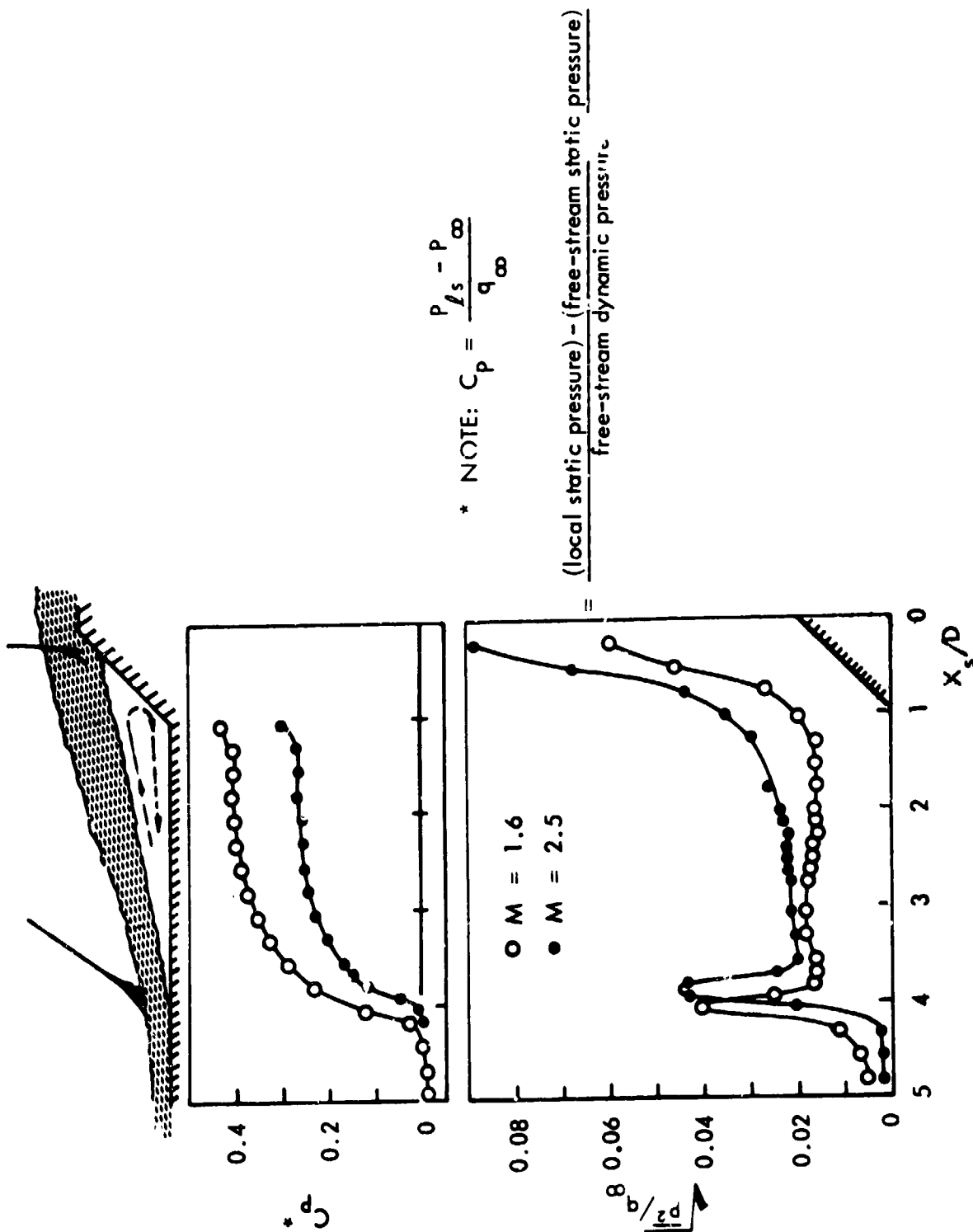
Figure 6. Axial Distributions of Static and Fluctuating Pressures for 45 Degree Flare Induced Separation (Ref. 14)

Figure 7. Variation of Normalized RMS Fluctuating Pressure Level with Local Mach Number for Expansion Induced Separated Flow

Legend:
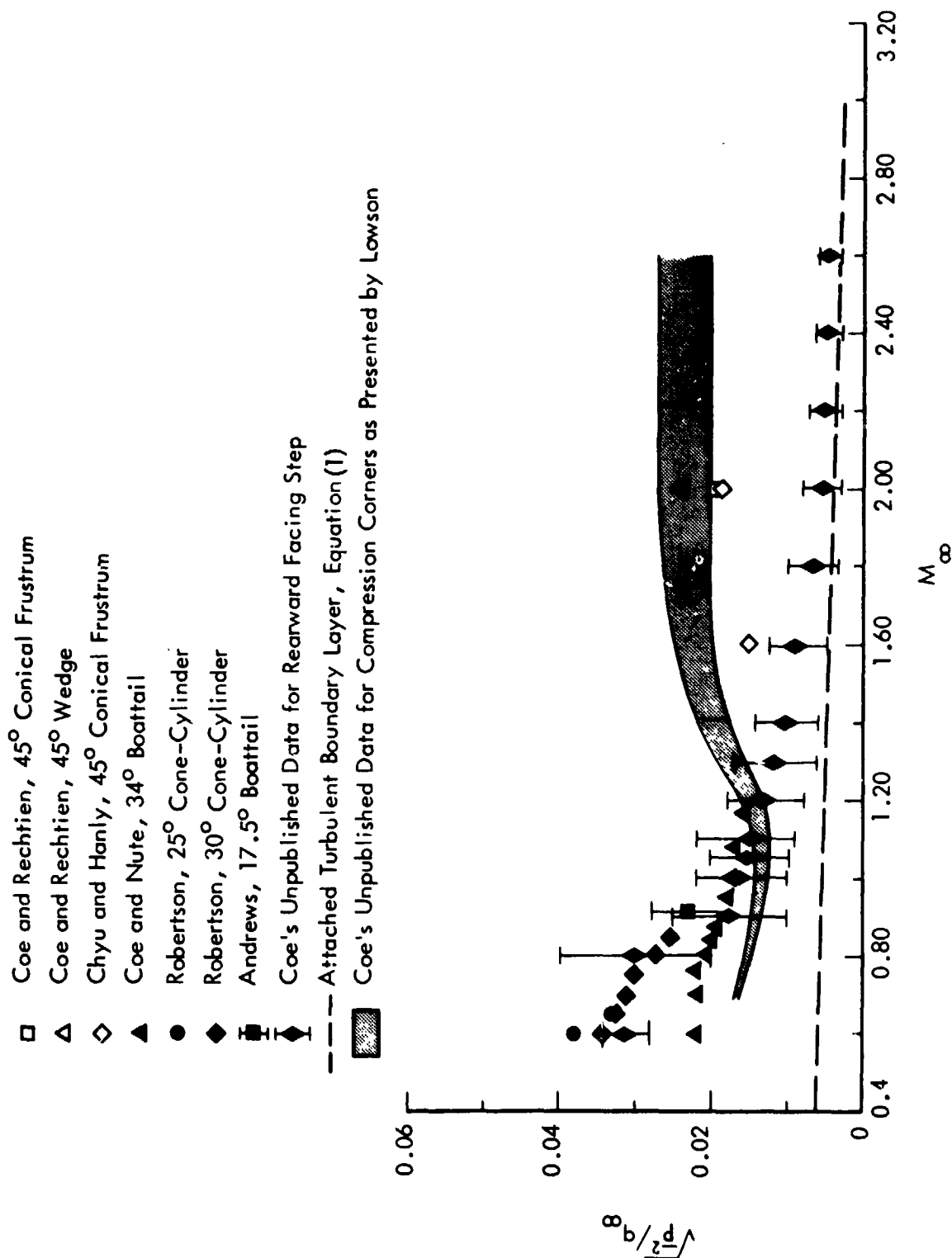- ● Coe's unpublished data for rearward facing steps
- ▼ Coe and Knute, 34° boattail
- ■ Robertson, 25° cone-cylinder
- ◆ Robertson, 30° cone-cylinder
- ▲ Andrews, 17.5° boattail

$$\frac{0.045}{1 + M_\ell^2}$$

Vertical axis: $\sqrt{\overline{p^2}}/q_\infty$

Horizontal axis: M_ℓ

Figure 8. Variation of Normalized RMS Fluctuating Pressure Level with Free-Stream Mach Number for Expansion Induced and Compression Induced Separated Flows
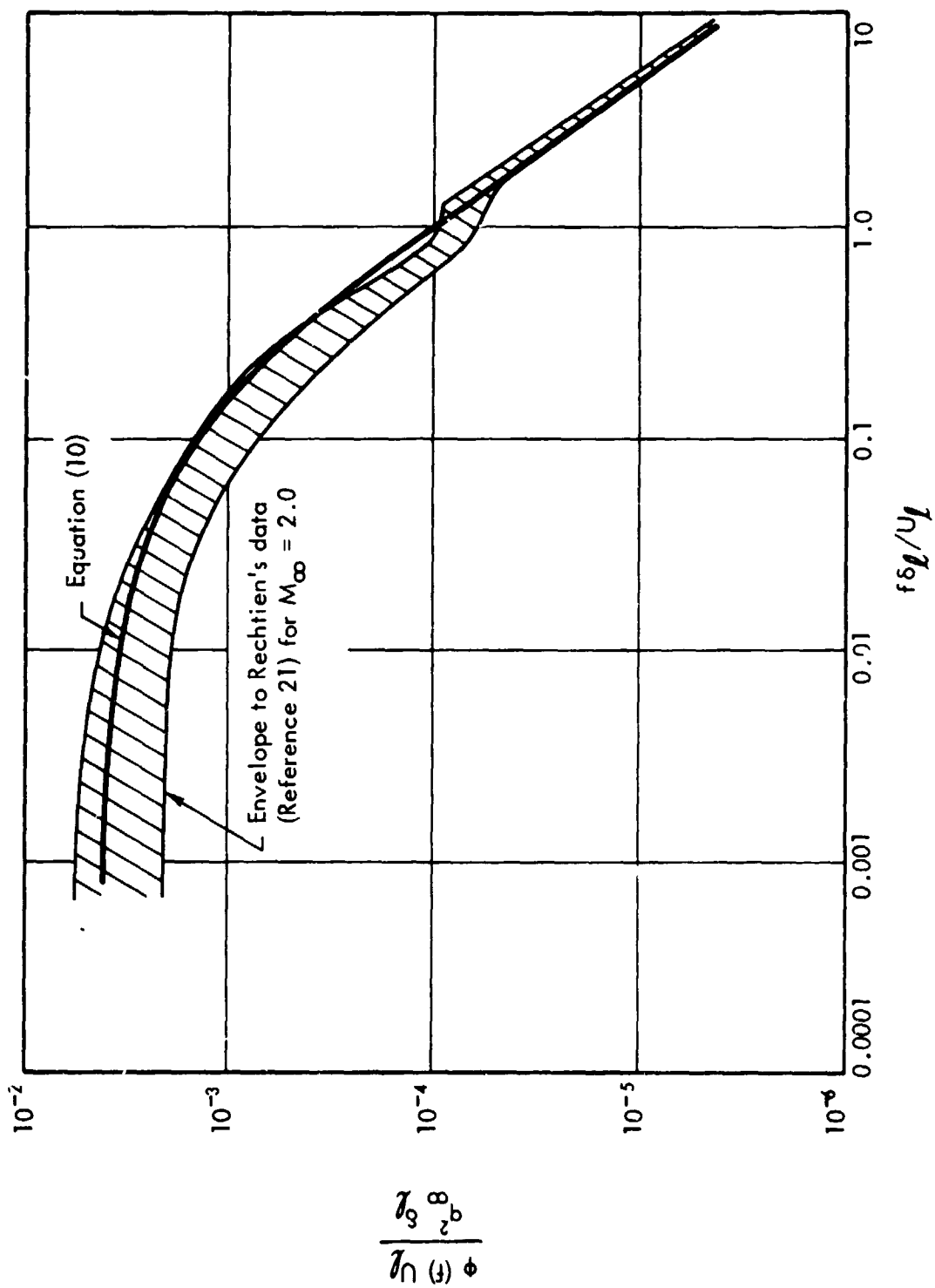
Legend:

□ Coe and Rechtien, 45° Conical Frustrum
△ Coe and Rechtien, 45° Wedge
◇ Chyu and Hanly, 45° Conical Frustrum
▲ Coe and Nute, 34° Boattail
● Robertson, 25° Cone-Cylinder
◆ Robertson, 30° Cone-Cylinder
Andrews, 17.5° Boattail
Coe's Unpublished Data for Rearward Facing Step
— — Attached Turbulent Boundary Layer, Equation (1)
Coe's Unpublished Data for Compression Corners as Presented by Lowson

Figure 9. Power Spectrum of Fluctuating Pressures within Separated Flow Regions

A-43
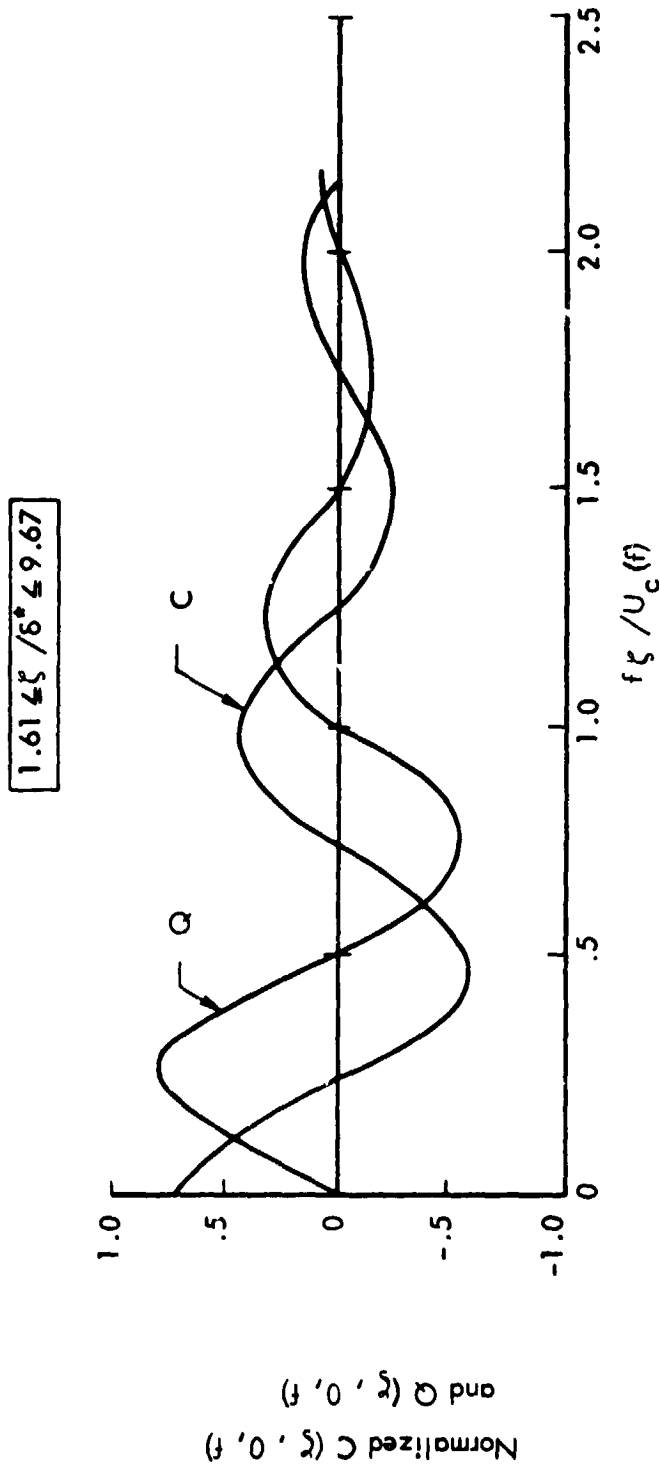
Figure 10. Typical Longitudinal Cross-Spectra of Pressure Fluctuations for Separated Flow (Ref. 14)
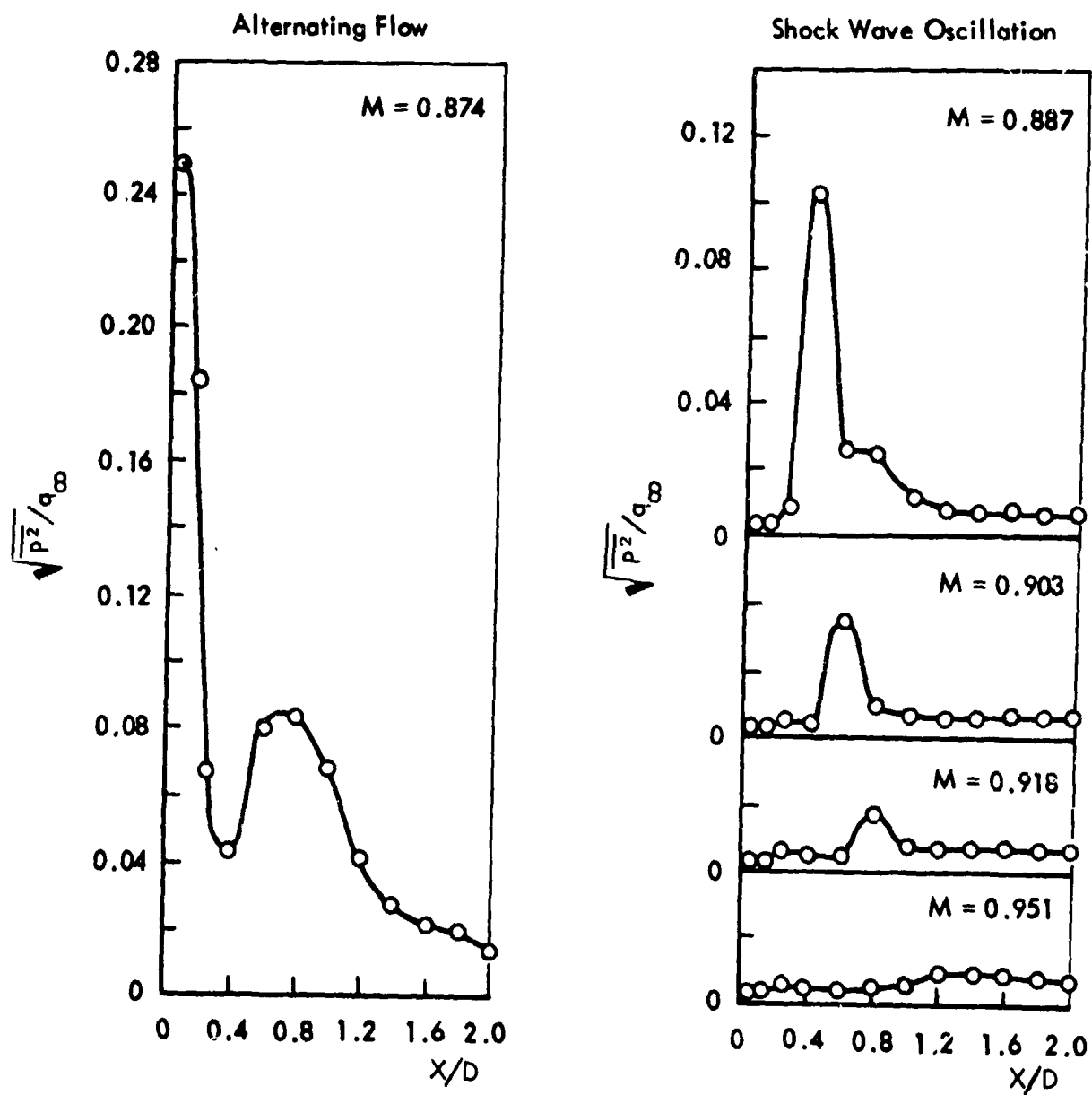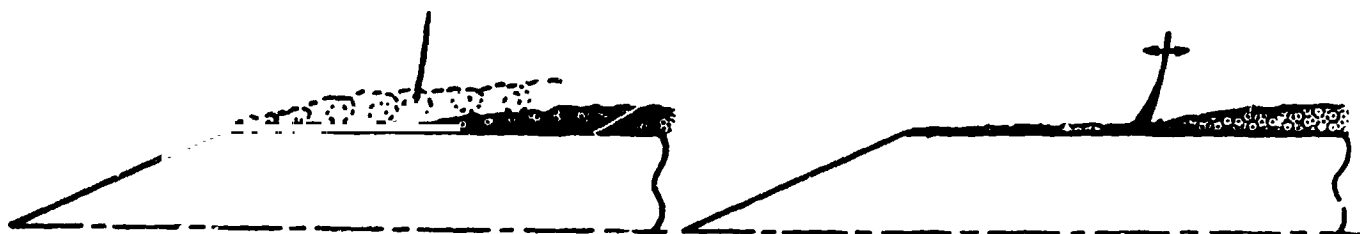
Figure 11. Axial Distribution of Fluctuating Pressures; 25 Degree Cone-Cylinder
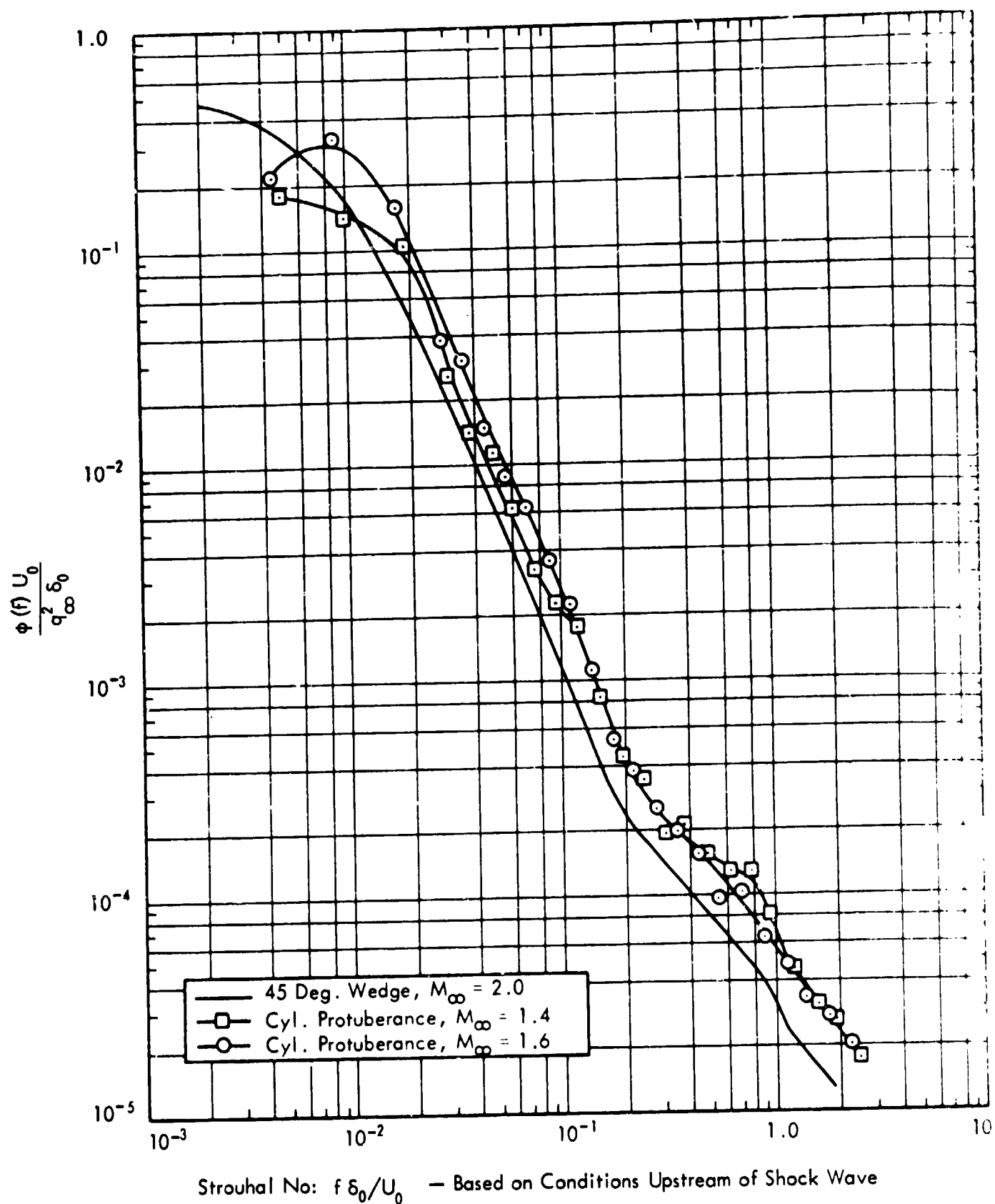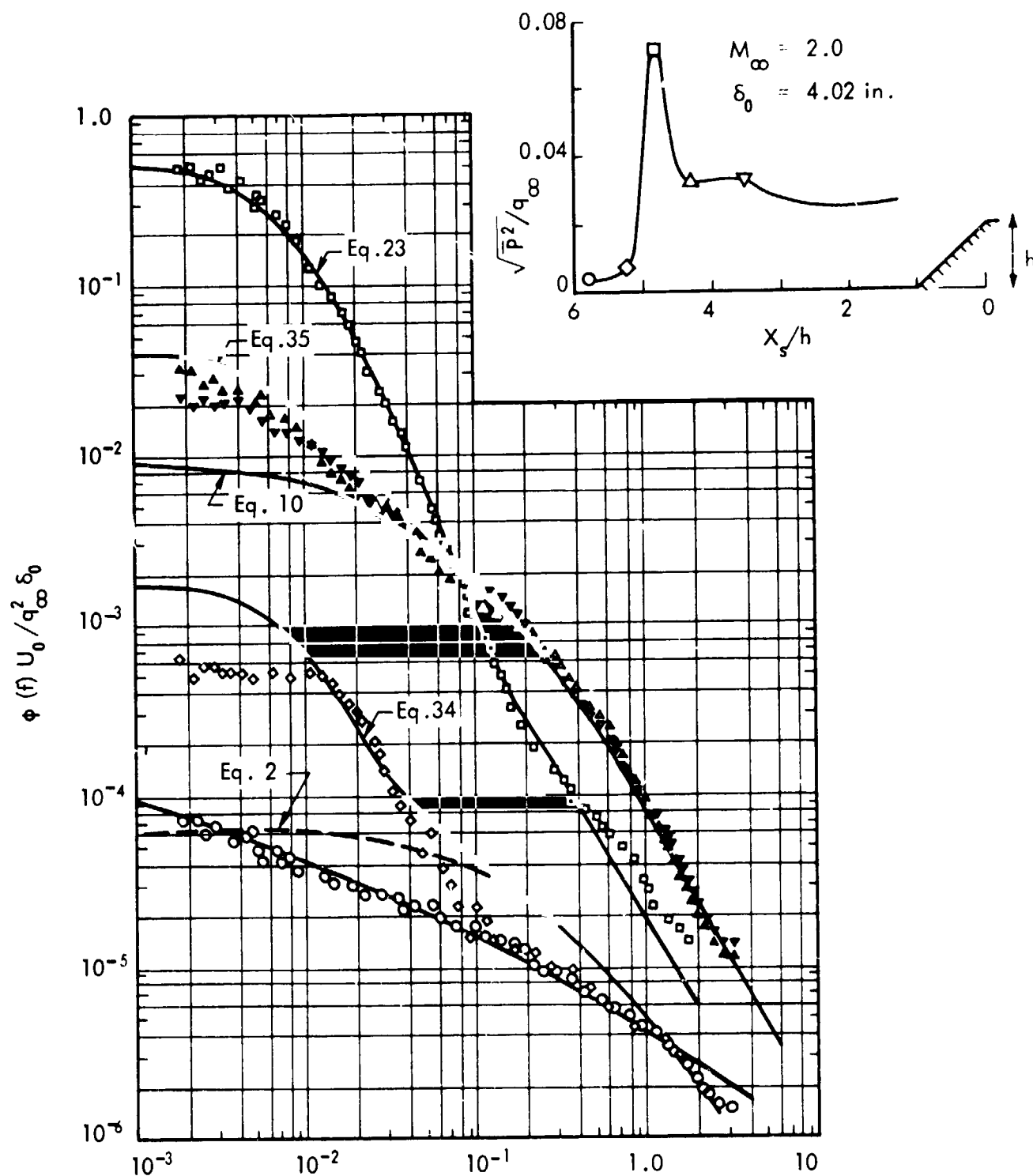
Figure 12. Comparison of Power Spectra for Shock-Wave Oscillation
Induced by Two- and Three-Dimensional Protuberances

A-46

Figure 13. Longitudinal Distribution of Pressure Fluctuations and Typical Power
Spectra in Vicinity of Supersonic Flow Separation Ahead of a 45° Wedge

Strouhal No: $f \delta_0 / U_0$ — Based on Conditions Upstream of Shock Wave

○ Attached turbulent boundary layer

◇ Non-homogeneous attached turbulent boundary layer

▽ △ Non-homogeneous separated flow
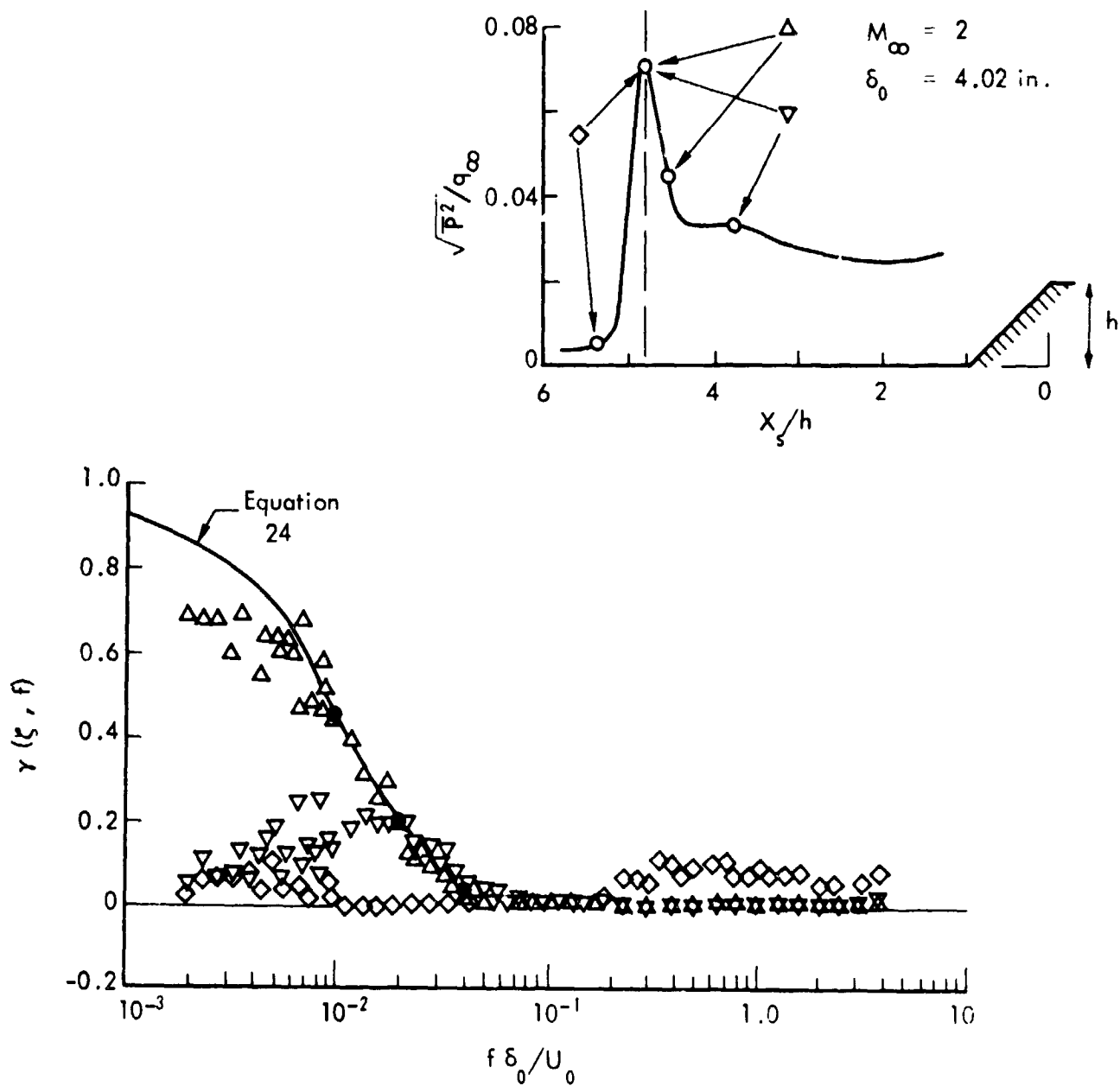
□ Shock wave oscillation

Figure 14. Correlation of Pressure Fluctuations Between Shock Wave and Adjacent Attached and Separated Flows (Reference 20)